Investigation of and correction for waveform changes arising from NMO stretch

---

A Thesis

Presented to

the Faculty of the Department of Earth and Atmospheric Sciences

University of Houston

In Partial Fulfillment

of the Requirements for the Degree

Master of Science

By

Un Young Lim

May 2014

Investigation of and correction for waveform changes arising from NMO stretch

---

Un Young Lim

APPROVED:

Dr. John P. Castagna (Chairman)

Dr. Hua-wei Zhou (Member)

Dr. Seung Yoo (Member)

Dean, College of Natural Sciences and Mathematics

To my wife

ACKNOWLEDGEMENTS

First and foremost, I would like to express my sincere appreciation to my thesis advisor, Dr. John Castagna, for his support and guidance during my study here at University of Houston. He has been giving me the knowledge ranging from fundamental background of Exploration Geophysics to recent state-of-art research areas in the field, as well as his valuable experience and inspiration to build up my research ability. Above all, since he always teaches me the most important thing for being a good researcher, the passion, now I believe that someday I would become a professional geophysicist who can contribute to overcoming most difficult challenges in Exploration Geophysics. I would also give my sincere gratitude to the rest of my thesis committee, Dr. Hua-wei Zhou and Dr. Seung Chul Yoo for their encouragement and invaluable advice. They were always willing to help me whenever I was in need and discuss the tough problems I encountered during this research.

In addition, I would like to thank my friends and colleagues at the University of Houston, Juan Berrizbeitia, Chen Liang, and Arnold Oyem. My special thanks go to Arnold Oyem, who helped me in dealing with spectral decomposition methods. Most of all, I want to thank Stu Fagin and Valence Operating Company for providing the Hitts Lake data.

Last, but not least, I have to thank my wife Minsung Lim who is my son Juhwan's mother for the endless supports and love to me and our family. Even though she has been waiting for my graduation a long time, she always cheers me up and prays for me and my research. I believe she deserves my respect. I am also heartily thankful to both our parents. Without their supports and cheering, I couldn’t have dreamed of studying Geophysics in the States. It is only possible because of their sacrifice. Finally, I have to appreciate God, who is my Lord, to lead my life on his road, who opened my heart to pay attention to what he has been saying for me and gave me endless life.

Investigation of and correction for waveform changes arising from NMO stretch

---

An Abstract of a Thesis

Presented to

the Department of Earth and Atmospheric Sciences

University of Houston

In Partial Fulfillment

of the Requirements for the Degree

Master of Science

By

Un Young Lim

May 2014

ABSTRACT

NMO-stretch distorts seismic frequency content significantly depending on depths of the target reservoir and offset locations. It causes poor resolution on CMP-stacked sections for image processing, and also creates difficulty in extracting the exact wavelet for AVO analysis and seismic inversion. In order to quantitatively study waveform changes arising from NMO-stretch, two synthetic convolution models are generated with the Zoeppritz equations. For both models, the amount of frequency shift, called 'stretch-ratio', are computed to determine waveform changes accurately. In the first model, which generates one reflectivity boundary concerning top of AVO Class 3 gas-saturated bed, general tendencies of the waveform changes are investigated. From comparison of results based on the spectral analyses between waveform changes before and after applying NMO-correction to the model, the progressive reduction of bandwidth and shift toward lower frequencies are detected along with increased offset. The second model is designed to investigate degree of NMO-stretch in the cases of typical AVO Class 3, 2 and 1. In this model, separations between the degrees of NMO-stretch for top of gas-saturated bed and top of brine-saturated bed concerning AVO Class 3, 2 and 1 noticeably increase along with increased offset. This indicates that gas and wet situations of typical AVO Classes could be differentiated by proper investigation of NMO-stretch in far offset ranges of pre-stack seismic data. A strategy using wavelet deconvolution is proposed as a method to correct waveform changes determined from above models. A multi-layered model is also used to test the effectiveness of the wavelet deconvolution-based NMO-stretch correction for realizing a more realistic situation. Additionally, in order to verify the effectiveness of the correction, time-frequency panels of the second model and the multi-layered model are generated with Short Time Fourier Transform, Continuous Wavelet Transform, and Constrained Least Squares Spectral Analysis. Applying the NMO-stretch correction corrects NMO-stretches of the synthetic models and recovers investigated waveforms before applying NMO-correction in the NMO-corrected gathers. An application to a synthetic seismogram based on real data from Hitts Lake Field also verifies the effectiveness of correction. The correction improves the alignments of reflections on targeted boundary and corrects lower frequency contents in far offset ranges.

TABLE OF CONTENTS

Page

LIST OF FIGURES

FIGURE Page

LIST OF TABLES

CHAPTER I

INTRODUCTION

1.1 Background and motivation

Normal moveout (NMO) is the effect that the distance between a seismic source and a receiver (the offset) has on the arrival time of a reflection in the form of an increase of time with offset. The relationship between arrival time and offset is hyperbolic and it is the principal criterion that a geophysicist uses to decide whether an event is a reflection or not (Sheriff and Geldart, 1995). As a pre-processing method of common mid-point (CMP) stacking for improvement in signal to noise ratio, normal move-out (NMO) correction, a process that flattens hyperbolic reflections on offset versus travel time panel, is commonly conducted in imaging and processing area (Zhou, 2014). Also, the alignment for the reflection events on the CMP gather by NMO-correction, by means of removing the offset dependency of the timing in the reflectivity sequence, is necessary not only in image processing but also in interpretation such as amplitude variation with offset (AVO) analysis. On the other hand, since the NMO-correction has a non-linear tendency, it produces a significant side effect called NMO-stretch (Dunkin and Levin, 1973). It could distort frequency contents significantly depending on depths of target reservoir and offset locations. To be more specific, shift toward lower frequencies due to NMO-stretch arises more severely at far offset and shallow depth. It provides poor resolution on CMP-stacked sections for image-processing, and also causes difficulty in extracting the exact wavelet for AVO analysis and seismic inversion. In order to prevent these problems, a certain range of far offset data in CMP gather is generally muted depending on conditions. Muting a certain percent of NMO-stretch is

another common technique (Yilmaz, 2001). However, as occasion demands, longer offset data are necessary for interpretation, especially in AVO analysis. Even if it isn't needed, if the NMO-stretch could be corrected properly, the acquired full data set could be used for the purpose of improving signal to noise ratio to image sub-surface area and provide better chances for the interpreter to estimate a more accurate wavelet in seismic data interpretation.

1.2 Modeling and Investigation of waveform changes arising from NMO-stretch

Before developing a method to correct NMO-stretch, spectral analyses have to be preceded to determine waveform changes with offset due to NMO-correction (Castoro et al., 2001). The second chapter in this thesis introduces methodologies to determine the degree of NMO-stretch along with an increase in offset. Two synthetic CMP gathers are generated from designed models with the Zoeppritz equations (Zoeppritz, 1919) for qualitative and quantitative analyses. The Zoeppritz equations are a set of equations that describe the partitioning of seismic wave energy at an interface, typically a boundary between two different layers of rock. Zoeppritz solved the amplitudes of reflected and transmitted waves using the conservation of stress and displacement across the layer boundary, which provides the equations that involve incident angle, densities, and elastic moduli. In Appendix A, the Zoeppritz equations are described in their matrix form. The first model, which generates one reflectivity boundary concerning top of AVO Class 3 gas-saturated layer, is built for investigation of the general tendencies of waveform changes arising from NMO-stretch. The second model is designed to investigate the degree of NMO-stretch in more specific situations of typical AVO Class 3, 2 and 1. If the degrees of NMO-stretch for gas-saturated and brine-saturated cases of the model are noticeably separated at the far offset, it would indicate that gas and wet situations concerning typical AVO Classes could be distinguished by

proper investigation of NMO-stretch at the far offset in pre-stack data. For both models, specific rock properties are introduced from a model based on a research of the Gulf of Mexico (Hilterman, 2001). Shale velocities and densities of the referred model were generated from selected well-log information in the Gulf of Mexico. Sand velocities and densities were also selected in order to yield reflection amplitudes corresponding to Class 3 (bright spot), 2 (phase reversal), and 1 (dim out) AVO anomalies. For the gas-saturated case of the referred model, the Greenberg-Castagna method (Greenberg and Castagna, 1992) was used to fluid-substitute gas from the brine-saturated case with fluid properties from Batzle and Wang (1992). After achieving synthetic CMP gathers of both models, NMO-correction and frequency analyses are implemented. Dominant frequencies of every trace in the first model before and after applying NMO-correction are computed for comparison. Variable densities of amplitude spectrum of every trace on the gather of the first model are also illustrated for presenting NMO-stretch effect. For the analysis of the second model, all cases regarding AVO Class 3, 2, and 1 of top of gas-saturated and brine-saturated beds are investigated with their dominant frequencies. For both models, the amount of frequency shift, called 'Stretch-ratio', devised by Dunkin and Levin (1973), are computed in order to determine waveform changes accurately. The proposed Stretch-ratio could be computed by determining the compression of reflectivity sequence between the reflectivity on NMO-corrected trace and un-corrected trace at certain offsets. In Appendix B, Dunkin and Levin's Stretch-ratio is described. Waveform changes of the two models arising from NMO-stretch could be quantitatively determined as a function of offset from the investigation and the acquired information will be used for the subsequent methodology to correct NMO-stretch which is described in Chapter 3.

1.3 NMO-stretch correction and validation of the method

Casotoro et al. (2001) devised the wavelet deconvolution method in order to remove NMO-stretch and correction of waveform changes. A brief description of the procedures for this method is as the following:

1. Applying NMO-correction,
2. Windowing and applying Fourier transform into the data,
3. Dividing the Fourier transform of each NMO-corrected segment by the Fourier transform of the corresponding isolated NMO-corrected wavelet,
4. Convolving the result with the wavelet and band-pass to provide a constant bandwidth output.

In Chapter 3 of this thesis, the author applies the strategy of Castoro et al. to the investigated models described above for correction of NMO-stretch occurred in the models. For conducting deconvolution of NMO-corrected wavelets from targeted NMO-corrected segments, Sacchi's sparse-deconvolution (1997) is used based on the sparse reflectivity assumption; a seismogram is composed of a finite superposition of seismic wavelets. Dunkin and Levin's multi-layered model (1973) is also used to test the effectiveness of wavelet deconvolution method for better understanding of a more realistic situation. P-wave velocity profile is obtained from the model of Dunkin and Levin (1973). Additional density and S-wave velocity profiles of Dunkin and Levin's model are computed by Gardner's empirical relation (Gardner et al., 1974) and Greenberg-Castagna's V_P-V_S relations (Greenberg and Castagna, 1992) for the generation of a synthetic CMP gather for this model. Additionally, for verifying validation of the method and conducting detailed frequency analysis, time-frequency analyses such as Short Time Window Fourier Transform

(STFT), Continuous Wavelet Transform (CWT), and Constrained Least Squares Spectral Analysis (CLSSA) are implemented. By executing the above spectral decomposition methods, 1-D targeted traces in the second model and Dunkin and Levin's multi-layered model could be transformed to 2-D time-frequency panels. The results of applying STFT into the targeted traces, which are before and after applying NMO-correction and after applying NMO-stretch correction, are illustrated to verify the effectiveness of the NMO-stretch correction for the models. Since CWT was devised to overcome the resolution problem of STFT (Alam and Taylor., 2006, Matos and Marfurt, 2008), and CLSSA showed better resolution compared to STFT and CWT (Puryear et al., 2012, Arnold and Castagna, 2013), other results applying CWT and CLSSA for selected segments of the targeted traces are also described to compare more details. In the results, we observe that distorted low frequencies are corrected and frequency information before applying NMO-correction is recovered with decent accuracy. Finally, a synthetic CMP gather is newly derived from a selected P-wave sonic log in Hitts Lake data set (Hitts Lake Field, onshore, Smith County, Texas) with a designed wavelet for the aim of applying the NMO-stretch correction method. A new P-wave velocity profile from the sonic-log is computed by implementing 4 milliseconds sliding averaging to solve the upscaling problem between measured data in well-logs and corresponding seismic data (Mukerji et al., 1995, Backus, 1962). After applying the NMO-stretch correction, more consistent frequencies could also be observed at targeted reflections on the gather.

1.4 Objectives of thesis

The goals of this thesis are briefly described below:

1. Quantitative investigation of waveform changes arising from NMO-stretch in proposed

models with the Stretch-ratio (Dunkin and Levin, 1973),

2. Testing of the Stretch-ratio as a new seismic attribute for reservoir characterization,

3. Applying the wavelet deconvolution method (Casotoro et al., 2001) into the proposed model including correction of investigated waveform changes,

4. Validation of the NMO-stretch correction with state-of-the-art time-frequency analyses,

5. Application of the correction with the synthetic seismogram based on real data, Hitts Lake Field, onshore Texas.

Detailed efforts to achieve the goals will be described in following chapters.

CHAPTER II

INVESTIGATION OF WAVEFORM CHANGES

2.1 Investigation of the first model

2.1.1 Model description

The first model generated by the author is a simple two-layer model. The model describes a reflectivity boundary of top of a gas-saturated bed corresponding to traditional AVO Class 3 anomaly. The main purpose of using this model is to investigate general tendencies of waveform changes arising from NMO-stretch quantitatively. Since only one reflectivity is generated from this model, the waveform changes can be easily determined along with the increase in offset (as a function of offset increase). The thickness of the first model is 2400 meter, which consists of two 1200 meter thickness layers. The designed shale layer is located on a gas-saturated sand layer at AVO Class 3 depth, 1200 meter environment. Rock properties of the model are introduced from a model, based on research of the Gulf of Mexico (GOM) (Hilterman, 2001) for representing gas-saturated sand anomaly of AVO at GOM. Specific rock properties of the first model are illustrated in Table 2.1.

Table 2.1. Rock properties for the first two-layer model.

Layer	Depth Profile (m)	ρ (gm/cm^3)	V_p (ft/s)	V_s (ft/s)	σ
Shale	0 ~ 1200	2.16	7190	2684	.419
Gas sand	1200 ~ 2400	1.88	5061	2956	.241

2.1.2 Synthetic well-logs

For generating common-midpoint gathers, CGG Veritas' Hampson-Russell is used. Since the model of this thesis is a one-dimensional depth model and Hampson-Russell requires specific well-logs for generating CMP gathers, an additional procedure that generates a set of synthetic well-logs is implemented prior to realizing the first model above. The well-log's information is written in LAS file format. The profile of Poisson's ratio (σ) does not need to be generated at this stage, because the values of Poisson's ratio (σ) of the first model can be computed by a combination of P-wave velocity (V_p) and S-wave velocity (V_s). Also, both P-wave and S-wave velocity values (ft/s) are converted in slowness ($\mu s/m$) for following LAS format. The generated set of synthetic well-logs for the first model is illustrated in Figure 2.1.

Fig. 2.1. Synthetic well-log for the first model described in Table 2.1.

2.1.3 Wavelet description

Since the following synthetic CMP gathers are generated on the basis of a convolutional model that uses convolution between modeled reflectivity series and a designed wavelet, determining wavelet properties is a prerequisite for further processes. The Ricker wavelet is generated with 35Hz dominant frequency and 100 milliseconds wavelet length. The wavelet has 2 milliseconds sampling rate and linear phase with zero phase rotation. The reason for setting a specific dominant frequency, 35Hz, of Ricker wavelet for the first model is that the author applies the wavelet into other following models, including Dunkin and Levin's multi-layered model (1973), which will be used for NMO-stretch correction in Chapter 3. In Dunkin and Levin, the wavelet was used to determine the degrees of NMO-stretch in their model. For better presentation, only designed Ricker wavelets are adopted in further processes due to the fact that Ricker wavelets have relatively shorter coda in time domain and smaller number of side lobes in comparison to synthetic band-pass wavelets. The Ricker wavelet for the first model and its amplitude spectrums in frequency domain are illustrated in Figure 2.2.

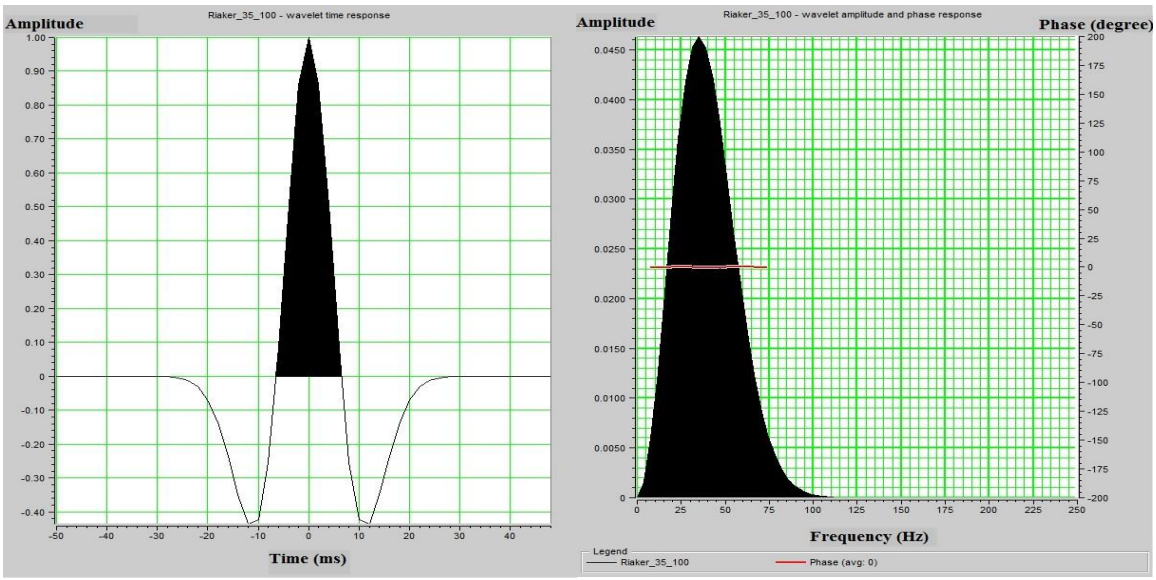

Fig. 2.2. A designed Ricker wavelet (left) for the first model and its amplitude spectrum in frequency domain (right), 35Hz dominant frequency, zero phase, and 2ms sampled.

2.1.4 Synthetic CMP gather generation

There are many ways to generate a synthetic common-midpoint (CMP) gather with modeled parameters such as incident angle, densities, and elastic moduli. Applying the Zoeppritz equations (Zoeppritz, 1919, Appendix A) is one possible way to develop convolution models to acquire the amplitudes of reflected and transmitted waves of designed models. The linear approximation of Zoeppritz equation, which was derived by Bortfeld (1961) and then refined by Richards and Frasier (1976) and Aki and Richards (1980) for intuitive understanding of the AVO process, could also be used for generating CMP gather. Elastic wave modeling, another synthetic CMP gather generating method, provides the exact solution for a plane wave propagating through a series of layers (Kennett, 1979, 1980). Computation of the full elastic wave, including all effects such as primaries, multiples, and converted waves, could be possible with the Elastic wave modeling (Simmons et al., 1994). However, only Zoeppritz equations are applied in the thesis for the simplicity of models. On track 4, track 5, and at the rightmost track in Figure 2.3, the profiles of Poisson's ratio of the first model and corresponding reflectivity series, zero-offset synthetic seismogram, and the designed Ricker wavelet (35Hz dominant frequency, 100ms length) are newly generated before applying the Zoeppritz equations. By implementing the Zoeppritz equation with the set parameters of the model, the uncorrected synthetic CMP gather is generated (Figure 2.4). Below are designed parameters for the synthetic CMP modeling of the first model:

- Target zone: 0 ~ 2400 (m), Target boundary: 1200 (m)
- Geometric spreading, transmission losses, array effects and muting of post-critical events are not applied.
- Number of offset: 11
- Offset range: 0 ~ 3600 (m), Trace interval: 360 (m)

- Model blocking: travel-time (slowness) average
- Time window to model: 0 ~ 2500 (ms)
- Processing sample rate: 1 (ms)
- Output domain: time
- Output sample rate: 2 (ms)

The reason for setting the offset length as 3600 meter is to set offset length as three times of the depth of target boundary, which represents the top of gas-saturated bed, 1200 meter, for observing details of far offset events.

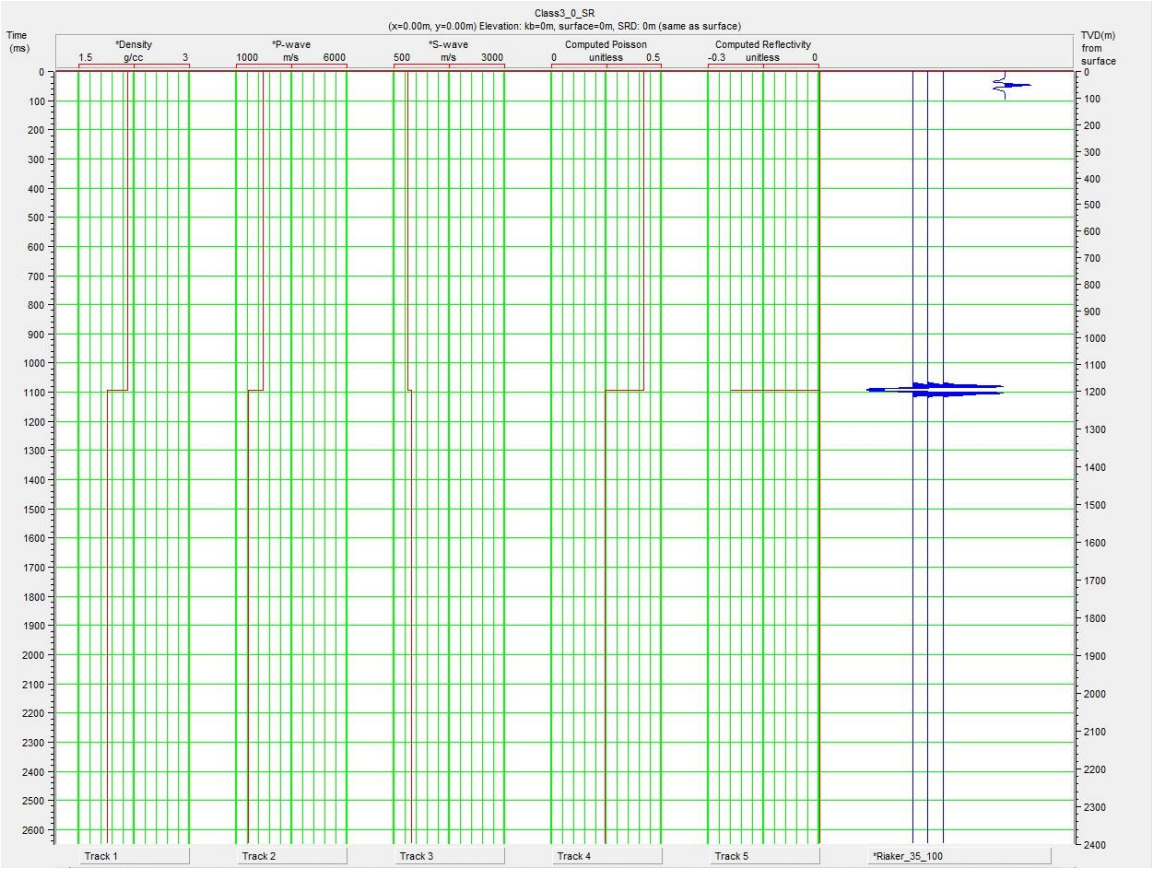

Fig. 2.3. Profiles of computed Poisson's ratio (track 4) and reflectivity series (track 5) of the first model including zero-offset synthetic seismogram with the generated 35Hz Ricker wavelet (blue colored one).

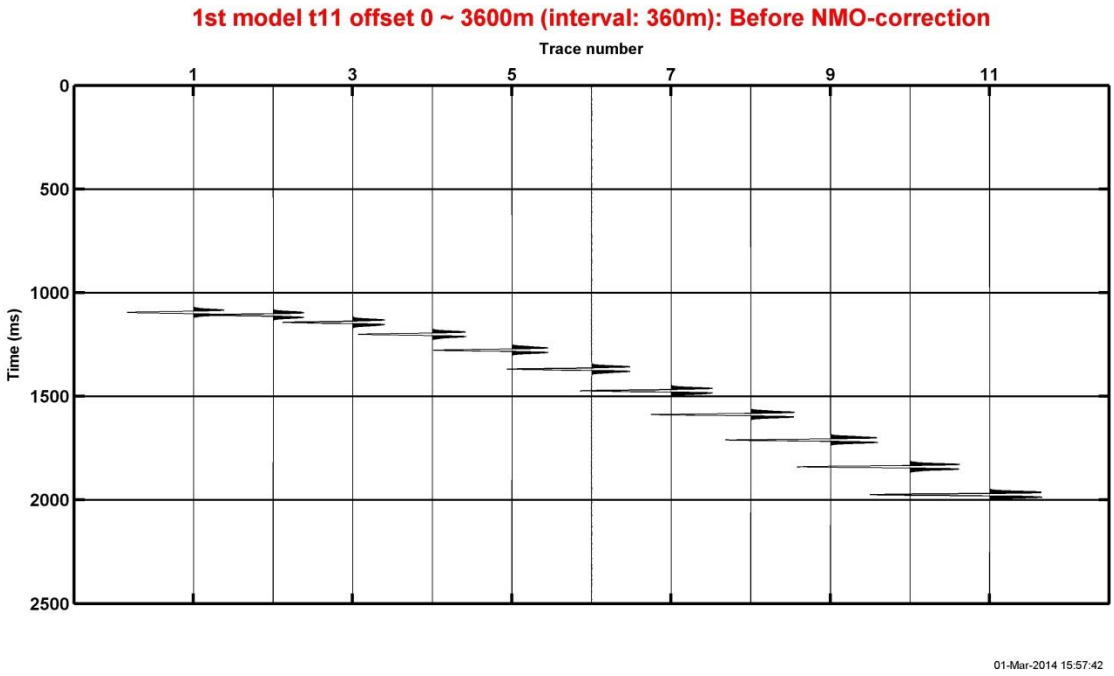

Fig. 2.4. Synthetic CMP gather of the first model: 11 trace numbers and 3600 meter offset length.

2.1.5 NMO-correction and spectral analysis

The NMO-corrected CMP gather of the first model is achieved by using NMO-velocity information acquired from elaborate velocity analysis. The velocity information will also be used to compute Dunkin and Levin's Stretch-ratio (1973, Appendix B) for the first model, in the following section 2.1.6. The NMO-corrected CMP gather is shown in Figure 2.5 and its targeted section, 1000 ~ 1200 milliseconds, is magnified in Figure 2.6 in order to show the degree of NMO-stretch as a function of offset. Spectral analyses on the achieved NMO-corrected CMP gather are implemented for determining waveform changes along with the offset. However, for quantitative analysis, it is necessary to compare not only the waveform changes of each trace on NMO-corrected CMP gather with offset, but also the changes between NMO-corrected trace and un-corrected trace at certain offsets. All eleven traces of both un-corrected and NMO-corrected

CMP gathers are windowed for determination of waveform changes (Figures 2.7 and 2.9). Analysis of un-corrected CMP gather is described in Figure 2.8. Although corresponding maximum amplitudes of traces increase along with offset increase due to AVO Class 3 gas anomaly, the dominant frequencies of amplitude spectra of every trace are almost identical to the dominant frequency (35Hz) of the designed Ricker wavelet described in Figure 2.2. The amplitude spectra after conducting NMO-correction are displayed in Figure 2.10. Each colored spectrum in Figure 2.8 and 2.10 corresponds to the same colored window in Figure 2.7 and 2.9. As shown in the results, even though the alignment of the reflection events on the CMP gather is properly corrected by NMO-correction for removing the offset dependency of the timing in the reflectivity sequence, we could observe that an increase in low frequency content of amplitude spectrum occurs with an increasing offset of the NMO-corrected CMP gather on account of inherent non-linear tendency of NMO-correction. Far offset traces have relatively lower frequency content compared to near offset traces after applying NMO-correction. Figure 2.11 describes zero-offset synthetic seismogram which is already illustrated in Figure 2.3. The stacked trace of NMO-corrected CMP gather is also described in Figure 2.12. For a detailed comparison, the targeted time range of both traces is magnified in Figures 2.13 and 2.14. From the comparison between the amplitude spectrum of zero-offset synthetic seismogram (Figure 2.15) and the amplitude spectrum of the stacked trace of NMO-corrected CMP gather (Figure 2.16), the tendency of waveform change can be shown qualitatively; low frequency content increase on stacked trace after NMO-stacking. The dominant frequency of zero-offset synthetic seismogram is similar to the dominant frequency of designed Ricker wavelet, 35Hz, in Figure 2.2. On the contrary, the dominant frequency of stacked trace is shifted towards lower frequencies. This illustrated distortion causes poor resolution on the post-stack seismogram and creates severe difficulties, not only in the field of interpretation, but also in the image processing, especially, for imaging structural and stratigraphic complexities in the Earth's subsurface.

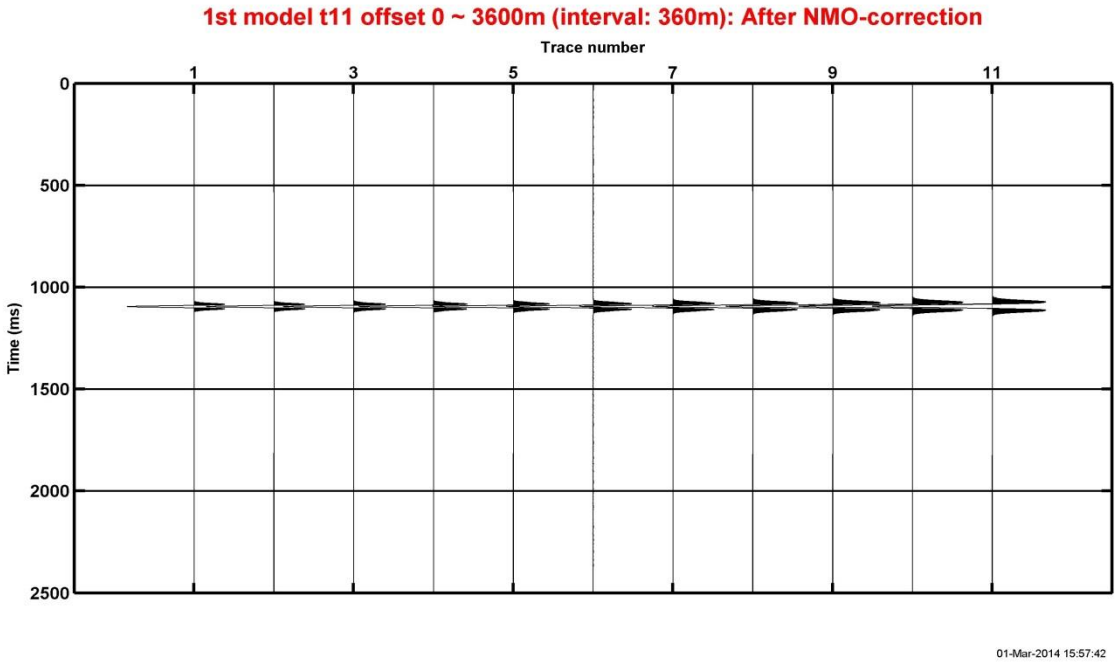

Fig. 2.5. NMO-corrected synthetic CMP gather of the first model.

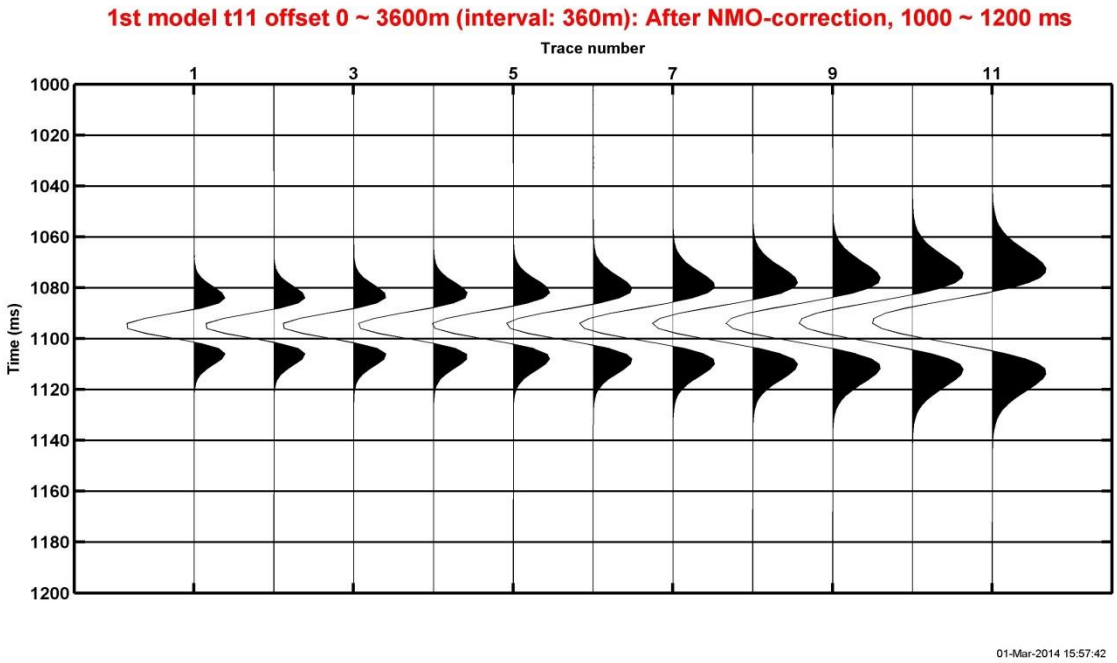

Fig. 2.6. A targeted section of NMO-corrected synthetic CMP gather of the first model, 1000 ~ 1200 milliseconds, is magnified.

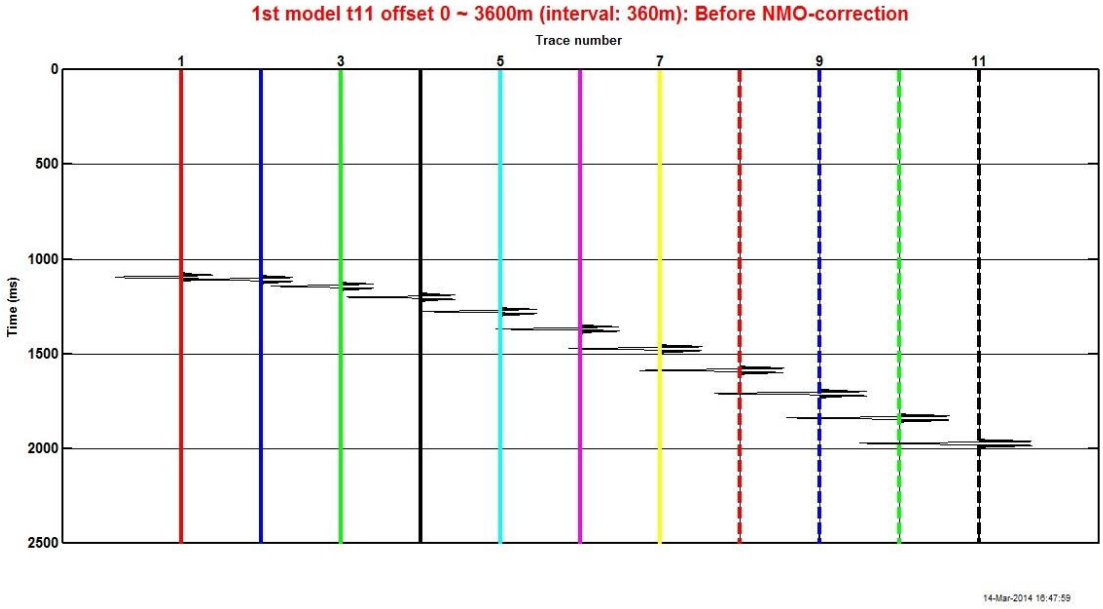

Fig. 2.7. Un-corrected CMP gather, every trace is selected for spectral analysis of the first model.

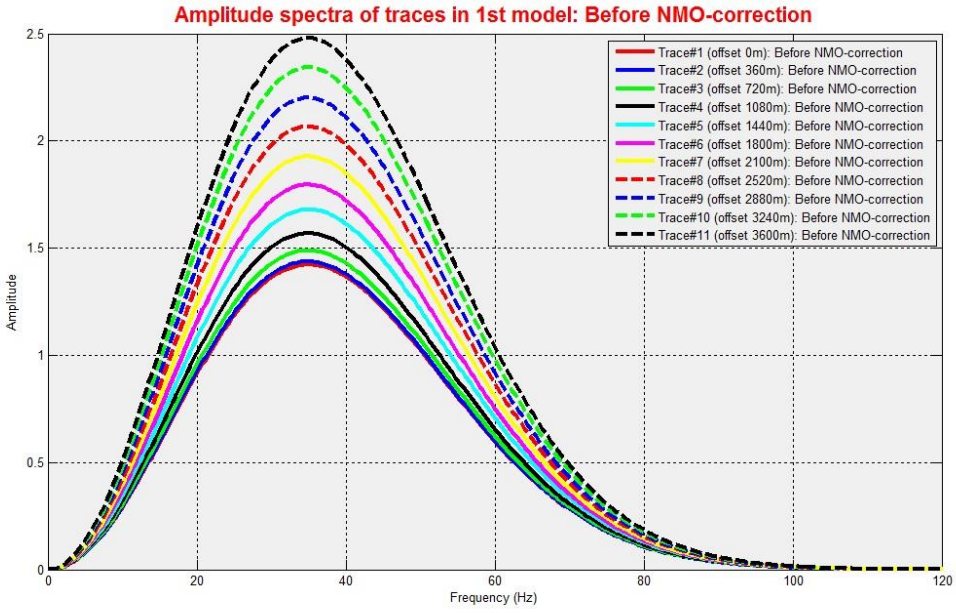

Fig. 2.8. Amplitude spectra of selected traces in Figure 2.7. Each colored spectrum corresponds to the same colored window in Figure 2.7.

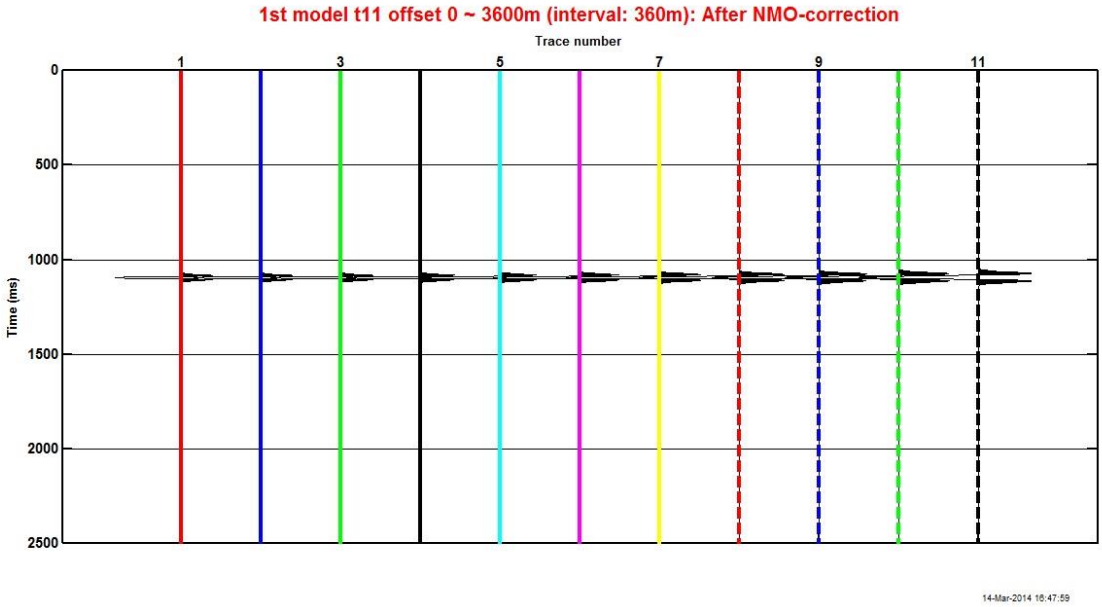

Fig. 2.9. NMO-corrected CMP gather, every trace is selected for spectral analysis of the first model.

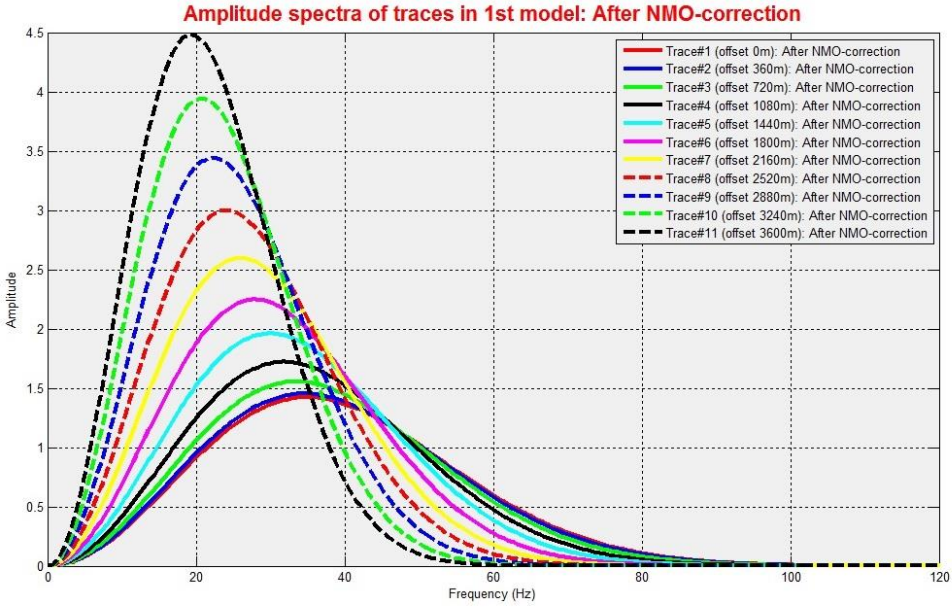

Fig. 2.10. Amplitude spectra of selected traces in Figure 2.9. Each colored spectrum corresponds to the same colored window in Figure 2.9.

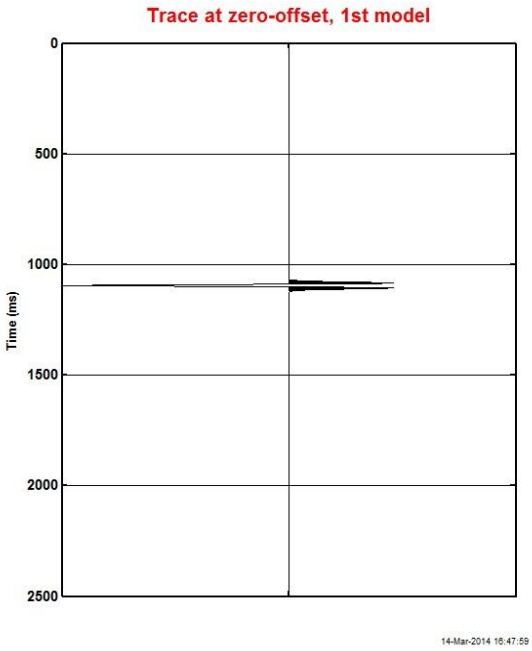

Fig. 2.11. Zero-offset Synthetic Seismogram.

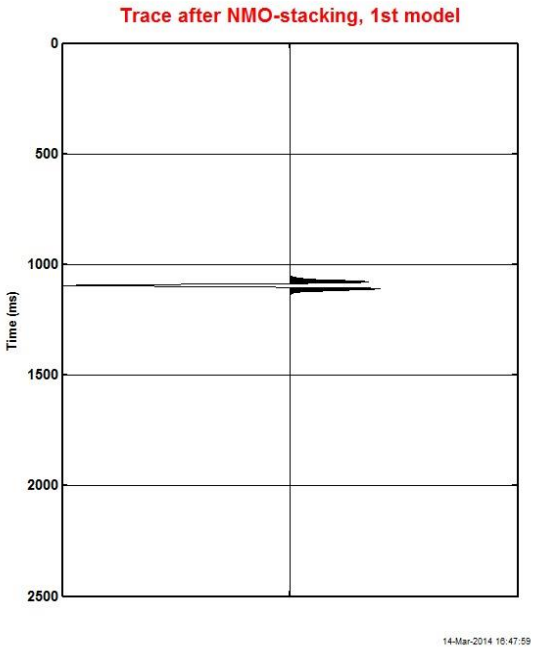

Fig. 2.12. Stacked trace of NMO-corrected CMP gather.

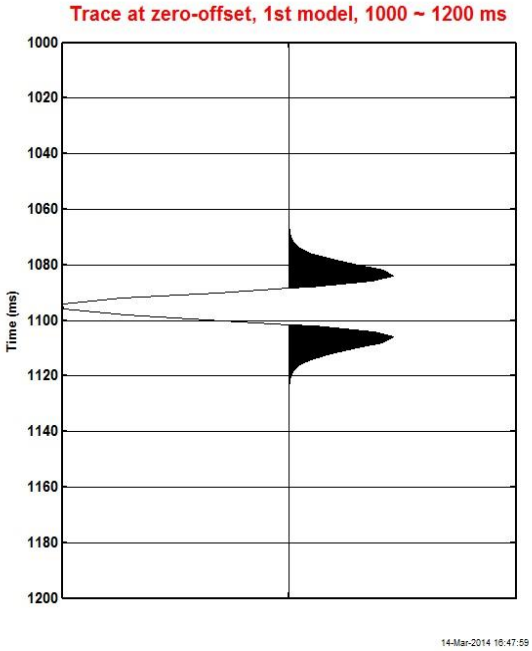

Fig. 2.13. Zero-offset Synthetic Seismogram, 1000 ~ 1200 milliseconds.

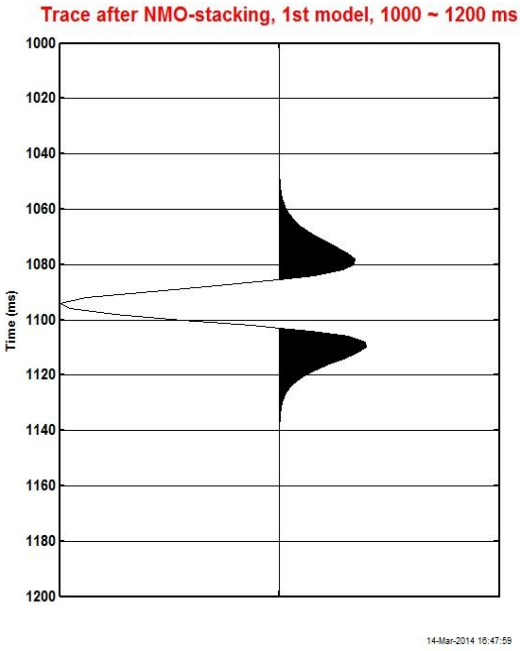

Fig. 2.14. Stacked trace of NMO-corrected CMP gather, 1000 ~ 1200 milliseconds.

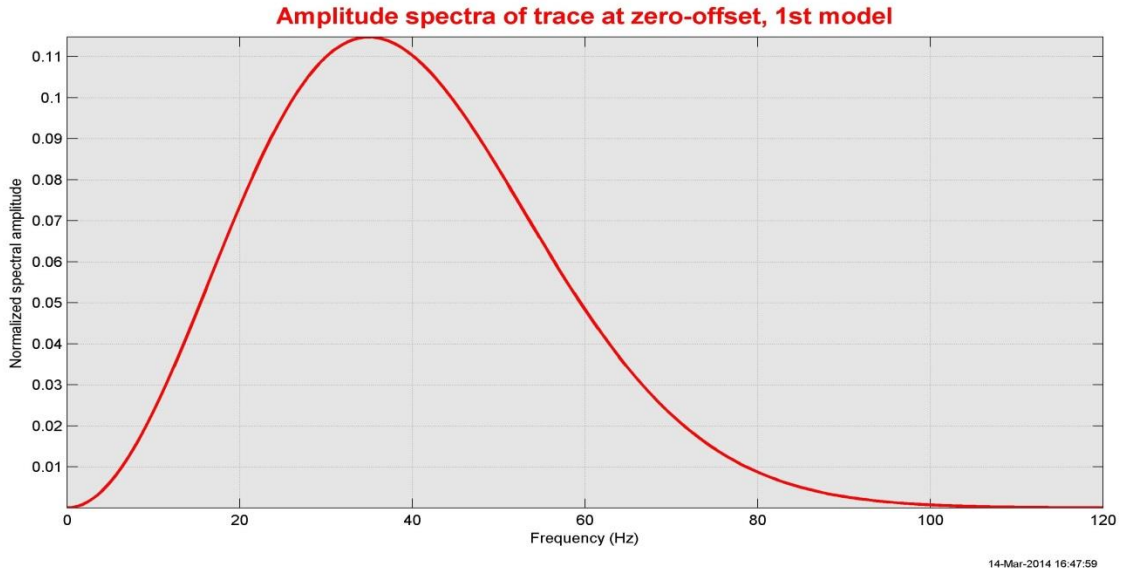

Fig. 2.15. Amplitude spectrum of zero-offset synthetic seismogram in Figure 2.11. Amplitudes are normalized with its maximum amplitude.

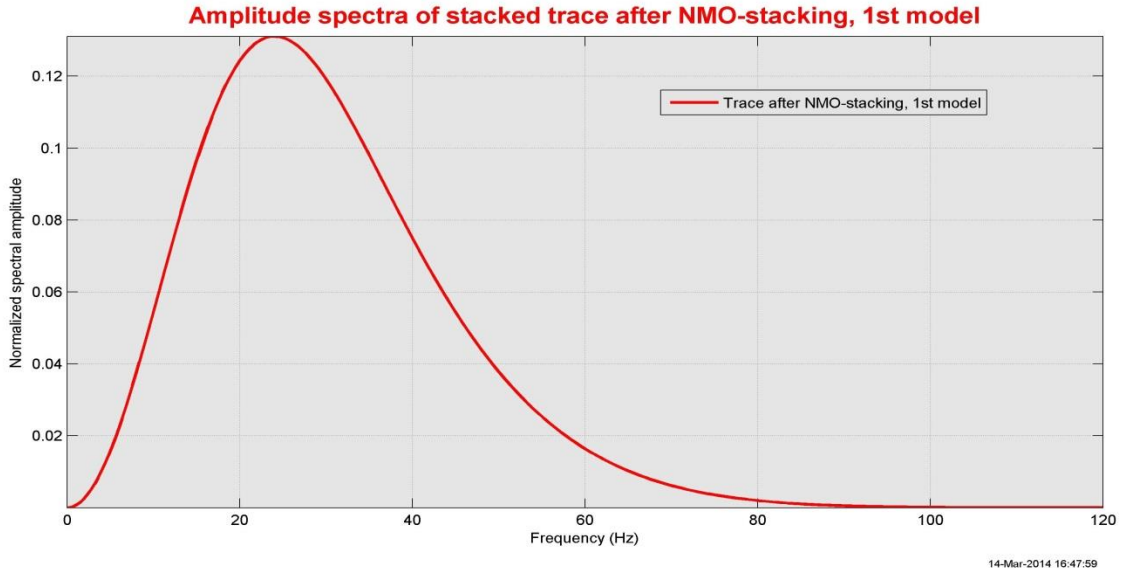

Fig. 2.16. Amplitude spectrum of stacked trace of NMO-corrected CMP gather in Figure 2.12. Amplitudes are normalized with its maximum amplitude.

2.1.6 Investigation of waveform changes

Along with the results of spectral analyses described in Figure 2.8 and 2.10, variable densities of amplitude spectra of every trace on the gather of the first model are also illustrated in Figure 2.17 (before applying NMO-correction) and Figure 2.18 (after applying NMO-correction) to show the NMO-stretch effect. Additionally, in order to determine waveform changes of the first model, the dominant frequencies of both traces of CMP gathers before and after applying NMO-correction are plotted in Figure 2.19. The dominant frequencies of un-corrected traces are changed according to increase in offset. On the other hand, the dominant frequencies of NMO-corrected traces are significantly changed with an increase in offset. Again, although NMO-correction removes the offset dependency of the timing in the reflectivity sequence and aligns the reflectivity events as zero-offset events correctly, it also generates another offset dependency, referred to as waveform distortion or NMO-stretch, as its side effect. To determine the offset dependency more accurately and devise a methodology for correction, discrepancies between dominant frequencies of un-corrected traces and NMO-corrected traces at the same offsets are computed in Figure 2.20. Dunkin and Levin's Stretch-ratios (1973, Appendix B) of every trace on NMO-corrected gather are also computed with offset (Figure 2.21). Naturally, the discrepancy and Stretch-ratios increase with the increase in offset. Table 2.2 describes the dominant frequency of un-corrected traces and it of NMO-corrected trace which are plotted in Figure 2.19. It also includes the discrepancies shown in Figure 2.20 and the Stretch-ratios illustrated in Figure 2.21 along with offset. Both traces located on farthest offset, 3600 meter, before and after applying NMO-correction are illustrated in Figure 2.22 and 2.23 for comparison and understanding of waveform changes arising from the effect of NMO-correction, since the changes would occur most seriously on the farthest offset on CMP gather. Figure 2.22 illustrates the amplitude spectra of both un-corrected (red) and NMO-corrected trace (blue) on the farthest offset. The traces are described in the time

domain (Figure 2.23). In order to observe details of wavelets and compare their differences, the wavelets are time-shifted with each end of wavelets as a standard for the shift in time (Figure 2.24). Significant waveform changes can be observed at the farthest offset both in time and frequency domains.

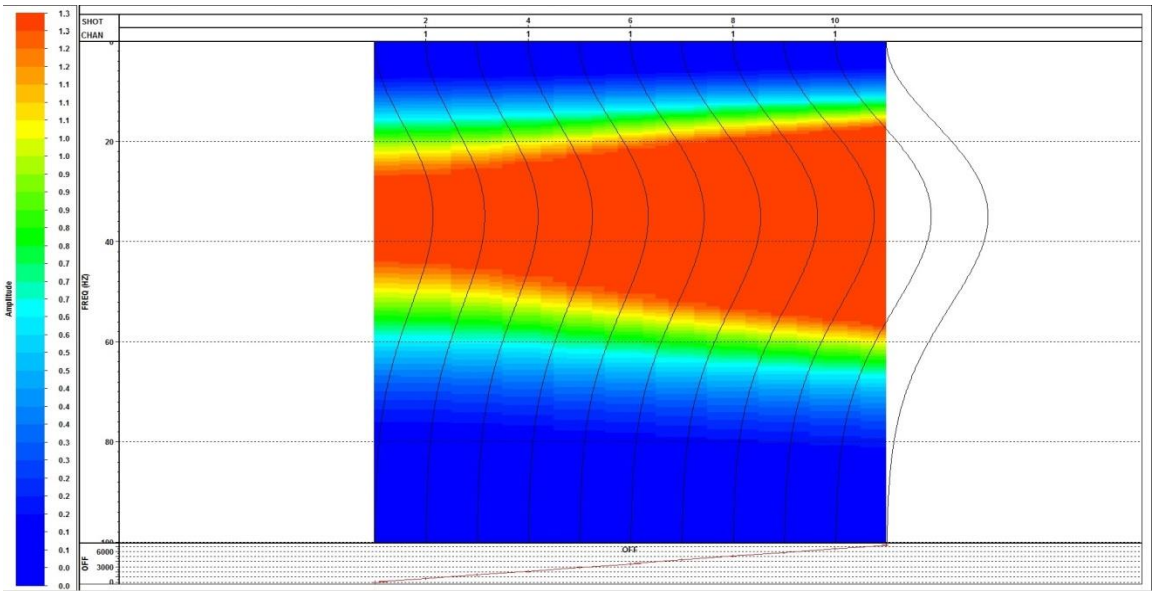

Fig. 2.17. Variable densities of amplitude spectra on CMP gather (Before NMO-correction)

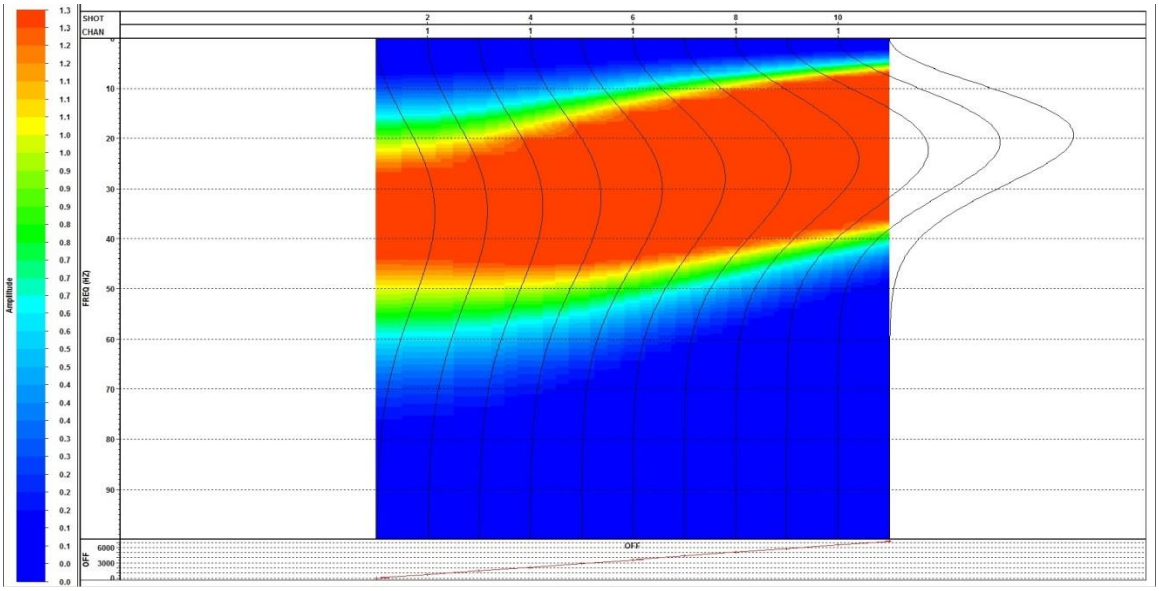

Fig. 2.18. Variable densities of amplitude spectra on CMP gather (After NMO-correction)

Table 2.2. Dominant frequencies of un-corrected (A) and NMO-corrected trace (B) with offset, discrepancies between A and B (C), and Dunkin and Levin's Stretch-ratio (1973) (D).

Offset (m)	A: Dominant frequency of un-corrected traces (Hz)	B: Dominant frequency of NMO corrected traces (Hz)	C: Discrepancy A-B (Hz)	D: Dunkin and Levin's Stretch-ratio
0	35.1719	35.1719	0.0000	1.0000
360	35.1719	34.5723	0.5996	1.0173
720	35.1719	33.5731	1.5988	1.0476
1080	35.1719	31.9744	3.1975	1.1000
1440	35.1719	29.9760	5.1959	1.1733
1800	35.1719	27.9776	7.1943	1.2571
2160	35.1719	25.9792	9.1927	1.3538
2520	35.1719	23.9808	11.1911	1.4667
2880	35.1719	22.3821	12.7898	1.5714
3240	35.1719	20.7834	14.3885	1.6923
3600	35.1719	19.1847	15.9872	1.8333

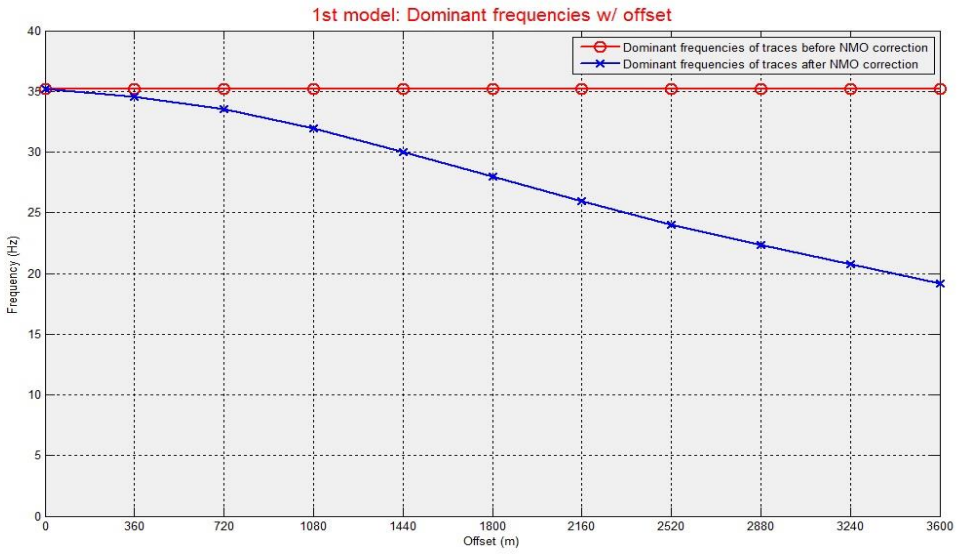

Fig. 2.19. Dominant frequencies of uncorrected and NMO-corrected traces with offset.

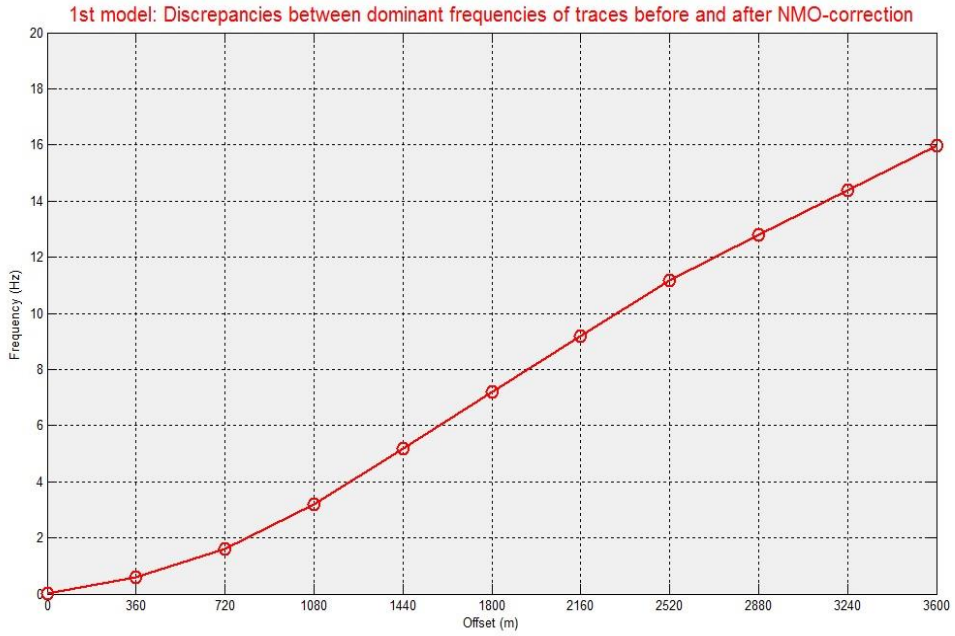

Fig. 2.20. Discrepancy of dominant frequency of NMO-corrected traces from it of un-corrected traces with offset.

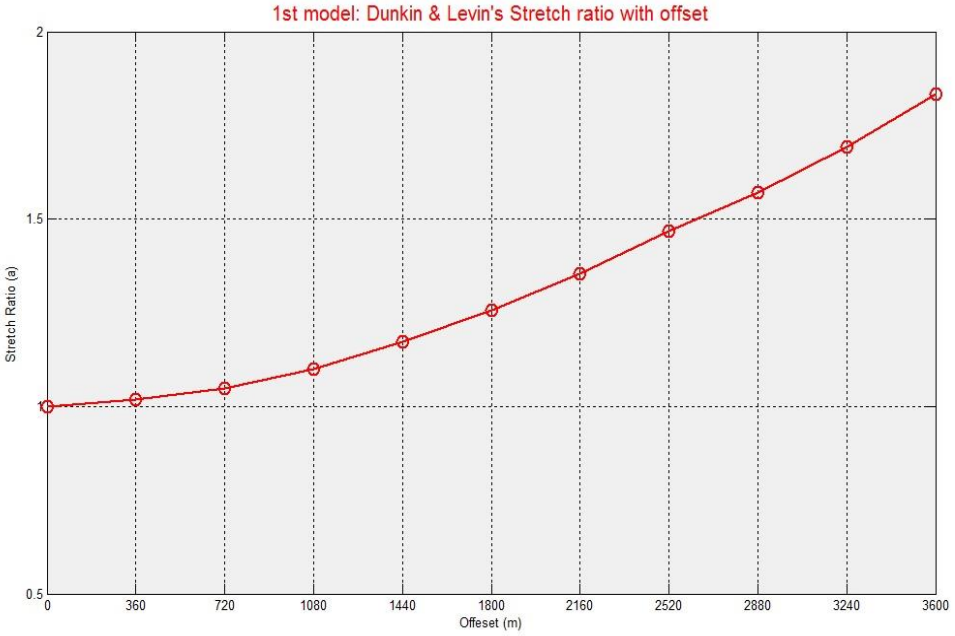

Fig. 2.21. Dunkin and Levin's Stretch-ratios of NMO-corrected traces with offset.

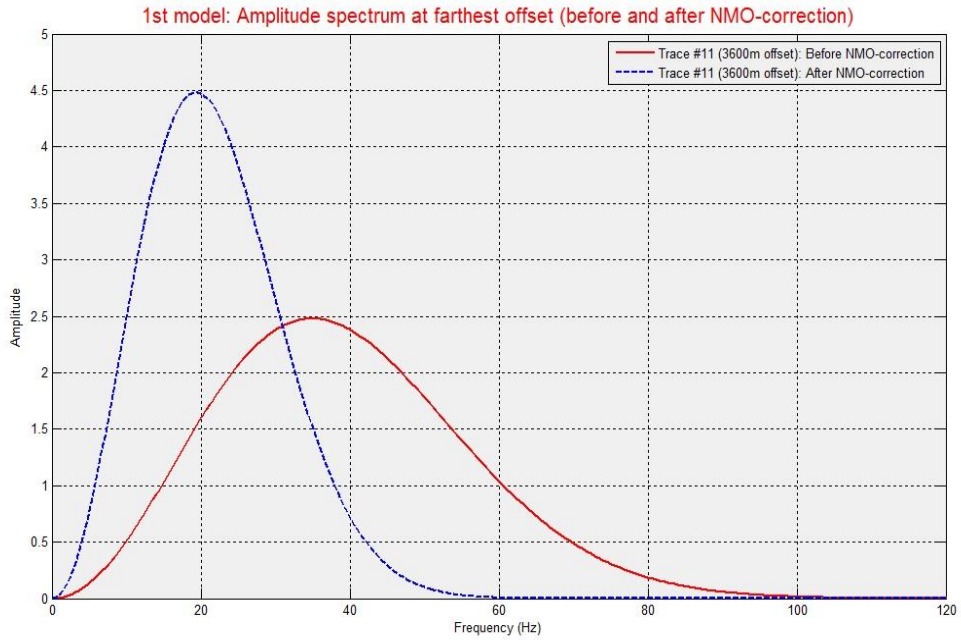

Fig. 2.22. Amplitude spectra of un-corrected (red) and NMO-corrected trace (blue) on the farthest offset, 3600 meter.

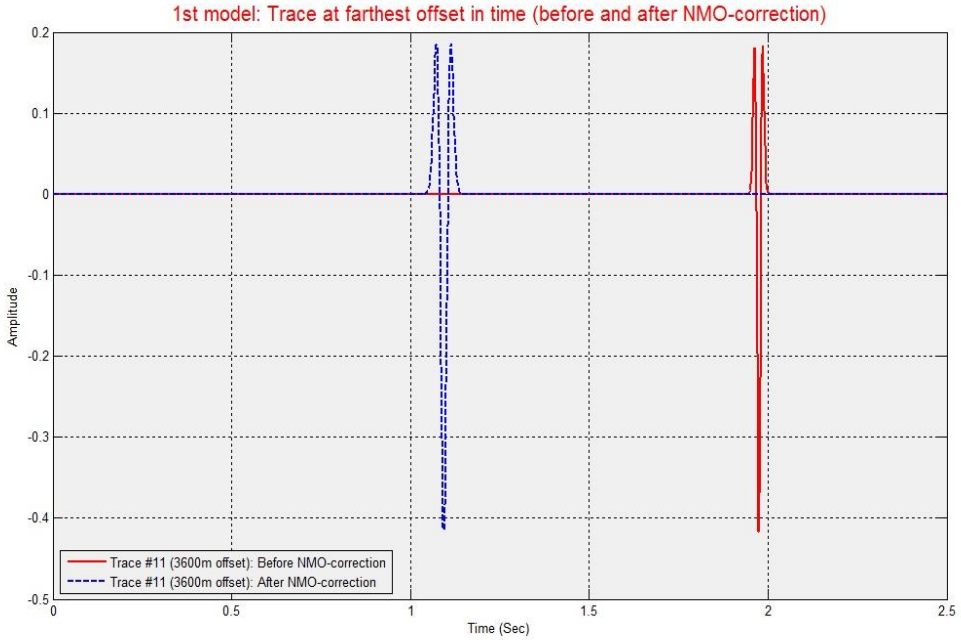

Fig. 2.23. Traces in time-domain before (red) and after (blue) applying NMO-correction on the farthest offset, 3600 meter.

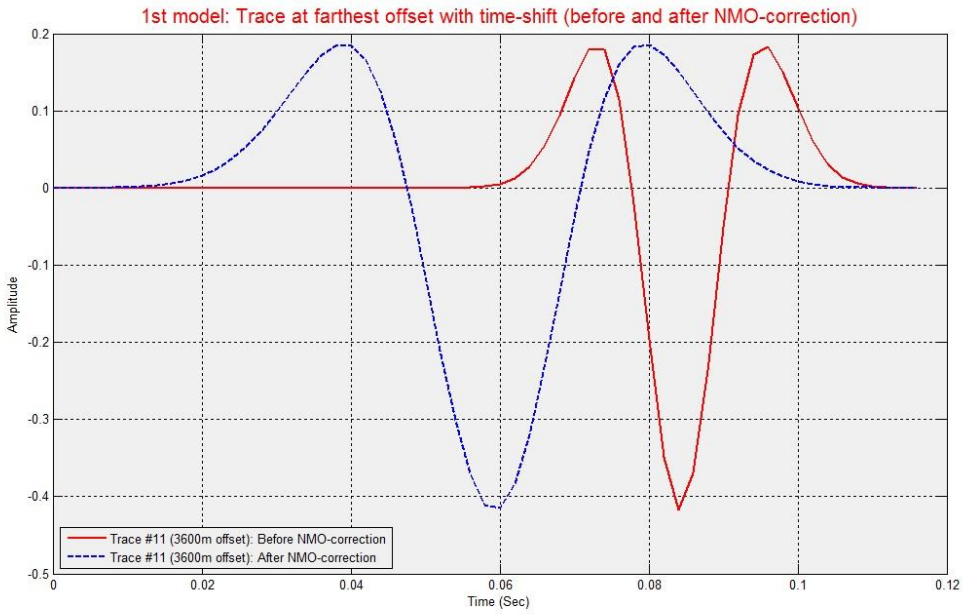

Fig. 2.24. Time-shift of traces described in Figure 2.23**,** each end times of wavelets are used as the standard for the time-shift.

2.2 Investigation of the second model

2.2.1 Model description and generation of synthetic well-logs

The second model set is designed to investigate the degree of NMO-stretch in more specific situations such as typical AVO Class 3, 2, and 1. The model set consists of two models: a model describing gas-saturated beds, corresponding to AVO Classes with specific depth environments, and a model describing brine-saturated beds. To build both models with typical AVO Classes, specific rock properties and depth information concerning each AVO Classes are introduced from a model based on research of the Gulf of Mexico (Hilterman, 2001). The model rock properties in Hilterman are illustrated in Table 2.3 (for AVO Class 3, 1200 meters), Table 2.4 (for AVO Class 2, 2750 meters) and Table 2.5 (for AVO Class 1, 4300 meters).

Table 2.3. Rock properties for AVO Class 3 (bright spot), 1200 meters depth.

Layer	ρ (gm/cm^3)	V_p (ft/s)	V_s (ft/s)	σ
Shale	2.16	7190	2684	0.419
Wet sand	2.11	7000	2820	0.403
Gas sand	1.88	5061	2956	0.241

Table 2.4. Rock properties for AVO Class 2 (phase reversal), 2750 meters depth.

Layer	ρ (gm/cm^3)	V_p (ft/s)	V_s (ft/s)	σ
Shale	2.29	8670	3828	0.378
Wet sand	2.23	10000	5233	0.311
Gas sand	2.08	9165	5462	0.221

Table 2.5. Rock properties for AVO Class 1 (dim out), 4300 meters depth.

Layer	ρ (gm/cm^3)	V_p (ft/s)	V_s (ft/s)	σ
Shale	2.40	10150	4970	0.343
Wet sand	2.32	13500	8048	0.224
Gas sand	2.21	13288	8288	0.182

Shale velocities and densities of the Hilterman's model, which are described in tables above, were generated from selected well-log information in the Gulf of Mexico. Sand velocities and densities were also selected in order to yield reflection amplitudes corresponding to Class 3 (bright spot), 2 (phase reversal), and 1 (dim out) AVO anomalies. For the gas-saturated case of the Hilterman's model, Greenberg-Castagna method (Greenberg and Castagna, 1992) was used to fluid-substitute gas from the brine-saturated situation with fluid properties from Batzle and Wang (1992). To satisfy the objective of investigation for the second model set, the author generates two models concerning gas-saturated and brine-saturated cases by using the rock properties and depth information. For both models, each layers concerning AVO Class 3, 2, and 1 are sequentially located at 1200 meters (for Class 3), 2750 meters (for Class 2), and 4300 meters (for Class 1) on same profiles. Every layer has a 250 meter thickness, although unrealistic, to avoid tuning effect. Shale properties between each two layers are linearly interpolated with the properties and depth information in Hilterman. The synthetic well-logs of both models are described in Figure 2.25 (for gas-saturated case) and in Figure 2.26 (for brine-saturated case). Again, generation of these synthetic well-logs is a prerequisite process for generation of the corresponding synthetic CMP gathers with CGG Veritas' Hampson-Russell. Additionally, both P-wave and S-wave velocity values (ft/s) are converted to slowness ($\mu s/m$) for following LAS format.

2.2.2 Wavelet description

For generation of synthetic CMP gathers of designed models, the Ricker wavelet, which was already used for the first model, is used again. It has 35Hz dominant frequency and 100 milliseconds wavelet length. The Ricker wavelet and its amplitude spectrums in frequency domain are illustrated in Figure 2.2.

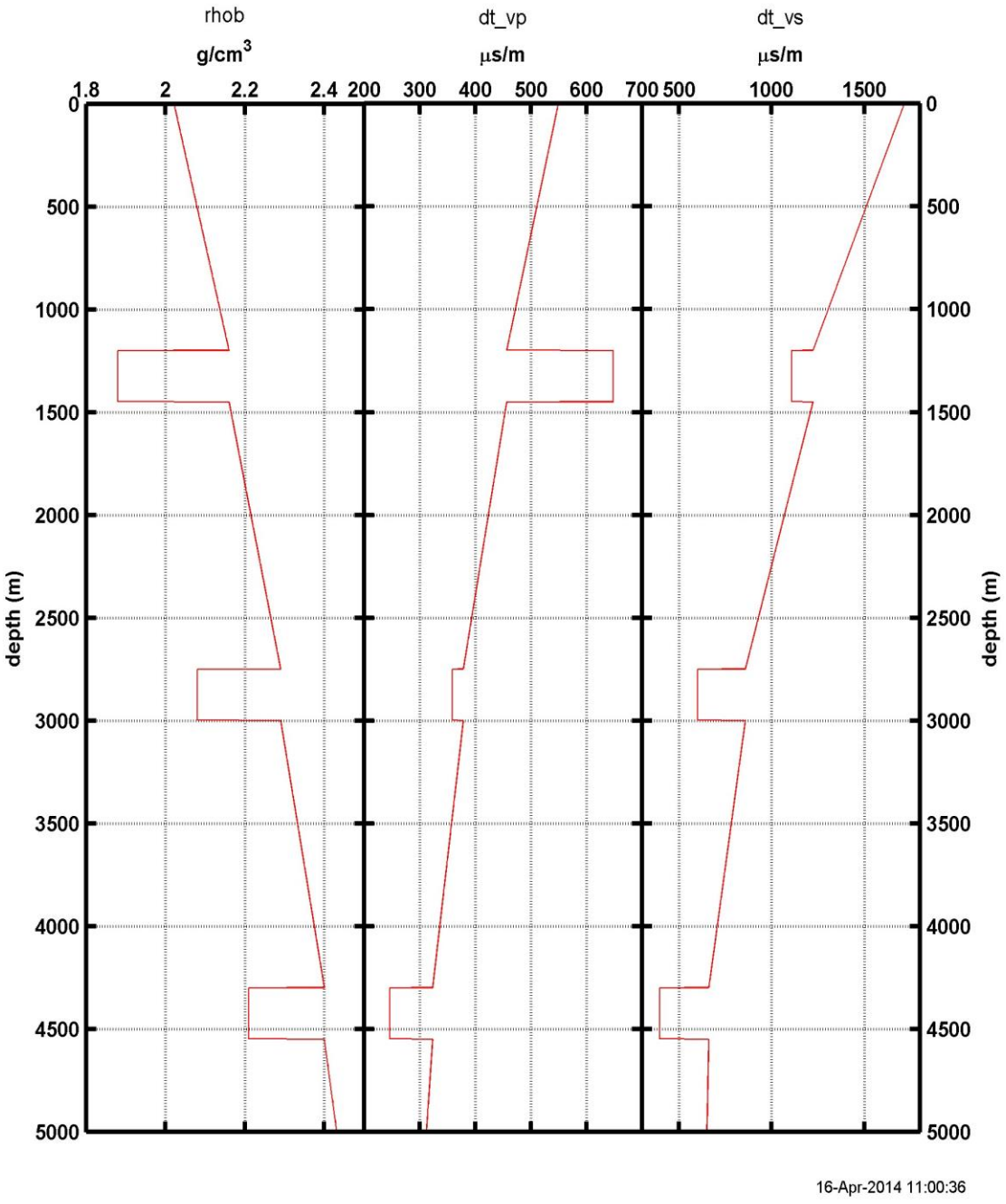

Figure 2.25. Synthetic well-log for gas-saturated case of the second model, generated by merging Class 3 (1st layer, 1200 ~ 1450 meter depth interval), Class 2 (2nd layer, 2750 ~ 3000 meter depth interval), and Class 1 (3rd layer, 4300 ~ 4550 meter depth interval).

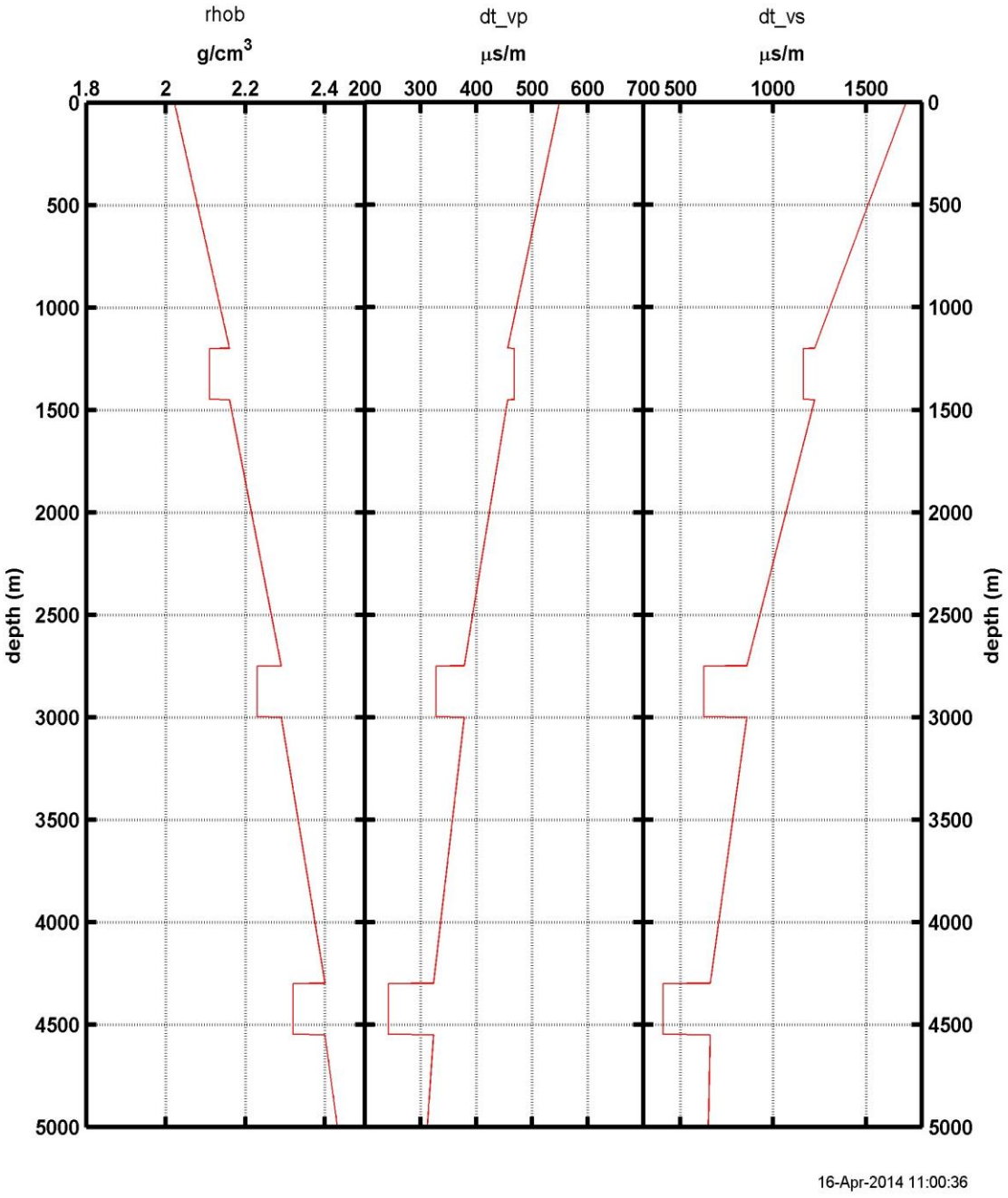

Figure 2.26. Synthetic well-log for brine-saturated case of the second model, generated by merging Class 3 (1st layer, 1200 ~ 1450 meter depth interval), Class 2 (2nd layer, 2750 ~ 3000 meter depth interval), and Class 1 (3rd layer, 4300 ~ 4550 meter depth interval).

2.2.3 Synthetic CMP gather generation

In order to generate synthetic common-midpoint (CMP) gathers of the second model set, the Zoeppritz equations are applied again. Before applying the Zoeppritz equations, the profiles of Poisson's ratio of the second model set and corresponding reflectivity series, zero-offset synthetic seismograms, and the designed Ricker wavelet (35Hz dominant frequency, 100ms length), which are described in track 4, track 5, and at the rightmost track in Figure 2.27 (for the gas-saturated model) and Figure 2.28 (for the brine-saturated model), are newly generated. The synthetic CMP gather corresponding to the gas-saturated case is shown in Figure 2.29. The gather for the brine-saturated model is described in Figure 2.30. In both figures, amplitudes are normalized with the maximum amplitude on the gathers. Below are designed parameters for the synthetic CMP modeling of the second model set:

- Target zone: 0 ~ 5000 (m), Target boundaries: 1200 ~ 1450 (Class 3), 2750 ~ 3000 (Class 2), 4300 ~ 4550 (Class 1) (m)
- Geometric spreading, transmission losses, array effects and muting of post-critical events are not applied.
- Number of offset: 11
- Offset range: 0 ~ 7000 (m), Trace interval: 700 (m)
- Model blocking: 2ms Backus averaging
- Time window to model: 0 ~ 5000 (ms)
- Processing sample rate: 1 (ms)
- Output domain: time, Output sample rate: 2 (ms)

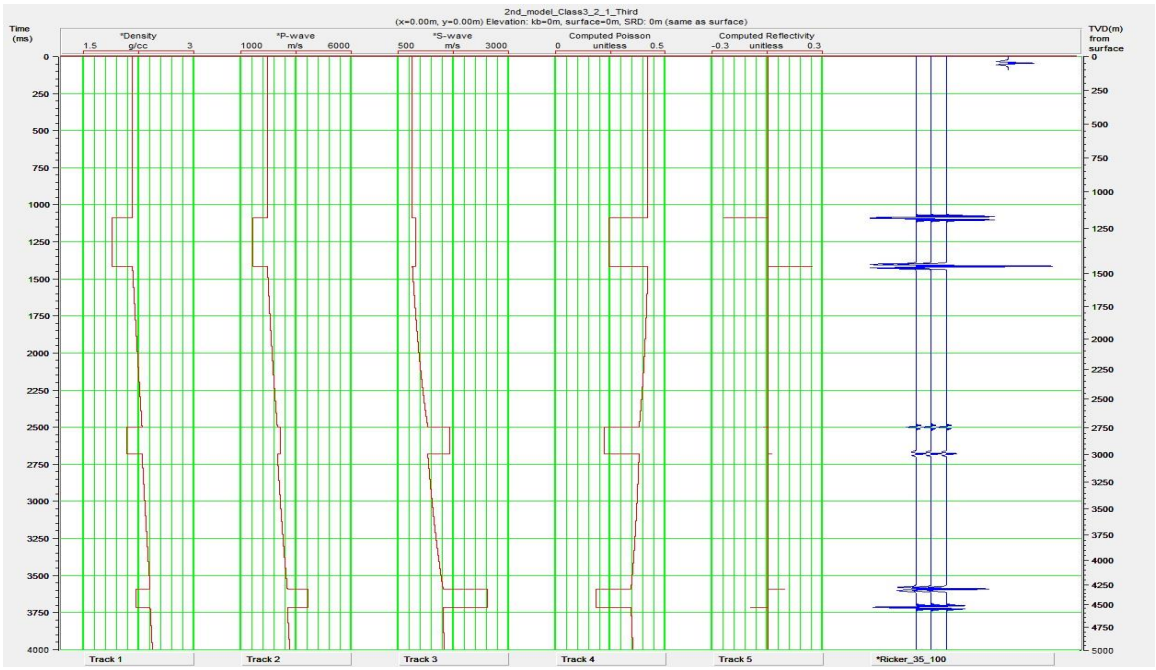

Fig. 2.27. Profiles of computed Poisson's ratio (track 4) and reflectivity series (track 5) of gas-saturated model including zero-offset synthetic seismogram with the generated 35Hz Ricker wavelet (blue colored one).

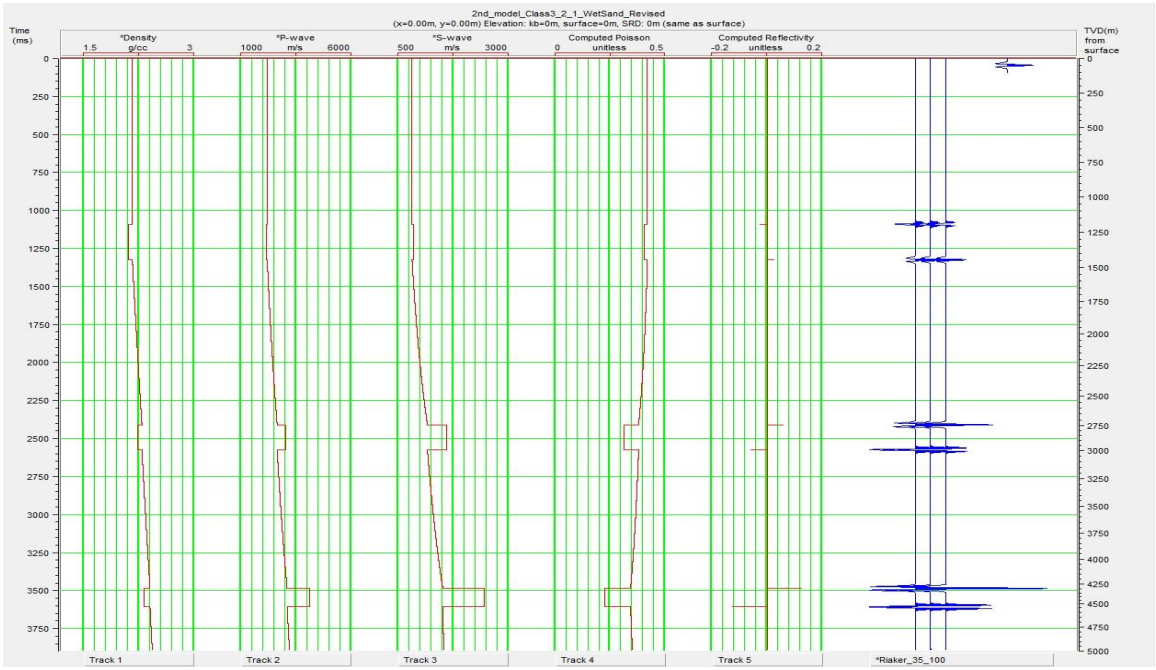

Fig. 2.28. Profiles of computed Poisson's ratio (track 4) and reflectivity series (track 5) of brine-saturated model including zero-offset synthetic seismogram with the generated 35Hz Ricker wavelet (blue colored one).

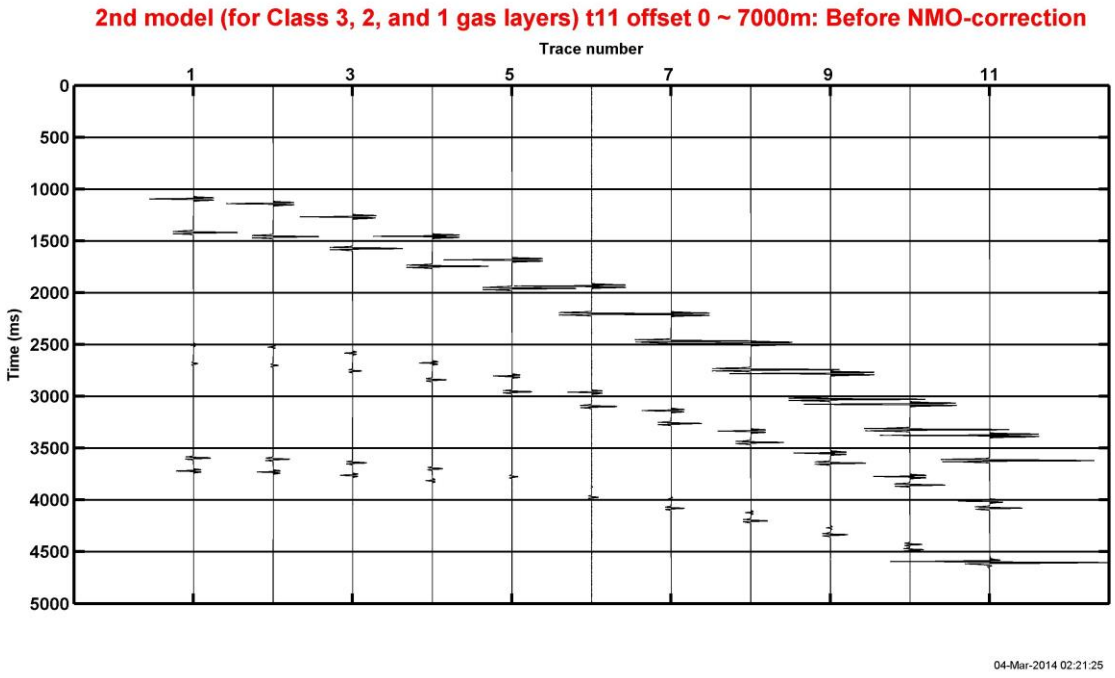

Fig. 2.29. Synthetic CMP gather of gas-saturated model: 11 trace numbers and 7000 meter offset length.

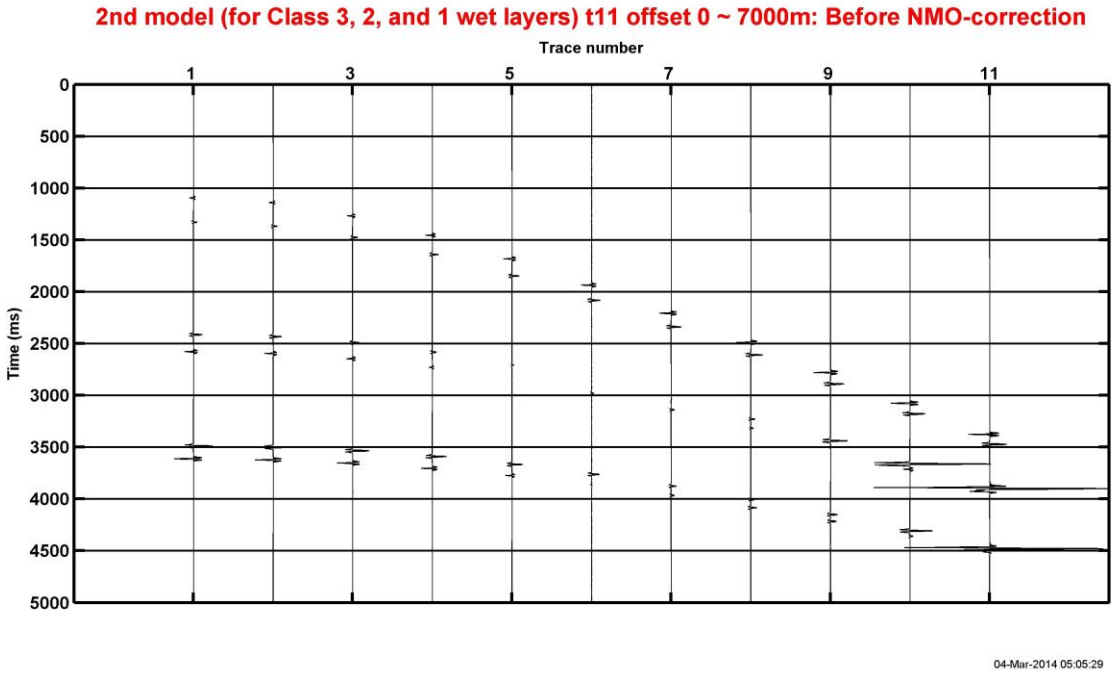

Fig. 2.30. Synthetic CMP gather of brine-saturated model: 11 trace numbers and 7000 meter offset length.

2.2.4 NMO-correction, AVO and spectral analyses

The NMO-corrected CMP gathers of the second model set are achieved by using NMO-velocity information acquired with elaborate velocity analysis. The velocity information will also be used for computing Dunkin and Levin's Stretch-ratio (1973, Appendix B) for this second model set in the following section 2.2.5. The NMO-corrected CMP gathers are shown in Figure 2.31 (for the gas-saturated case) and Figure 2.32 (for the brine-saturated case). Since the objective of this second investigation is to investigate the degree of NMO-stretch in specific situations of typical AVO Class 3, 2, and 1 for both gas-saturated and brine-saturated cases, the second investigation has to be preceded with an investigation of the amplitude variation with offset of each targeted layers corresponding to the top of AVO Class 3, 2, and 1 anomaly for verifying the effectiveness of designed models as models that represent AVO Classes. If the results of AVO in the models are identical to the results of already conducted AVO studies, we could tell the models represent specific AVO cases. Since the 11^{th} traces located at the farthest offset on both gathers (Figure 2.31 and 2.32) include post-critical events, only the first ten traces in 0 to 6300 meter offset ranges are targeted for further investigation. Figure 2.33 shows the results of investigated amplitude variation with offset for the second model sets. It is identical to the reflection-coefficient curves of Rutherford et al. (1989) and Hilterman (2001). Amplitude spectra of traces representing the top of Class 3 gas-saturated layer, described at 1100 milliseconds time in Figure 2.31, is illustrated in Figure 2.34. Other AVO cases are also shown in Figure 2.35 (for Class 2 gas, 2500 milliseconds in Fig. 2.31), Figure 2.36 (for Class 1 gas, 3600 millisecond in Fig. 2.31), Figure 2.37 (for Class 3 wet, 1100 milliseconds in Fig. 2.32), Figure 2.38 (for Class 2 wet, 2400 milliseconds in Fig. 2.32) and Figure 2.39 (for Class 1 wet, 3500 milliseconds in Fig. 2.32). The tendency of waveform changes, shifting toward lower frequencies shown in the first investigation, is also observed in all above figures. More detailed investigations to determine waveform changes follows in section

2.2.5.

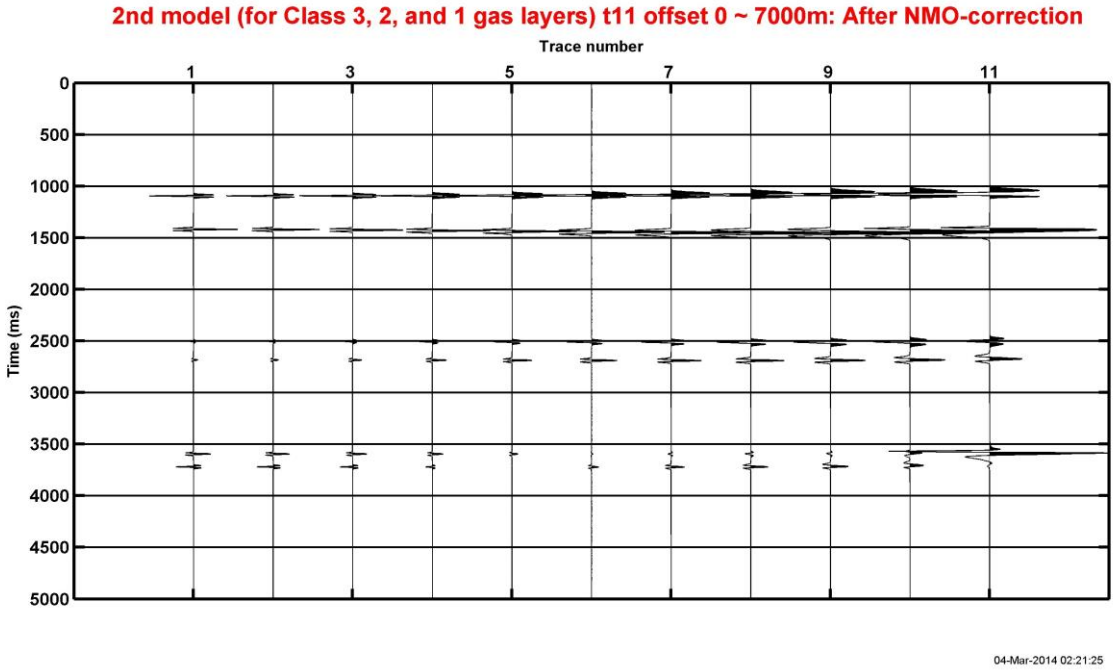

Fig. 2.31. NMO-corrected synthetic CMP gather of the gas-saturated model.

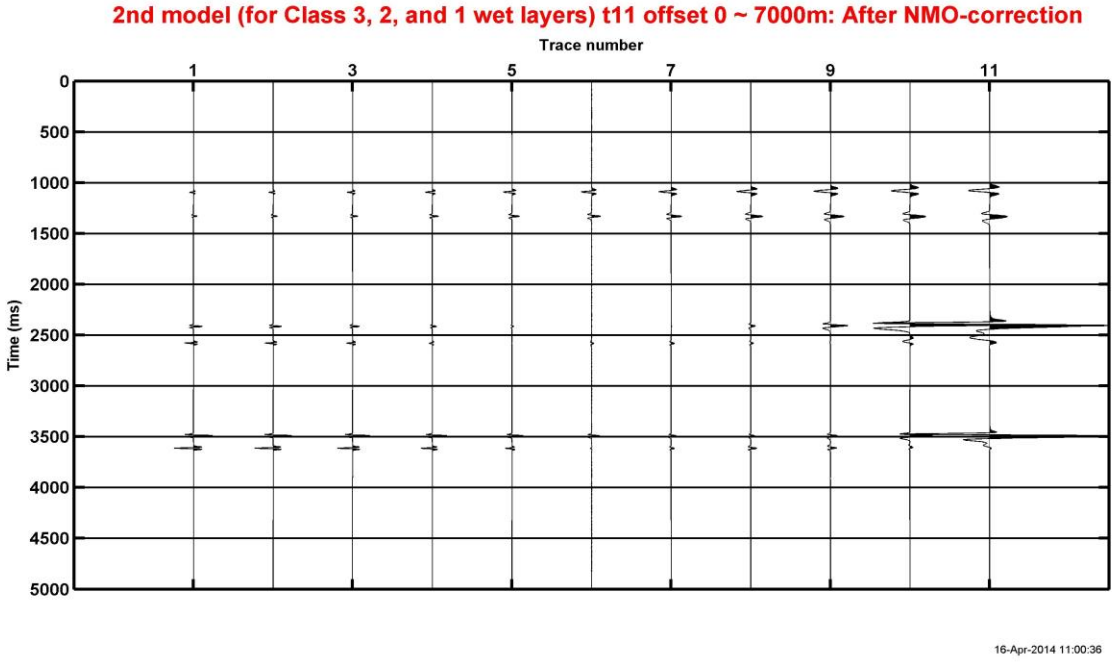

Fig. 2.32. NMO-corrected synthetic CMP gather of the brine-saturated model.

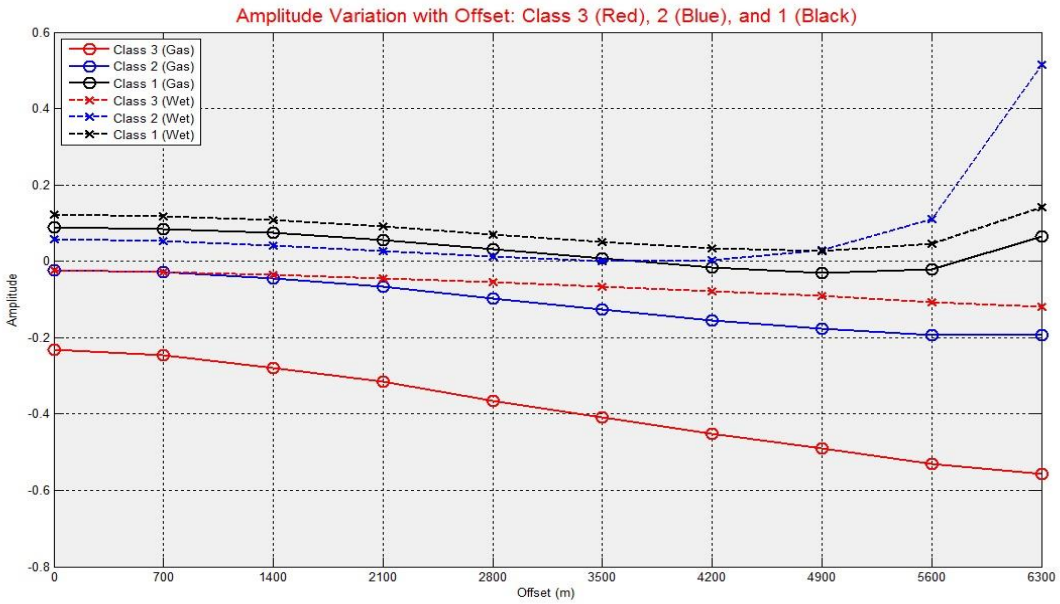

Fig. 2.33. Amplitude variation with offset, reflection-coefficient curves for corresponding top of Class 3 (red), 2 (blue) and 1 (black) for gas-saturated and brine-saturated models. Circle indicates gas-saturated case and x represents brine-saturate case.

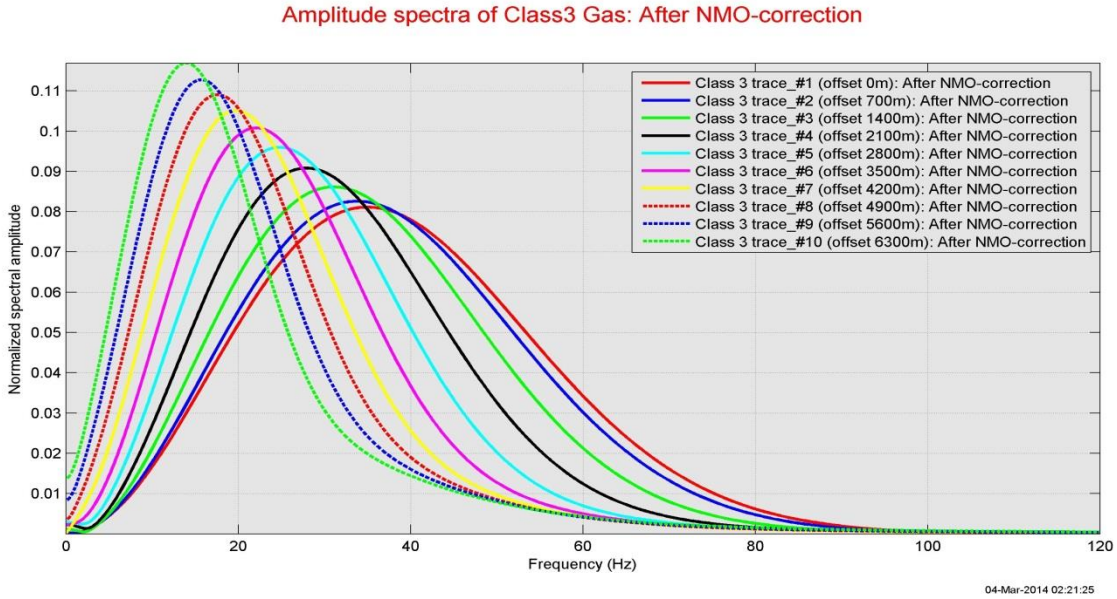

Fig. 2.34. Amplitude spectra of traces corresponding to the top of Class 3 gas-saturated layer, which is described at 1100 milliseconds time in Figure 2.31.

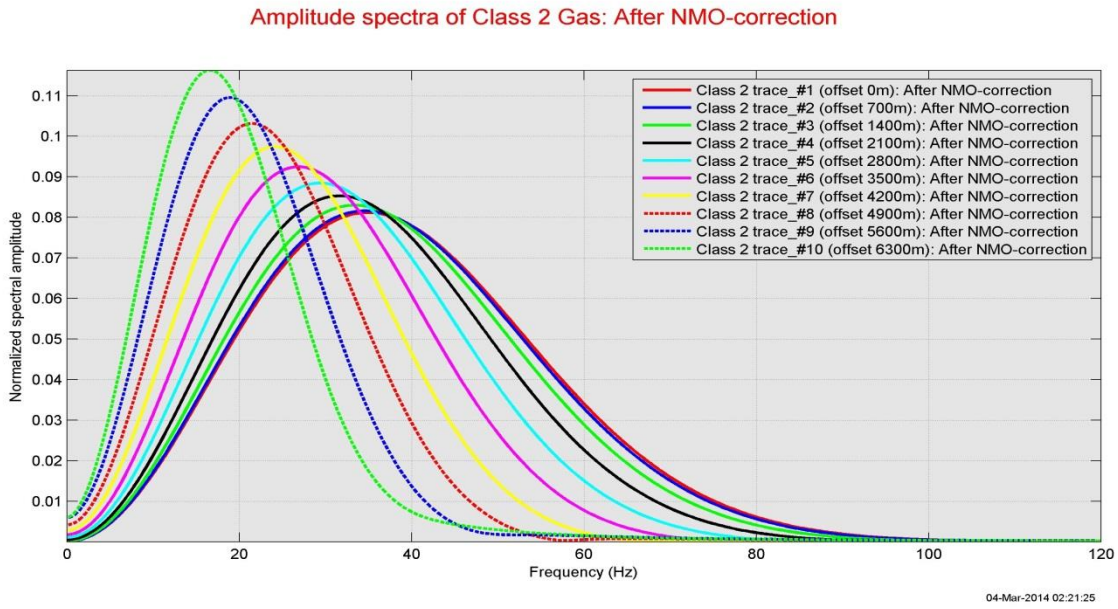

Fig. 2.35. Amplitude spectra of traces corresponding to the top of Class 2 gas-saturated layer, which is described at 2500 milliseconds time in Figure 2.31.

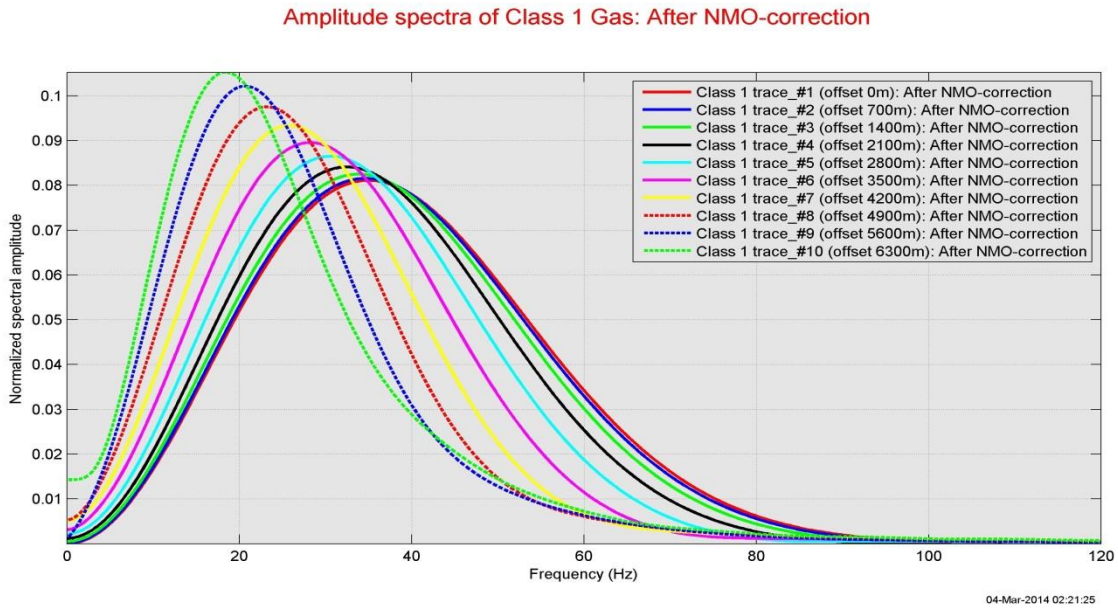

Fig. 2.36. Amplitude spectra of traces corresponding to the top of Class 1 gas-saturated layer, which is described at 3600 milliseconds time in Figure 2.31.

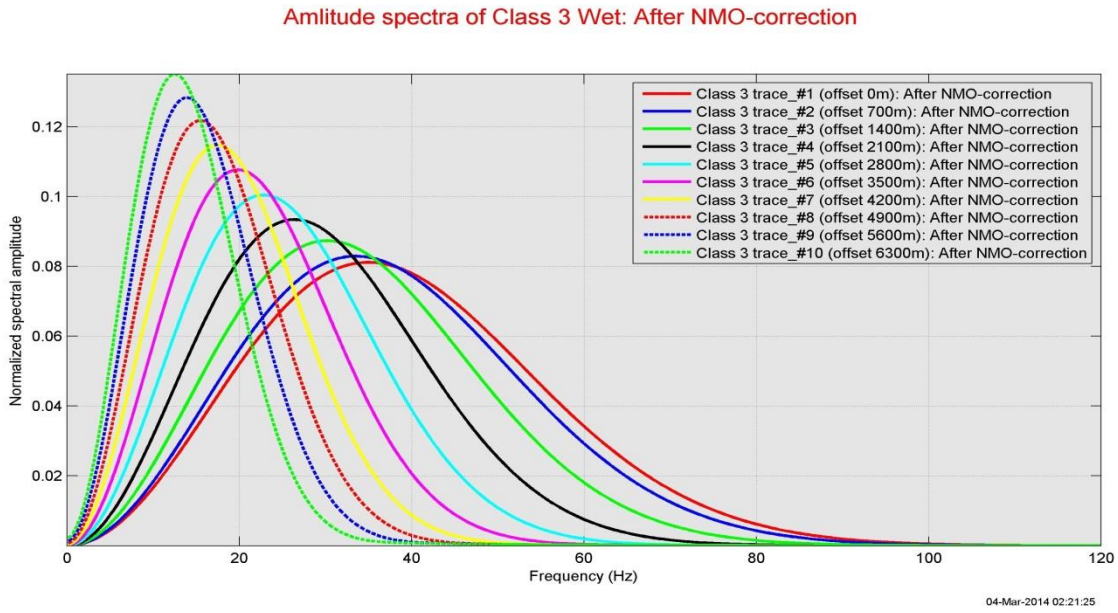

Fig. 2.37. Amplitude spectra of traces corresponding to the top of Class 3 brine-saturated layer, which is described at 1100 milliseconds time in Figure 2.32.

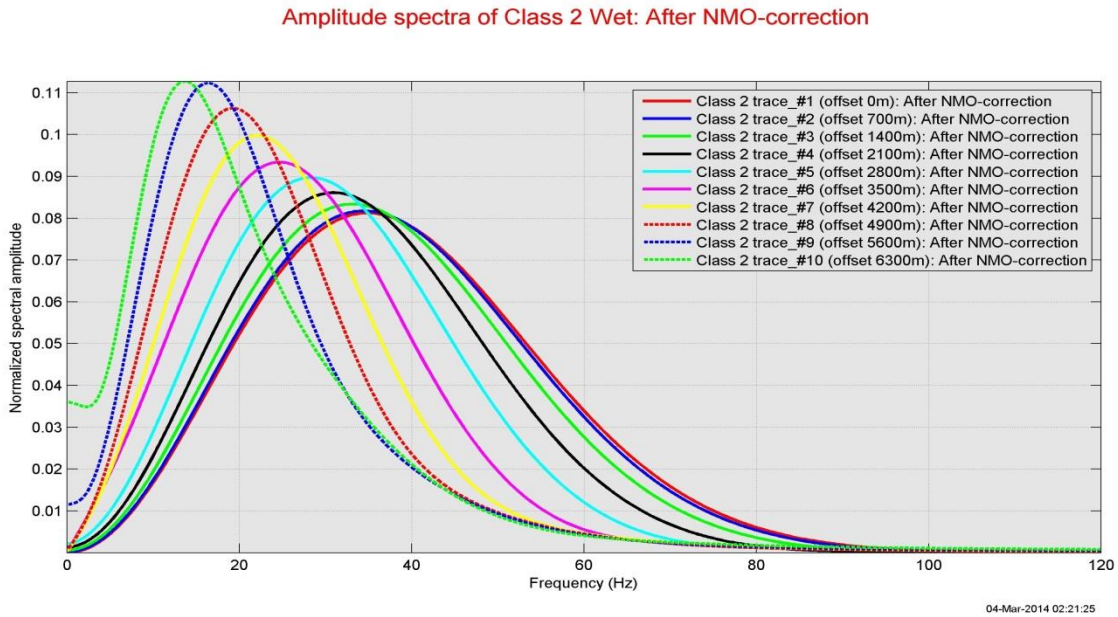

Fig. 2.38. Amplitude spectra of traces corresponding to the top of Class 2 brine-saturated layer, which is described at 2400 milliseconds time in Figure 2.32.

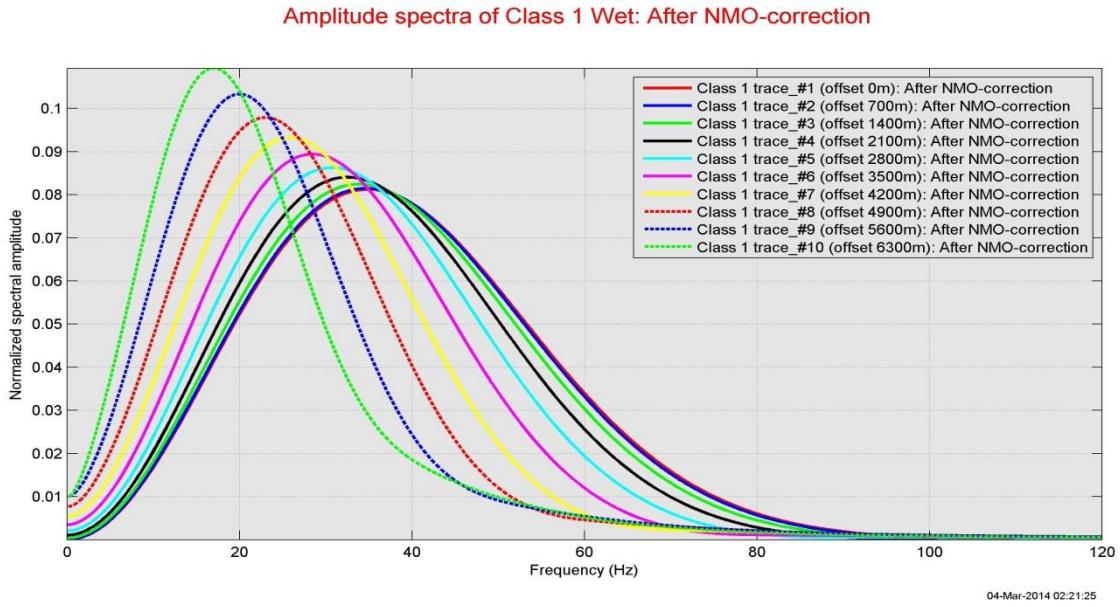

Fig. 2.39. Amplitude spectra of traces corresponding to the top of Class 1 brine-saturated layer, which is described at 3500 milliseconds time in Figure 2.32.

2.2.5 Investigation of waveform changes

The curves of dominant frequencies with offset for the top interface of the six sand beds, described in the section 2.2.4, are shown in Figure 2.40. The dominant frequencies decrease with increase in offset for every case of sand layers. In addition, the layers located at shallower positions have lower values of dominant frequencies at the same offset. That is, with the observation, we could tell that waveform changes from NMO-stretch, shifting from lower frequencies, arise at far offset and shallow depth. However, at this stage, the more important aspect to point out is that gas-saturated sand and brine-saturated sand can be differentiated by investigating dominant frequencies at far offset. In every AVO Class, if the investigated offset is far enough, gas-saturated anomalies are separated from brine-saturated anomaly. With Dunkin

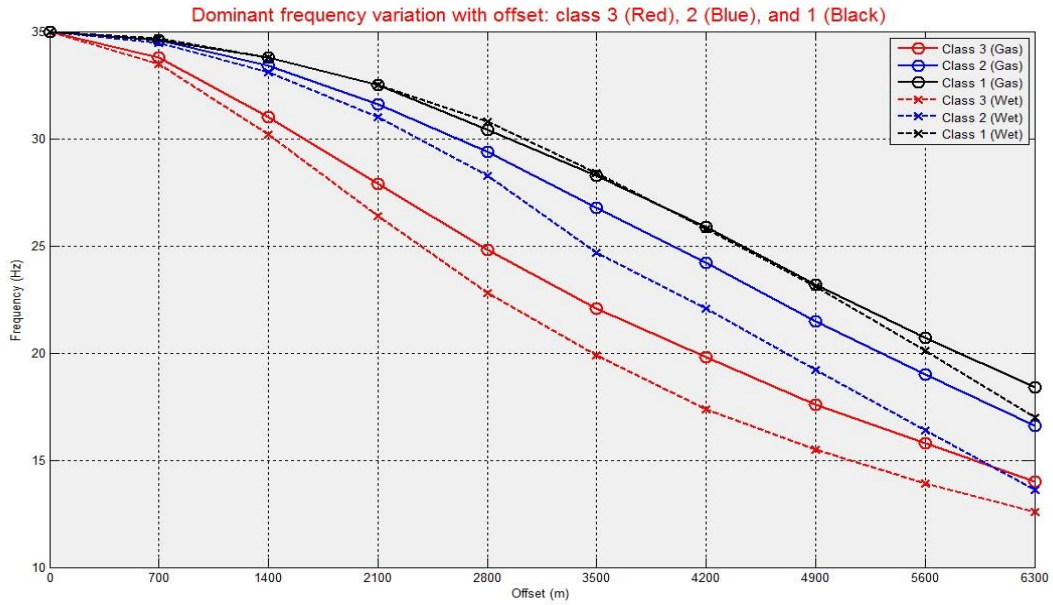

Fig. 2.40. Dominant-frequency variation with offset for corresponding top of Class 3 (red), 2 (blue), and 1 (black) for gas and brine-saturated models. Circle indicates gas-saturated case and x represents brine-saturate case.

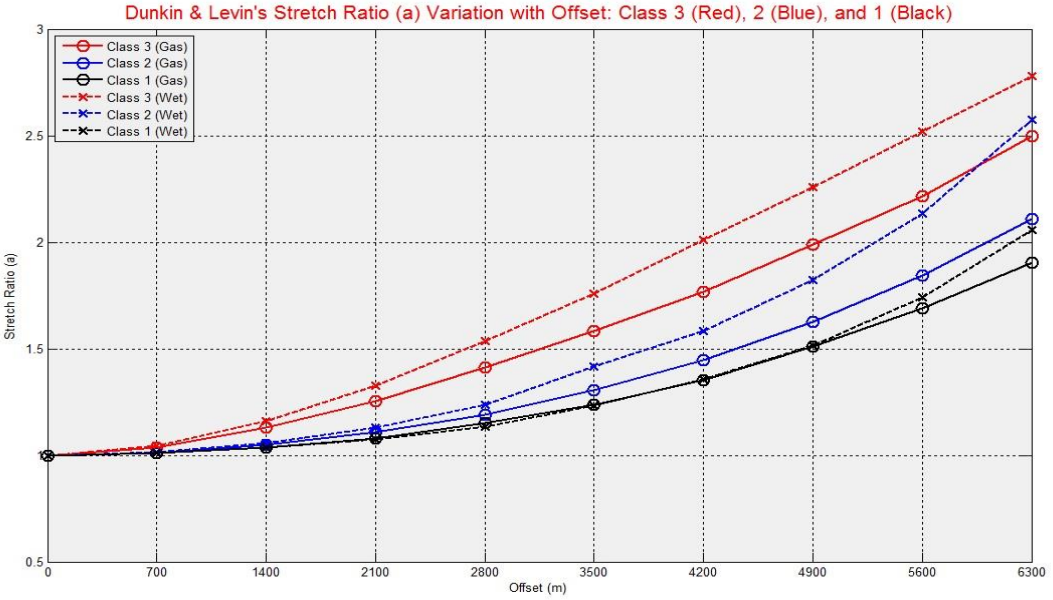

Fig. 2.41. Dunkin and Levin's Stretch-ratio variation with offset for corresponding top of Class 3 (red), 2 (blue), and 1 (black) for gas and brine-saturated models. Circle indicates gas-saturated case and x represents brine-saturate case.

and Levin's Stretch ratio, which is computed based on the curves in Figure 2.40, the separation could be observed more noticeably (Figure 2.41). By following the definition of Dunkin and Levin's Stretch-ratio (1973, Appendix B), the Stretch-ratio of a target purse could be computed in terms of the length of offset, target depth, and NMO-velocity of the target purse. Even though the two sand-beds are located at the same time depth and offset in the example of Class 3 sand layers, the Stretch-ratios for the gas-saturated layer and brine-saturated layer could be differentiated from each other due to the fact that the corresponding NMO velocities for both cases are different.

2.3 Conclusion of investigation

In the investigation of the first model, general tendencies of waveform changes arising from NMO-stretch were observed. From comparison of waveform changes based on the spectral analyses of before and after applying NMO-correction into the model, progressive reductions of bandwidth and shifts toward lower frequencies along with offset increase were detected. The computed Dunkin and Levin's Stretch-ratio for the first model successfully illustrated the general tendencies. In the investigation of the second model set, the possibility of the Dunkin and Levin's Stretch-ratio as a new seismic attribute for reservoir characterization was tested. With the Stretch-ratio, the degrees of NMO-stretch for gas-saturated case and the brine-saturated case concerning AVO Class 3, 2, and 1 were noticeably separated at the far offset on corresponding CMP gather. It indicates that gas and wet situations concerning typical AVO Classes could be discriminated by proper investigation of NMO-stretch at the far offset in pre-stack seismic data.

CHAPTER III

NMO-STRETCH CORRECTION

3.1 Description of the methodology: Wavelet deconvolution

In this chapter, the strategy of Castoro et al. (2001) is applied to the investigated models described above for correcting the NMO-stretch that occurred in the models. Castoro et al. proposed the wavelet deconvolution method in order to remove NMO-stretch and correct waveform changes. The procedures of the method are described as below:

1. Applying the NMO-correction,
2. Windowing and applying Fourier transform into the data,
3. Dividing the Fourier transform of each NMO-corrected segment by the Fourier transform of the corresponding isolated NMO-corrected wavelet,
4. Convolving the result with the wavelet and band-pass to provide a constant bandwidth output.

The above procedures can be expressed as

$$\mathrm{R(f)}W_1(f) = [\frac{\tilde{S}_x(f)}{\widetilde{W}(f)}]W_1(f), \qquad (1)$$

where $\tilde{S}_x(f)$ is the Fourier transform of each NMO corrected segment at offset x, $\widetilde{W}(f)$ is the Fourier transform of the corresponding isolated NMO-corrected wavelet, [ ] indicates windowing, and $W_1(f)$ is the Fourier transform of a wavelet with band-width narrower than w_t, which corresponds to wavelet on original uncorrected trace. The reason why they convolved $W_1(f)$ into reflectivity instead of convolving w_t is that irregular distribution of amplitudes in the

high frequency range of their spectrum that was seen in their model, when w_t was used as convolved wavelet. It was due to the fact that NMO-correction, they conducted, removed the frequency and it could not be retrieved by the convolution. In the corrections, which will be described in the following sections, the investigated wavelets, w_t, the original wavelets on uncorrected trace of the author's models in synthetic or real data set, are used instead of $W_1(f)$ in equation (1) for the correction of NMO-stretch. A detailed description of applying the wavelet deconvolution method is given in the following sections. To deconvolve stretched NMO-corrected wavelets from targeted NMO-corrected traces concerning procedure no. 3, described above, the Sacchi's sparse-deconvolution (1997) is used based on the sparse reflectivity assumption; a seismogram is composed of a finite superposition of seismic wavelets.

3.2 Correction of the first model

3.2.1 Application

The procedures of the wavelet deconvolution method are described in detail along with the first model. Firstly, the 11th trace, which is located at farthest offset, 3600 meter, on the synthetic CMP gather illustrated in Figures 2.4 and 2.5, is selected for showing the procedures. Figures 3.1 and 3.2 portray the targeted trace before and after applying NMO-correction. By comparing Figure 3.1 (before NMO-correction) and Figure 3.2 (after NMO-correction), the NMO-stretch that occurred is observed. It is also shown from comparison of the isolated wavelets on the traces, which are the wavelet extracted from uncorrected trace (Figure 3.3) and the wavelet extracted from NMO-corrected trace (Figure 3.4). After applying NMO-correction, the reflectivity shown in Figure 3.5 is generated by conducting sparse-deconvolution between the NMO-corrected trace and the isolated NMO-corrected wavelet.

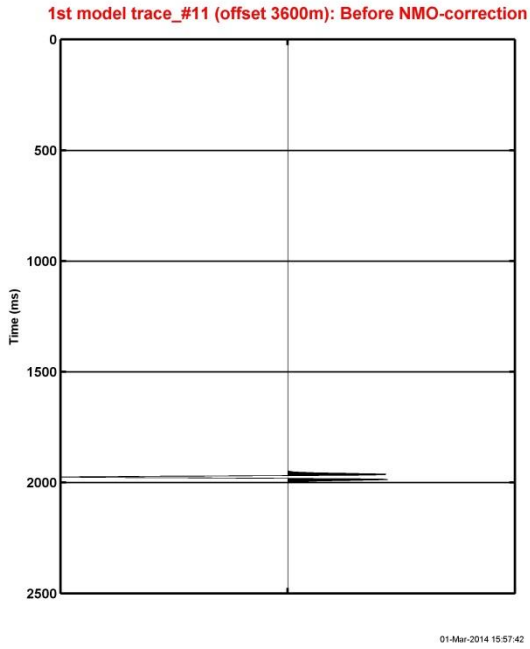

Fig. 3.1. The 11th trace at farthest offset, 3600 meter on the first model (Before NMO-correction).

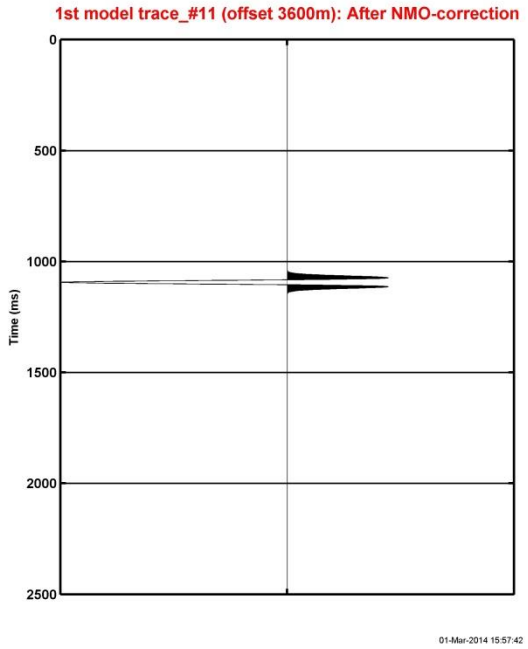

Fig. 3.2. The 11th trace at farthest offset, 3600 meter on the first model (After NMO-correction).

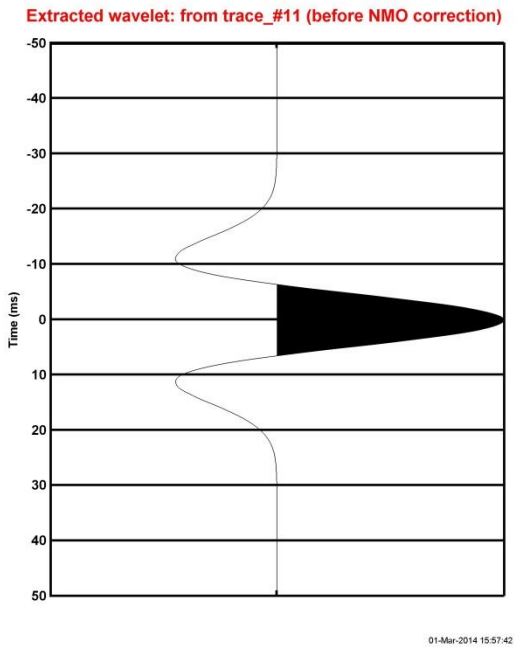

Fig. 3.3. An extracted wavelet from uncorrected trace in Figure 3.1.

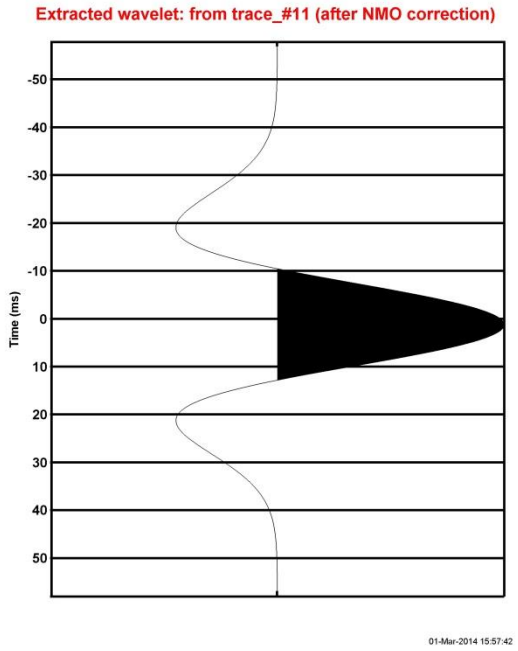

Fig. 3.4. An extracted wavelet from NMO-corrected trace in Figure 3.2.

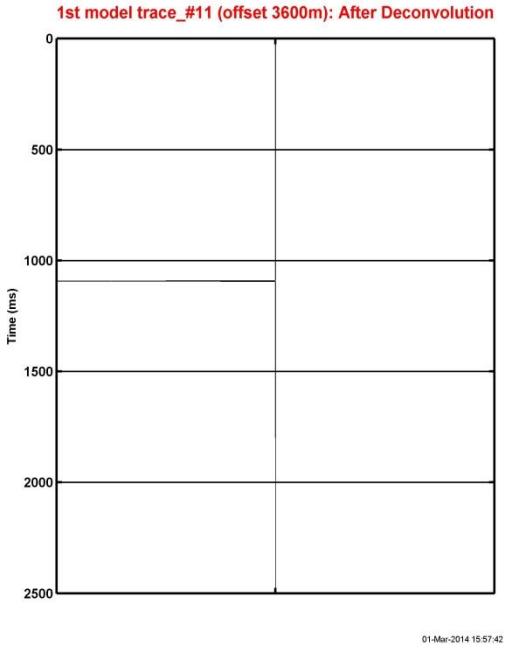

Fig. 3.5. The 11th trace at farthest offset, 3600 meter on the first model (After sparse-deconvolution).

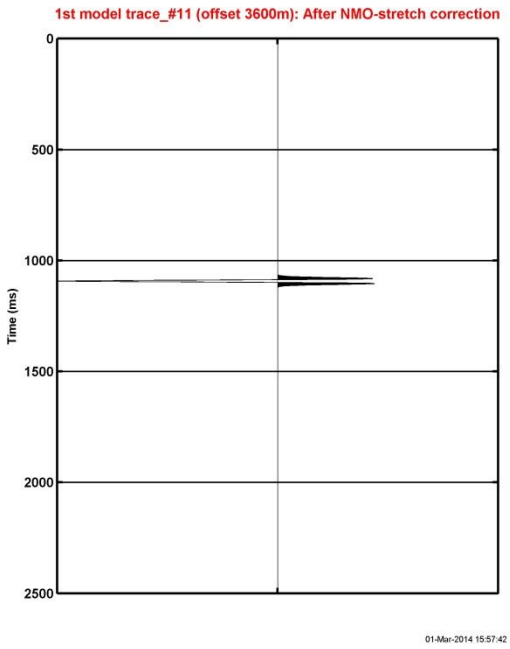

Fig. 3.6. The 11th trace at farthest offset, 3600 meter on the first model (After NMO-stretch correction).

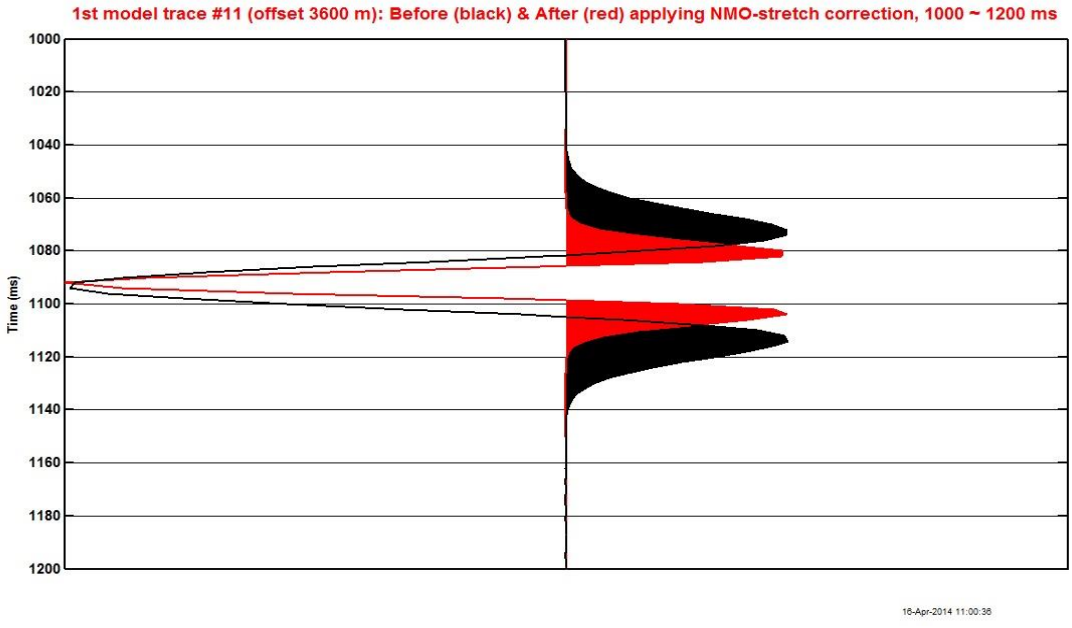

Fig. 3.7. The 11th trace at farthest offset, 3600 meter on the first model before (black-colored trace) and after (red-colored trace) applying NMO-stretch correction, 1000 ~ 1200 milliseconds.

By convolving the reflectivity and the original uncorrected wavelets, waveform changes on NMO-corrected trace are recovered almost perfectly. The final result of NMO-stretch correction for the 11th trace of the first model is presented in Figure 3.6. For better comparison, the targeted section of the trace before (black-colored trace) and after applying the NMO-stretch correction (red-colored trace) is magnified in time, 1000 ~ 1200 milliseconds (Figure 3.7). The application of the NMO-stretch correction is repeated on the whole CMP gather of the first model. The gathers before (Figure 3.8) and after conducting NMO-correction (Figure 3.9), shown in Figure 2.4 and 2.5, are presented again for describing procedures of the NMO-stretch correction. Figure 3.10 illustrates the result of implementing the sparse-deconvolution for the whole traces on the gather. The final result of NMO-stretch correction is described in Figure 3.11. Again, in order to observe the effectiveness of the correction, the targeted time section of CMP gather before (black-colored traces) and after applying the NMO-stretch correction (red-colored traces), 1000 ~ 1200 milliseconds, are selected for magnification (Figure 3.12).

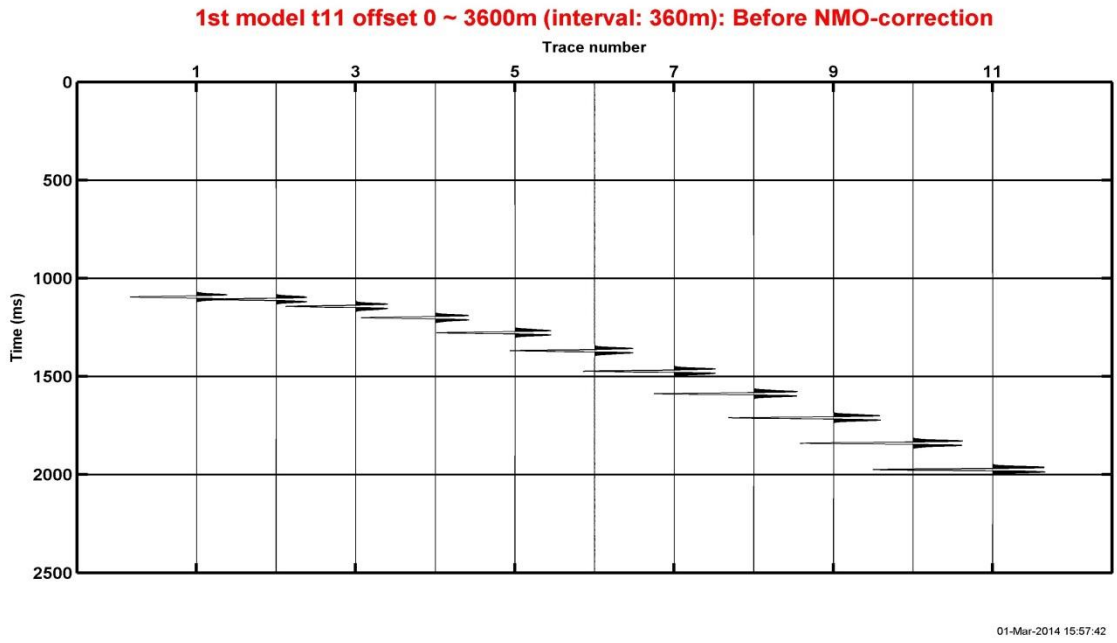

Fig. 3.8. Synthetic CMP gather of the first model (Before applying NMO-correction).

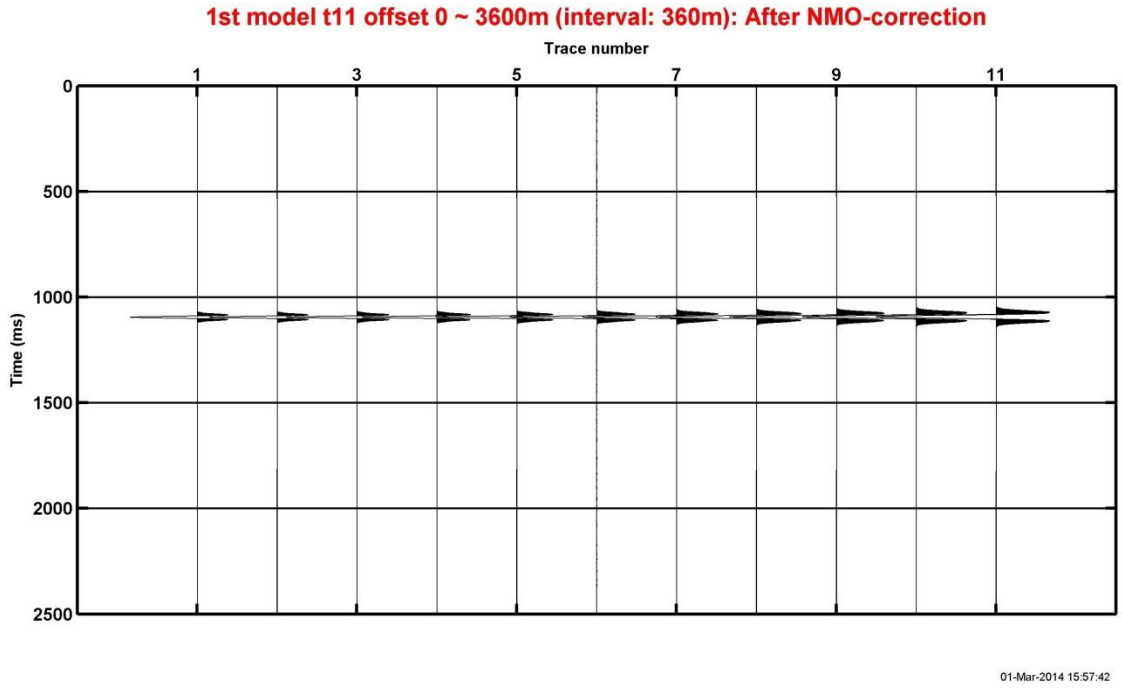

Fig. 3.9. Synthetic CMP gather of the first model (After applying NMO-correction).

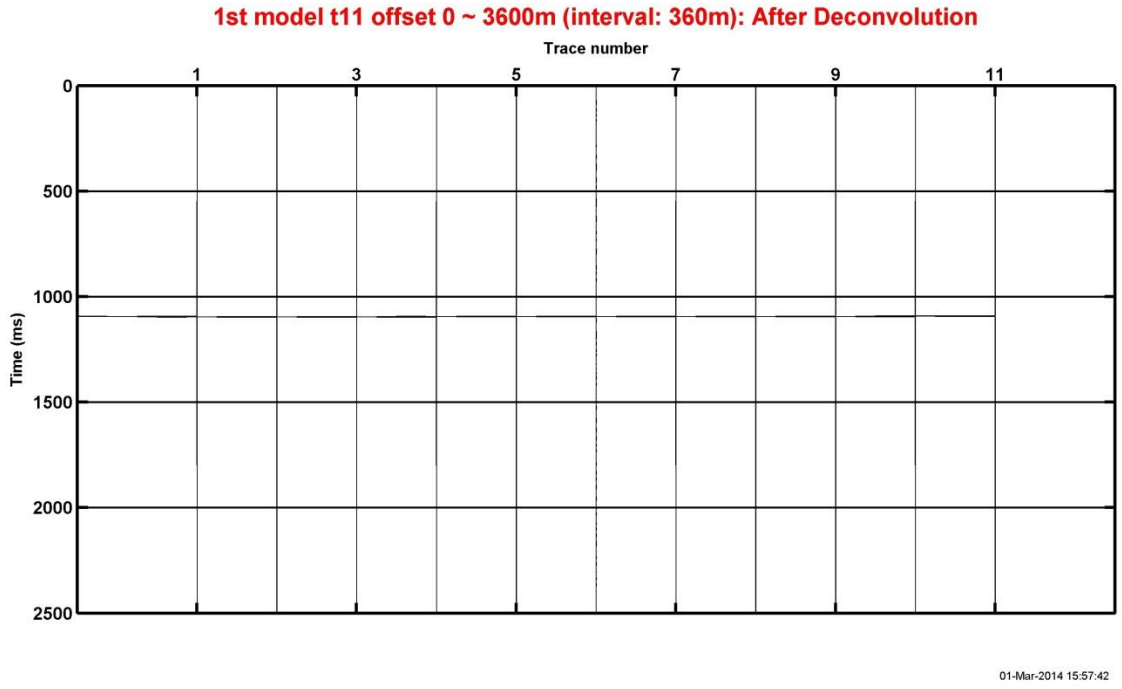

Fig. 3.10. Synthetic CMP gather of the first model (After applying sparse-deconvolution).

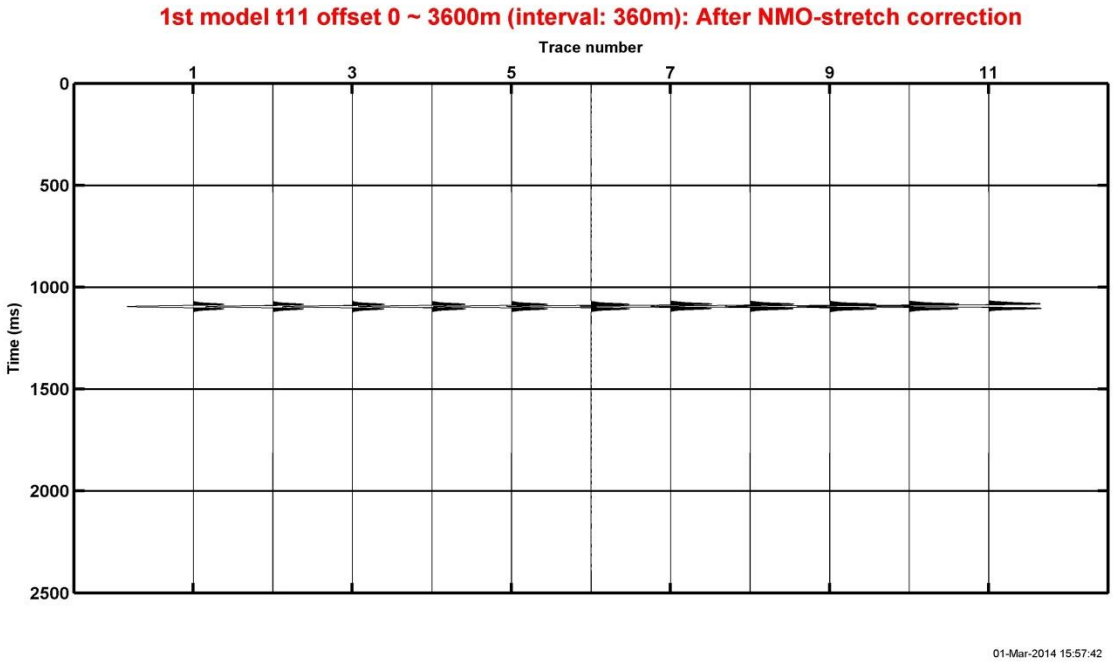

Fig. 3.11. Synthetic CMP gather of the first model (After applying NMO-stretch correction).

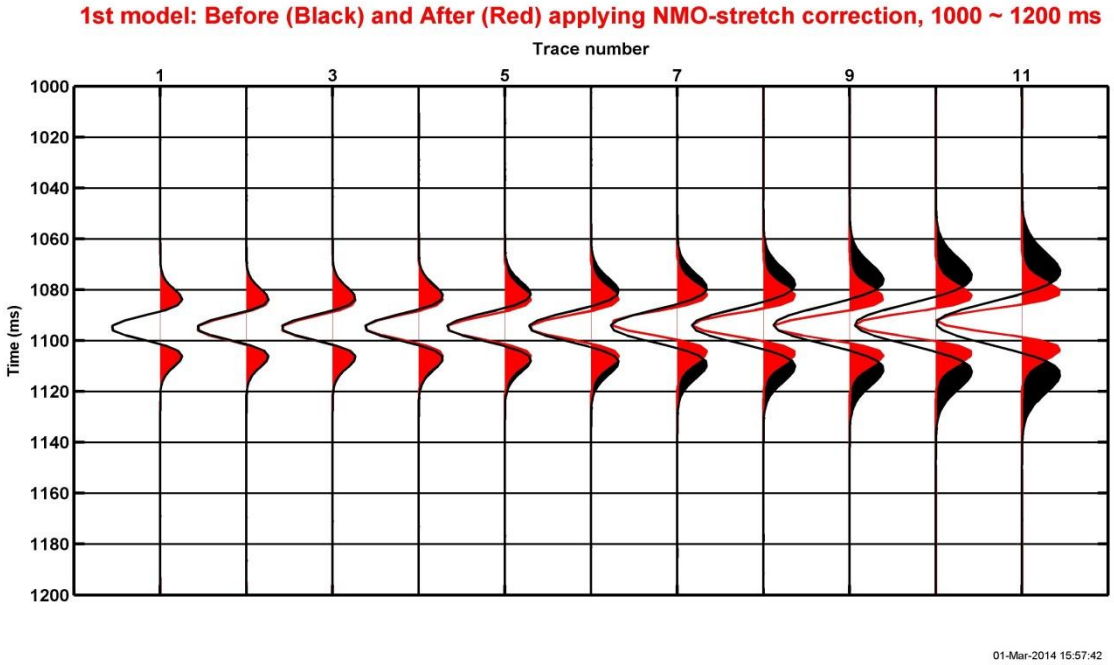

Fig. 3.12. Synthetic CMP gather of the first model, before (black-colored trace) and after applying NMO-stretch correction (red-colored trace), 1000 ~ 1200 milliseconds.

3.2.2 Verification

As shown in the investigation of the first model, the tendencies of wavelet distortions arising from NMO-stretch, which are progressive reduction of bandwidth and shifts toward lower frequencies along with offset increase, are detected. The distortions are shown by comparing the variable densities of amplitude spectra of CMP gather of the first model before (shown in Figure 2.17 and repeated in Figure 3.13) and after applying NMO-correction (shown in Figure 2.18 and repeated in Figure 3.14). To verify validation of the NMO-stretch correction, a new variable density of amplitude spectra after applying the correction is presented in Figure 3.15. The frequency information before NMO-correction (Figure 3.13) and after NMO-stretch correction (Figure 3.15) are almost identical. That is, the wavelet distortions are successfully recovered by the methodology. Further verifications of the effectiveness of the method, using spectral analyses in frequency domain and comparison in time domain for a selected trace, are also conducted. Figure 3.16 illustrates the amplitude spectra of both un-corrected (red) and NMO-corrected trace (blue) at the farthest offset (3600 meter) on CMP gather of the first model. The result of applying NMO-stretch correction into the trace is shown in Figure 3.17. The blue-colored spectrum indicates the spectrum of the trace after applying the NMO-stretch correction and the red-colored spectrum corresponds to the trace before the NMO-correction. Again, the frequency information of the un-corrected trace is almost perfectly recovered on the stretch-corrected trace. Comparison between the traces also shows the validation of the NMO-stretch correction. The corresponding targeted traces before and after applying the NMO-correction are illustrated in Figure 3.18. After applying the correction, the NMO-stretch is corrected (Figure 3.19). In order to observe details of wavelets and compare their differences, the wavelets are time-shifted in Figure 3.20. The observed severe waveform change is also corrected after applying the NMO-stretch correction (Figure 3.21). The NMO-corrected wavelet is overlapped with uncorrected wavelet. In addition,

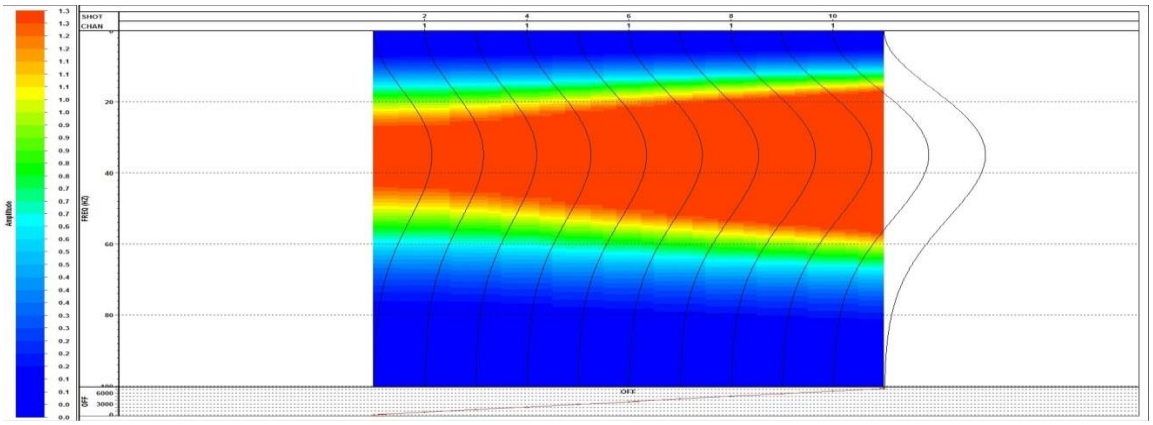

Fig. 3.13. Variable densities of amplitude spectra on CMP gather of the first model (Before NMO-correction).

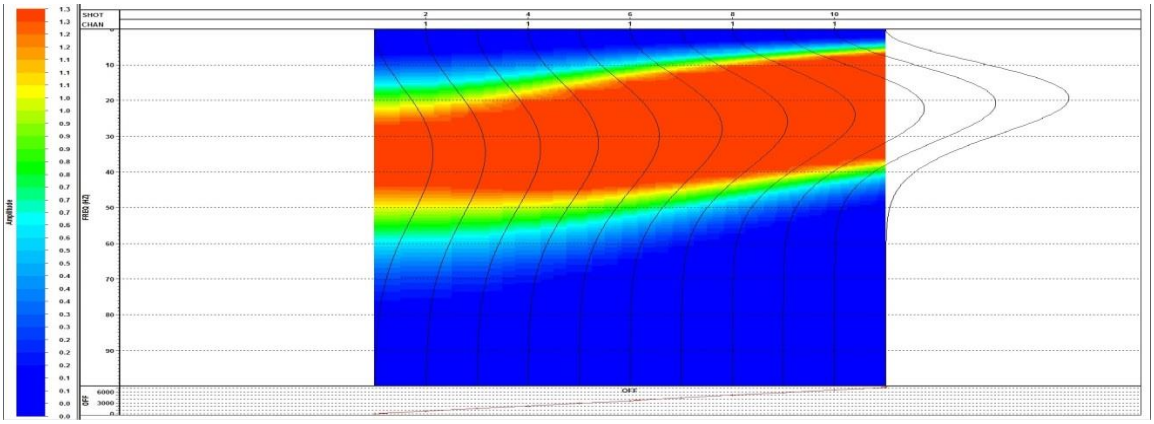

Fig. 3.14. Variable densities of amplitude spectra on CMP gather of the first model (After NMO-correction).

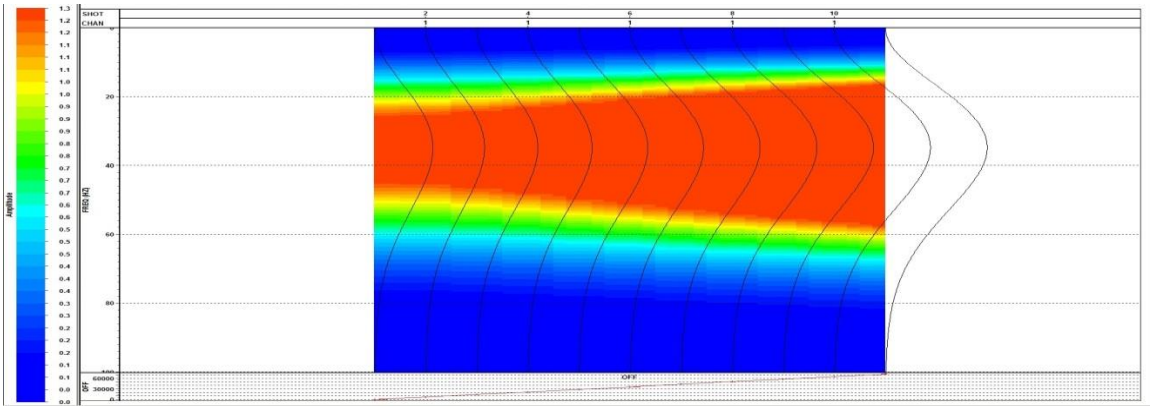

Fig. 3.15. Variable densities of amplitude spectra on CMP gather of the first model (After NMO-stretch correction).

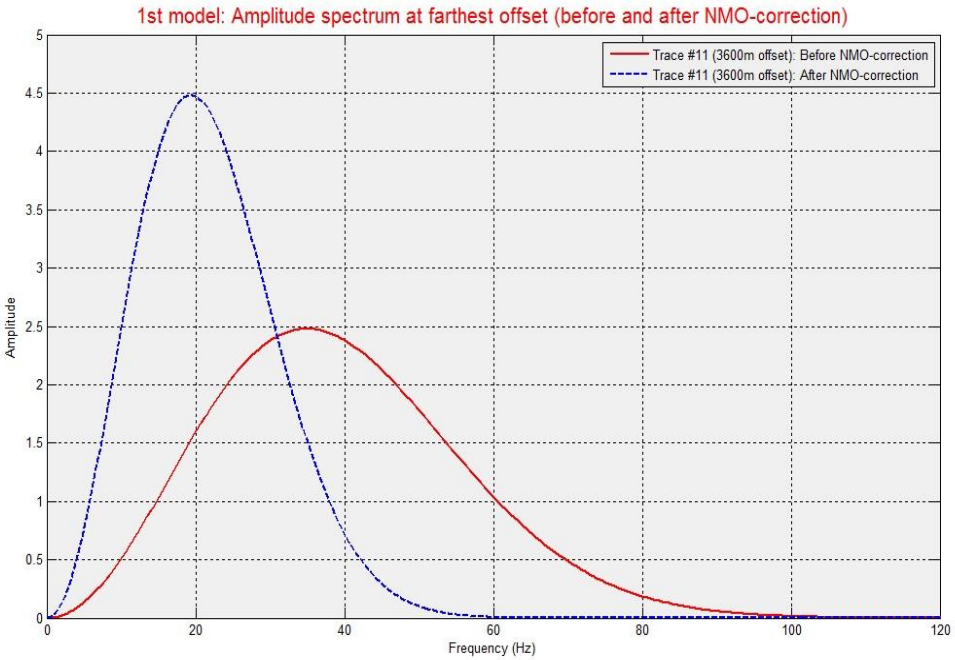

Fig. 3.16. Amplitude spectra of un-corrected (red) and NMO-corrected trace (blue) at the farthest offset, 3600 meter, of the first model (Before NMO-stretch correction).

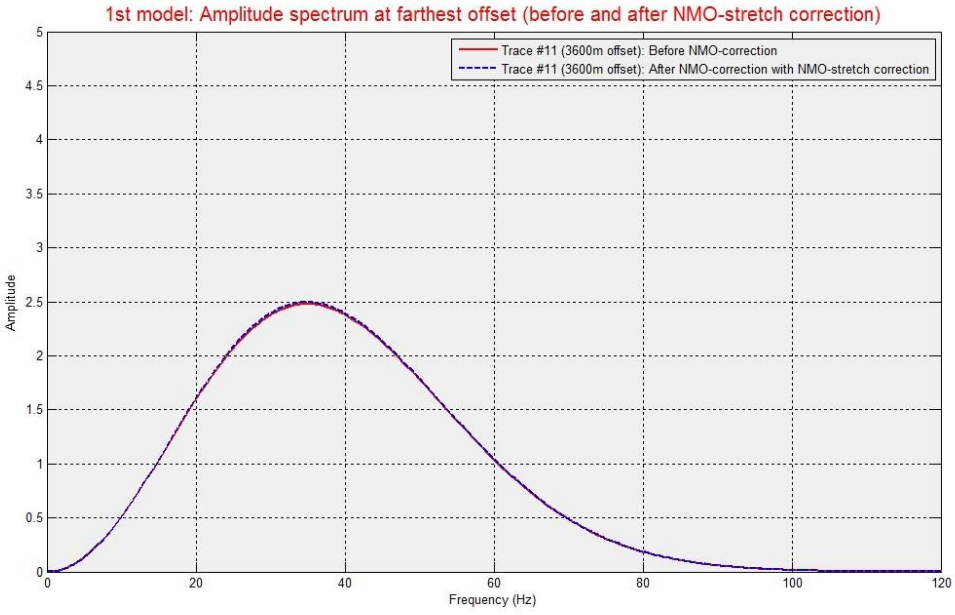

Fig. 3.17. Amplitude spectra of un-corrected (red) and NMO-corrected trace (blue) on the farthest offset, 3600 meter, of the first model (After NMO-stretch correction).

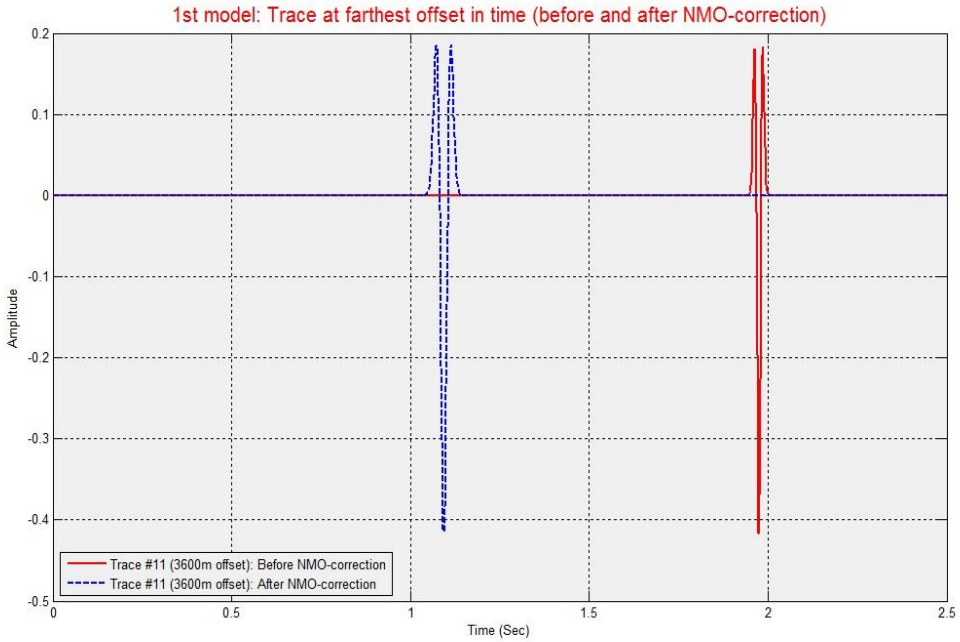

Fig. 3.18. Traces in time-domain before and after applying NMO-correction on the farthest offset, 3600 meter, of the first model (Before NMO-stretch correction).

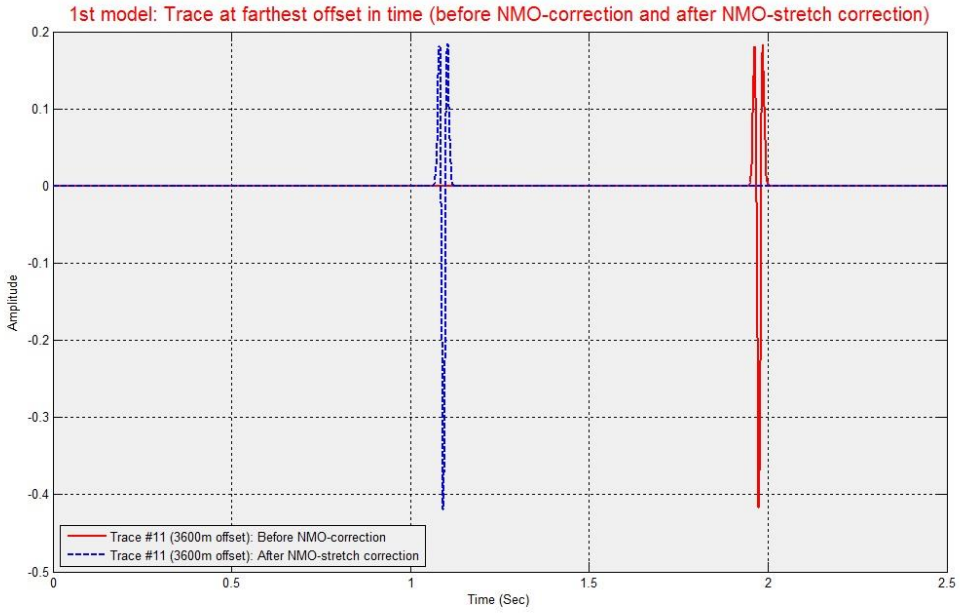

Fig. 3.19. Traces in time-domain before and after applying NMO-correction on the farthest offset, 3600 meter, of the first model (After NMO-stretch correction).

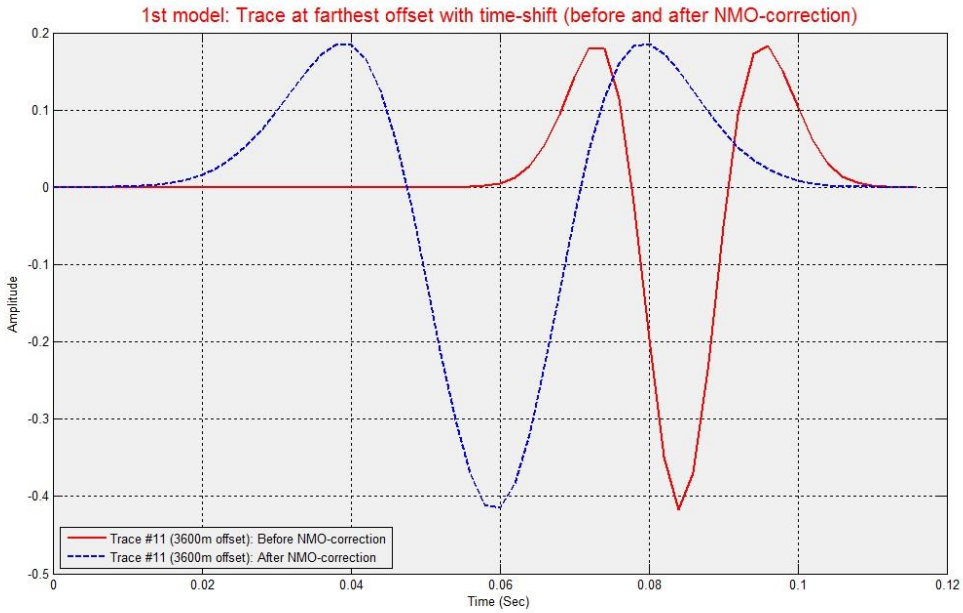

Fig. 3.20. Time-shift of traces described in Figure 3.17**.** Each end times of wavelets are used as the standard for the time-shift in the first model (Before NMO-stretch correction).

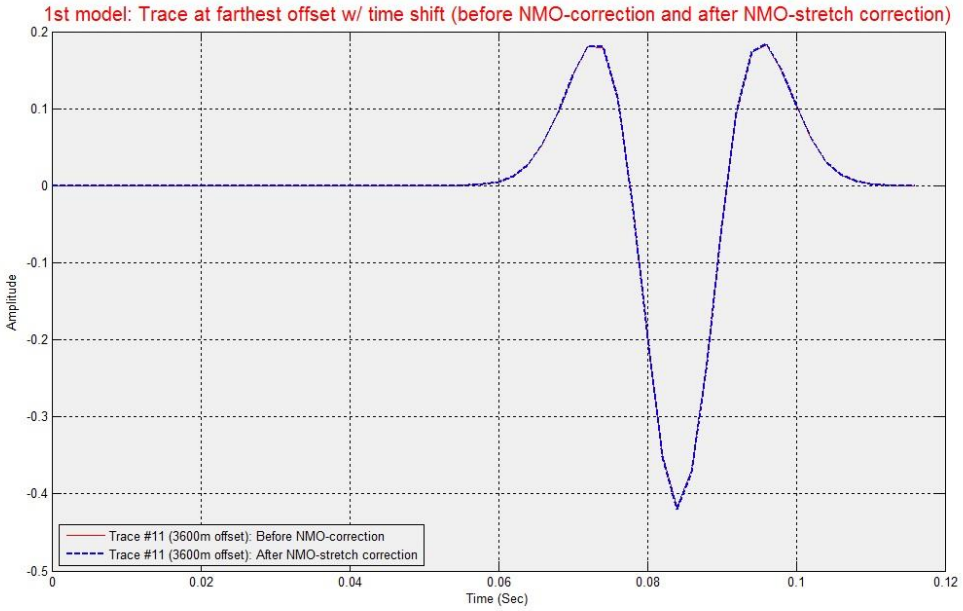

Fig. 3.21. Time-shift of traces described in Figure 3.18**.** Each end times of wavelets are used as the standard for the time-shift in the first model (After NMO-stretch correction).

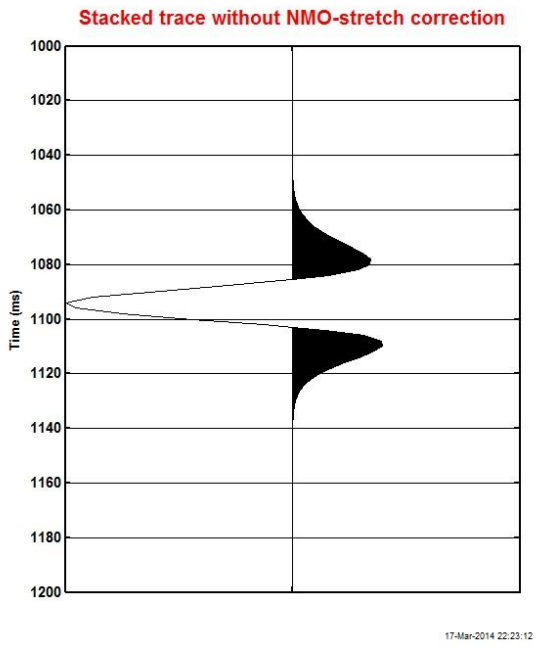

Fig. 3.22. Stacked trace of NMO-corrected CMP gather, 1st model, 1000 ~ 1200 ms (Without NMO-stretch correction).

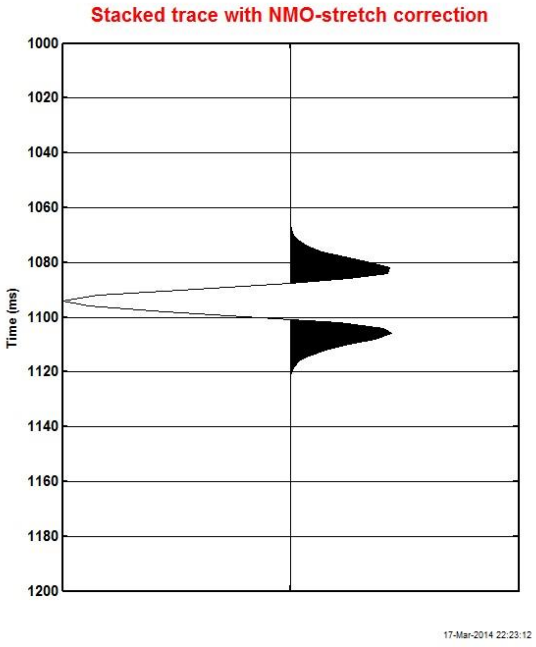

Fig. 3.23. Stacked trace of NMO-corrected CMP gather, 1st model, 1000 ~ 1200 ms (With NMO-stretch correction).

when the CMP gather of the first model is stacked with the NMO-stretch correction, the result of stacking, shown in Figure 3.23, has better resolution compared to when the stacked trace is achieved without the correction, described in Figure 3.22. The time section, 1000 ~ 1200 milliseconds, is selected for magnification of both traces. It illustrates that the NMO-stretch correction could provide the opportunity to generate post-stack data with better resolution for seismic imaging. The Figure 3.16, which was already described in Figure 2.22, is repeated for better presentation. Figures 3.18, 3.20, and 3.22 are also repeated, and are the same as Figures 2.23, 2.24, and 2.14. Spectral analyses and comparisons conducted above verify the validation of NMO-stretch correction.

3.3 Correction of the second model

3.3.1 Application

Corrections for the second model set are also conducted with the wavelet deconvolution method. Figure 3.24 depicts the NMO-corrected CMP gather of the gas-saturated model described in Figure 2.31. The 10th trace located at 6300 meter offset on the gather is selected for applying the correction for the purpose of observing the result of correction. Generally, NMO-stretch arise severely at the far-offset, however, the farthest trace on the gather, the 11th trace, has a post-critical event at 3600 milliseconds. Due to this fact, the 10th trace, the red colored trace in Figure 3.24, is chosen. By following the procedures of NMO-stretch correction described in the section 3.1, the selected trace is corrected. The trace before applying NMO-correction is shown in Figure 3.25. After NMO-correction, wavelets on the trace are stretched (Figure 3.26). However, after applying the sparse-deconvolution, the stretched wavelets are deconvolved to a decent level (Figure 3.27), and then the distorted waveforms are corrected by convolving the investigated wavelets on the trace before applying NMO-correction and the deconvolved result (Figure 3.28). Figure 3.29 shows a comparison before (black-colored trace) and after (red-colored trace) applying the NMO-stretch correction into the targeted trace. In order to observe details of the result, a time section of the trace, 2400 ~ 2800 milliseconds, is magnified in Figure 3.30.

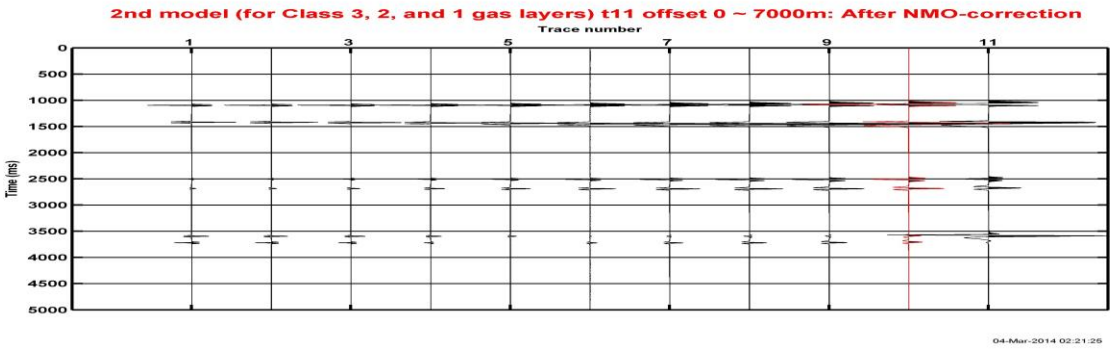

Fig. 3.24. NMO-corrected synthetic CMP gather of the gas-saturated model in the second model set. The 10th trace (red-colored trace), located at 6300 meter offset on the gather, is selected for applying the correction.

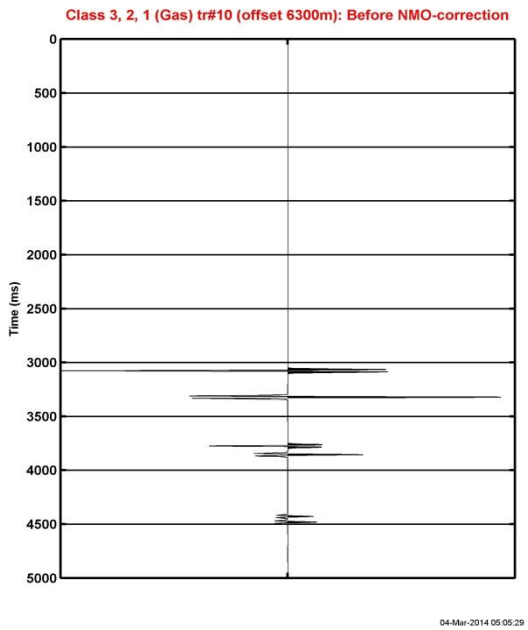

Fig. 3.25. The 10th trace, located at 6300 meter offset on the gas-saturated model in the second model set (Before NMO-correction).

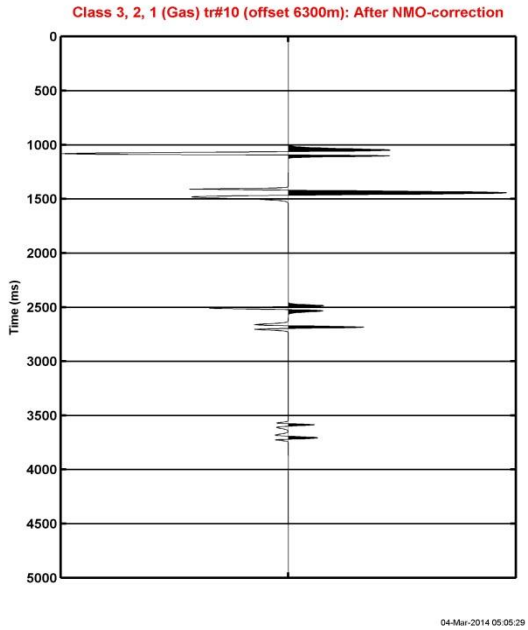

Fig. 3.26. The 10th trace, located at 6300 meter offset on the gas-saturated model in the second model set (After NMO-correction).

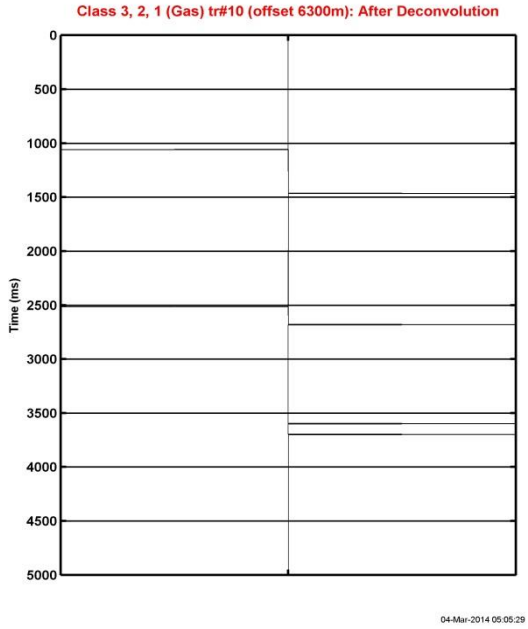

Fig. 3.27. The 10th trace, located at 6300 meter offset on the gas-saturated model in the second model set (After sparse-deconvolution).

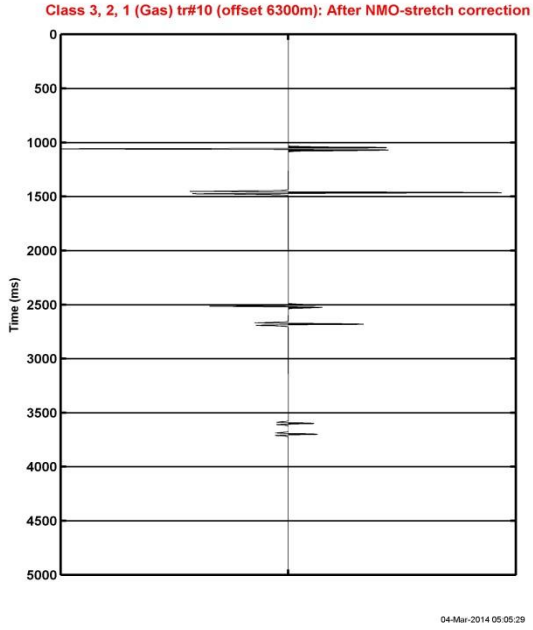

Fig. 3.28. The 10th trace, located at 6300 meter offset on the gas-saturated model in the second model set (After NMO-stretch correction).

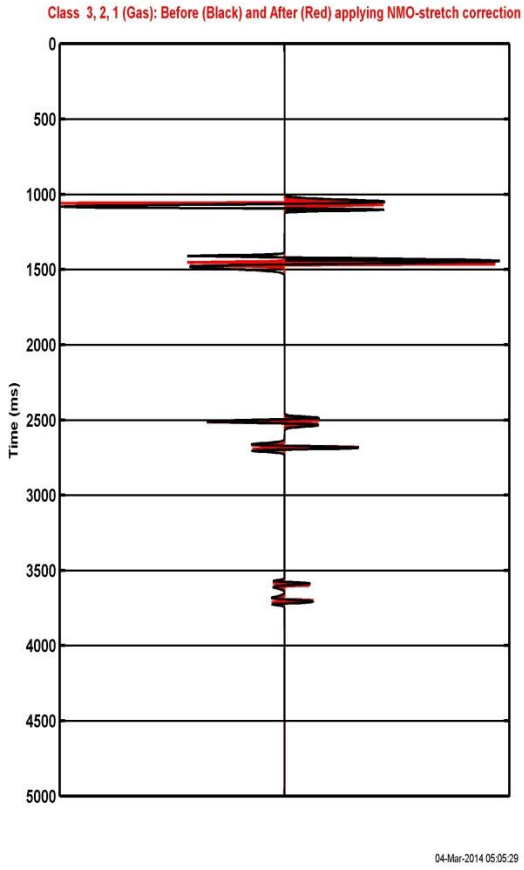

Fig. 3.29. The 10th trace, located at 6300 meter offset on the gas-saturated model in the second model set before (black-colored trace) and after (red-colored trace) applying NMO-stretch correction.

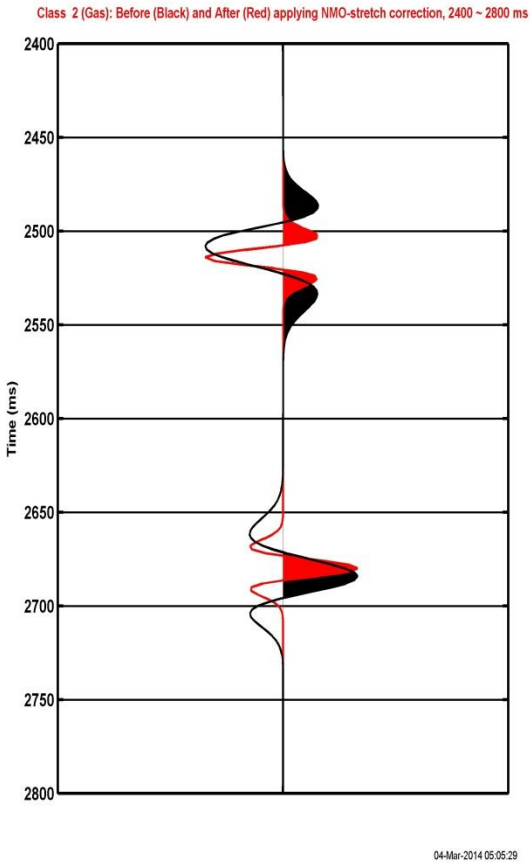

Fig. 3.30. The 10th trace, located at 6300 meter offset on the gas-saturated model in the second model set before (black-colored trace) and after (red- colored trace) applying NMO-stretch correction, 2400 ~ 2800 ms.

The NMO-stretch correction for the brine-saturated model is also applied. The NMO-corrected CMP gather of the brine-saturated case is illustrated in Figure 3.31. For the model, the 10th trace of the model is selected again for the same reason described above. It is depicted in red color. The traces before (black-colored trace) and after (red-colored trace) applying NMO-stretch correction are illustrated in Figure 3.32 to show the result of the correction. Its selected time section, 900 ~ 1500 milliseconds, is also presented in Figure 3.33 for better comparison of the two.

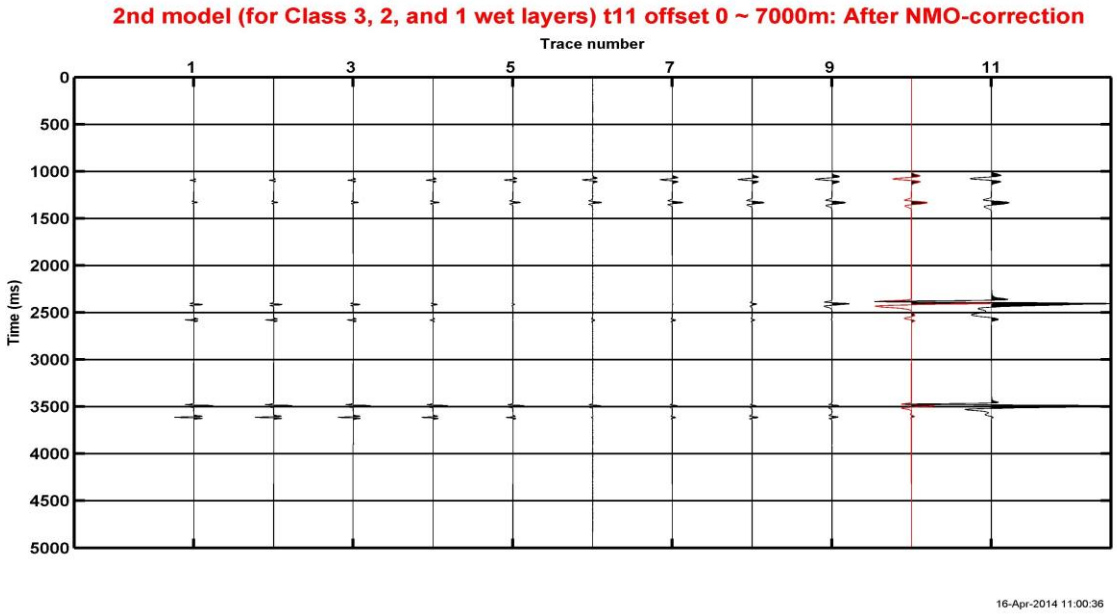

Fig. 3.31. NMO-corrected synthetic CMP gather of the brine-saturated model in the second model set. The 10th trace (red-colored trace), located at 6300 meter offset on the gather, is selected for applying the correction.

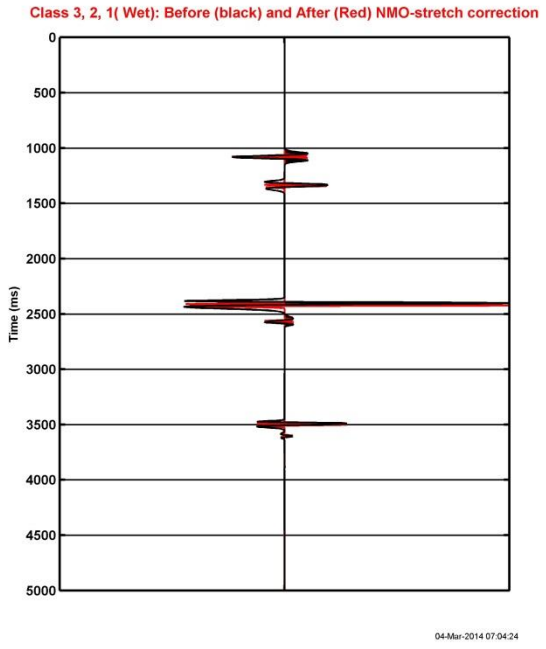

Fig. 3.32. The 10th trace, located at 6300 meter offset on the brine-saturated model in the second model set before (black-colored trace) and after (red-colored trace) applying NMO-stretch correction.

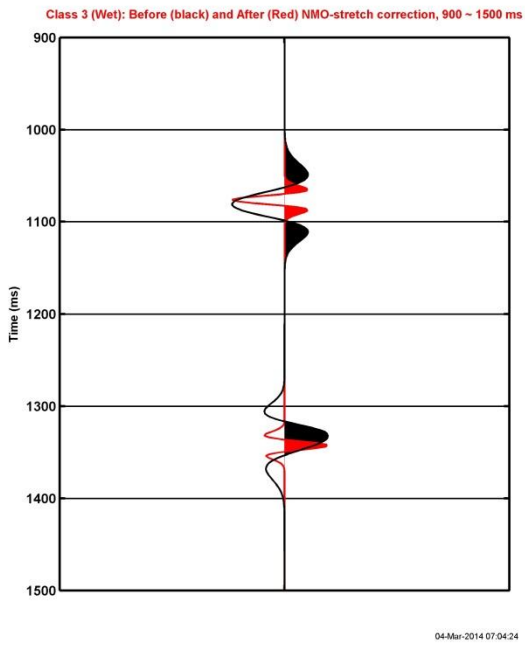

Fig. 3.33. The 10th trace, located at 6300 meter offset on the brine-saturated model in the second model set before (black-colored trace) and after (red- colored trace) applying NMO-stretch correction, 900 ~ 1500 ms.

3.3.2 Verification

For the aim of verifying the validation of the NMO-stretch correction and conduct a detailed frequency analysis for the second model set, time-frequency analyses including Short Time Window Fourier Transform (STFT, Bracewell, 1986, Cohen, 1994, Partyka et al., 1999), Continuous Wavelet Transform (CWT, Alam and Taylor, 2006, Matos and Marfurt, 2008) and Constrained Least Squares Spectral Analysis (CLSSA, Puryear et al., 2012) are implemented. The STFT is the crosscorrelation of the seismic trace with a sinusoidal basis over a moving time window, and the CWT is another crosscorrelation of the seismic trace against adjusted mother wavelet. However, the CLSSA is an inversion-based spectral decomposition method to time-frequency analysis of a seismic trace by applying constrained least-squares spectral analysis (Puryear et al., 2012). By executing the spectral decomposition methods listed above, 1-D targeted traces (the 10^{th} traces on CMP gathers of gas-saturated and brine-saturated models in the second model set) could be transformed to 2-D time-frequency panels. The results of applying STFT into the targeted traces, before and after applying NMO-correction and after applying NMO-stretch correction, are illustrated in Figure 3.34 (for the gas-saturated model) and 3.36 (for the brine-saturated model) to verify effectiveness of the NMO-stretch correction for the models. To generate the time-frequency panels, a 300 milliseconds time window, which is three times of the length of designed wavelet, 100 milliseconds, is applied for both models. In Figures 3.34 and 3.36, the traces and their STFT results before NMO-correction are depicted on the left side of both figures, and the traces and their STFT time-frequency representations after applying NMO-correction and NMO-stretch correction are also described in the middle (for NMO-corrected traces) and on the right (for NMO-stretch corrected traces) side of Figures 3.34 and 3.36. In both results, we could observe that distorted low frequencies after NMO-correction are corrected and frequency information before applying NMO-correction is recovered in the traces after applying

NMO-stretch correction. The STFT panels of uncorrected traces (left, Figures 3.34 and 3.36) indicate the dominant frequencies of wavelets on the traces are 35Hz. It is identical to the dominant frequency of designed Ricker wavelet described in Figure 2.2. After conducting the NMO-corrections, the NMO-stretch increases more severely, along with decrease in time depth on the NMO-corrected traces, for both the gas-saturated (middle, Figure 3.34) and brine-saturated models (middle, Figure 3.36). However, after applying NMO-stretch correction, the distorted dominant frequencies move to the correct position, 35Hz (right, Figure 3.34 and 3.36). Since CWT was devised to overcome the resolution problem of STFT (Alam and Taylor., 2006, Matos and Marfurt, 2008) and CLSSA showed better resolution than STFT and CWT (Puryear et al., 2012, Arnold and Castagna, 2013), other results applying CWT and CLSSA for selected segments of the targeted traces in the second model set are also described in Figure 3.35 and 3.37 to compare more details. For the gas-saturated model, a time section, 2950 ~ 3200 milliseconds, is selected for the uncorrected trace (top, Figure 3.35 (a)), and a corresponding time section, 950 ~ 1200 milliseconds, is chosen for the trace after NMO-correction (middle, Figure 3.35 (b)) and the trace after NMO-stretch correction (bottom, Figure 3.35 (c)). For the brine-saturated model, a time section, 3000 ~ 3150 milliseconds, is selected for the uncorrected trace (top, Figure 3.37 (a)), and a corresponding time section, 1000 ~ 1150 milliseconds, is chosen for the trace after NMO-correction (middle, Figure 3.37 (b)) and the trace after NMO-stretch correction (bottom, Figure 3.37 (c)). The specific time locations of selected time sections are expressed in red arrows in Figures 3.34 and 3.36. These results also verify the validation of the wavelet deconvolution method to correct NMO-stretch. After applying the NMO-stretch correction, the 35Hz dominant frequency of uncorrected wavelets are almost perfectly recovered on NMO-corrected traces (Figure 3.35 (c) and 3.37 (c)). Additionally, since the same 300 milliseconds time window is applied in order to generate three different time-frequency panels, such as STFT, CWT, and CLSSA for traces before and after applying NMO-correction, we could compare the ability of

each spectral decomposition methods to resolve adjacent events in time. Although interferences occur in the panels of selected wavelet on uncorrected trace (Figure 3.37 (a)) due to the energy from contiguous events of targeted section, CWT and CLSSA show better resolution for time-frequency representation than STFT. CLSSA has the best ability to resolve events. Even though the frequency information are almost identical to the information of the uncorrected trace, the reason why there are no interferences in the panels described in Figure 3.37 (c), which corresponds to NMO-corrected traces after NMO-stretch correction, is that adjacent events are separated from the targeted wavelet with enough distance beyond the set window length of 300 milliseconds.

3.4 Correction of Dunkin and Levin's model

3.4.1 Model description and application

In this thesis, Dunkin and Levin's model (1973) is used to confirm the effectiveness of NMO-stretch correction for better understanding of more realistic situation. In Dunkin and Levin, the model was used to describe the amount of waveform distortions, NMO-stretch, with offset and depth changes. We will observe the degree of NMO-stretch in the following descriptions in this chapter. The P-wave profile of the model is described in Table 3.1. Additional density and S-wave velocity profiles of Dunkin and Levin's model are newly computed by Gardner's empirical relation (Gardner et al., 1974) and Greenberg-Castagna's V_P - V_S relations (Greenberg and Castagna, 1992) for the generation of the synthetic CMP gather of this model. The set of synthetic well-logs, corresponding to density, P-wave, and S-wave velocity profiles, is illustrated in Figure 3.38. Both P-wave and S-wave velocity values (ft/s) are converted to slowness ($\mu s/m$) to follow the LAS format. Unit of depth is also converted from feet to meters. The Ricker wavelet

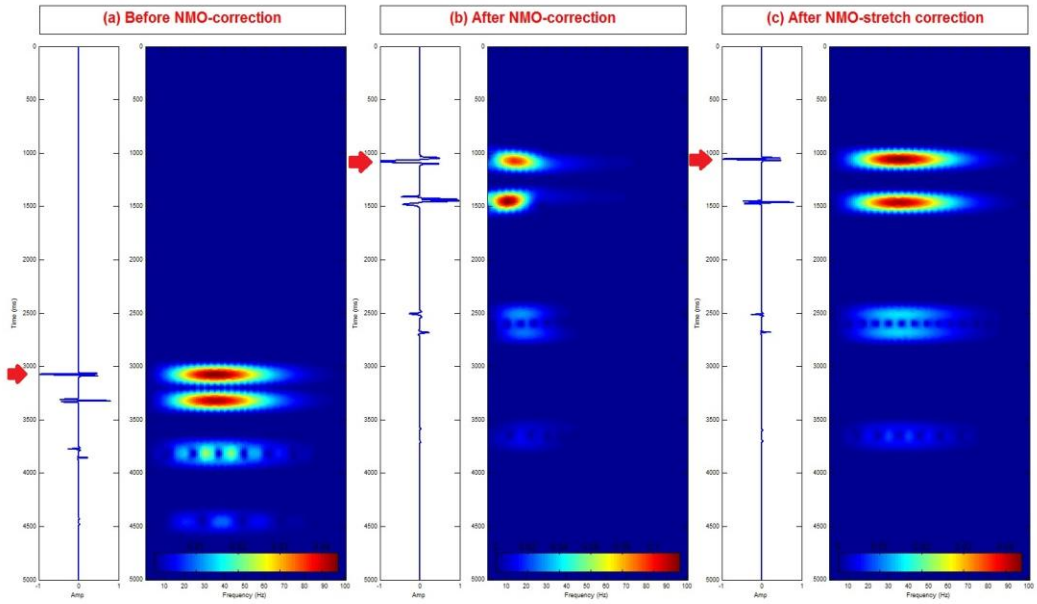

Fig. 3.34. The 10th trace of the gas-saturated model and its time-frequency panel applying STFT. (a) Before NMO-correction, (b) After NMO-correction and (c) After NMO-stretch correction. Red arrows indicate targeted wavelets which are described in Figure 3.35.

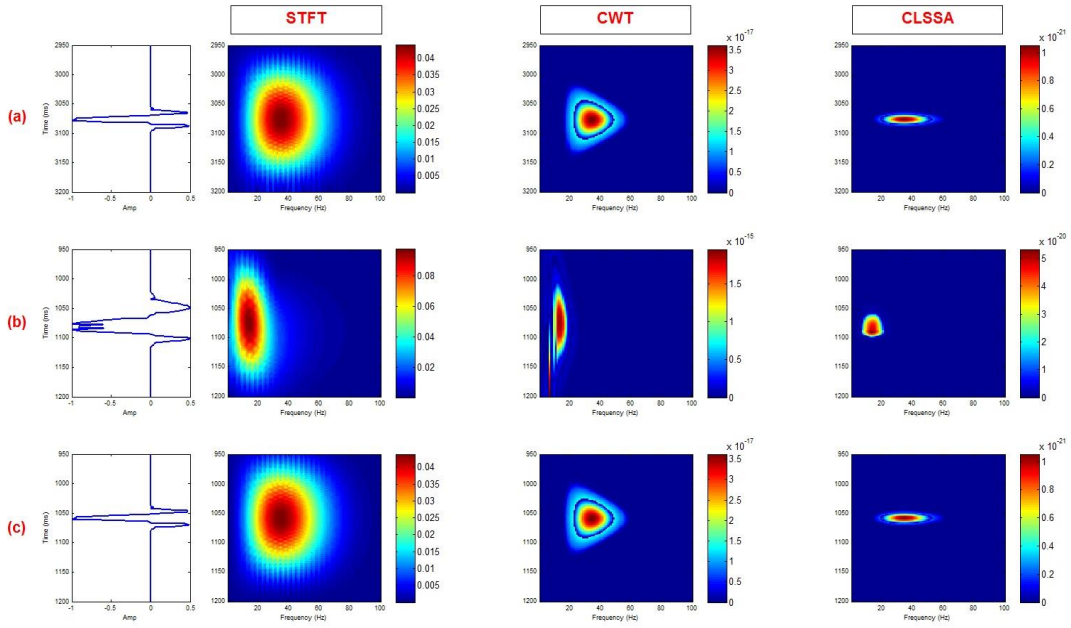

Fig. 3.35. Selected segments on the 10th trace of the gas-saturated model and their time-frequency panels applying STFT (left), CWT (middle), and CLSSA (right). (a) Before NMO-correction, 2950 ~ 3200 milliseconds of the trace shown in Figure 3.34 (a), (b) After NMO-correction, 950 ~ 1200 milliseconds of the trace shown in Figure 3.34 (b), (c) After NMO-stretch correction, 950 ~ 1200 milliseconds of the trace shown in Figure 3.34 (c).

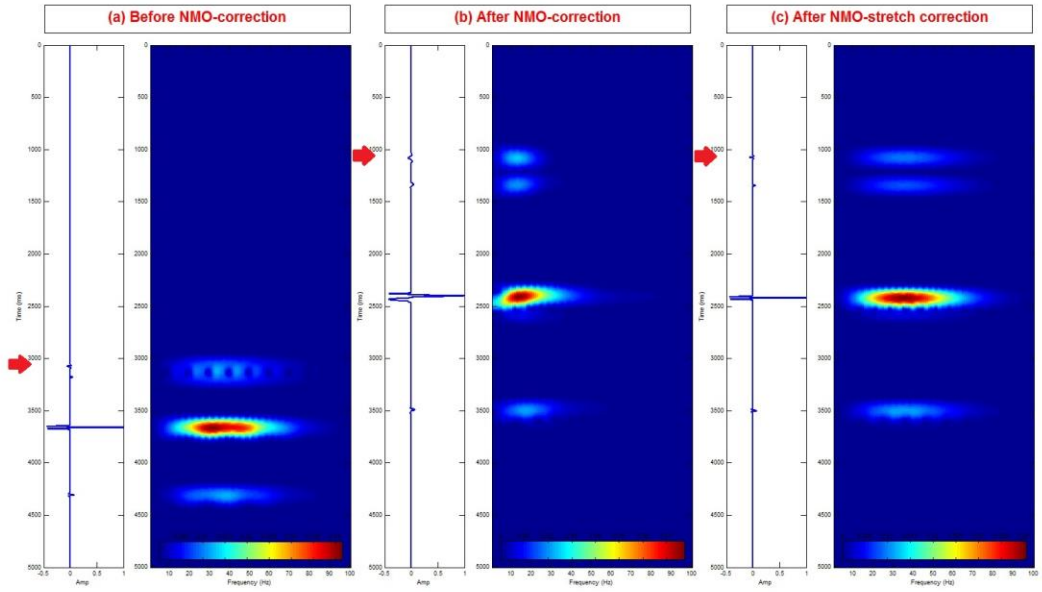

Fig. 3.36. The 10th trace of the brine-saturated model and its time-frequency panel applying STFT. (a) Before NMO-correction, (b) After NMO-correction and (c) After NMO-stretch correction. Red arrows indicate targeted wavelets which are described in Figure 3.37.

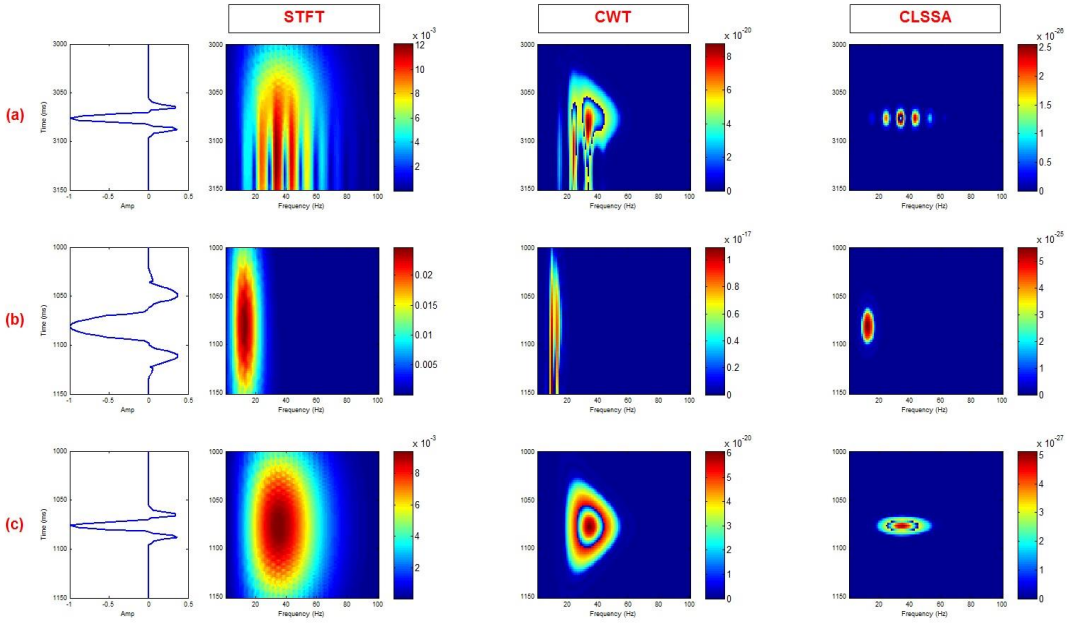

Fig. 3.37. Selected segments on the 10th trace of the brine-saturated model and their time-frequency panels applying STFT (left), CWT (middle), and CLSSA (right). (a) Before NMO-correction, 3000 ~ 3150 milliseconds of the trace shown in Figure 3.36 (a), (b) After NMO-correction, 1000 ~ 1150 milliseconds of the trace shown in Figure 3.36 (b), (c) After NMO-stretch correction, 1000 ~ 1150 milliseconds of the trace shown in Figure 3.36 (c).

described in Figure 2.2, which was used for the first and second models in this thesis, is used again for generating synthetic CMP gather. It was also used in Dunkin and Levin (1973). The wavelet has a 35Hz dominant frequency and 100 milliseconds wavelet length. On track 4, track 5, and at the rightmost track in Figure 3.39, the profiles of Poisson's ratio of Dunkin and Levin's model and corresponding reflectivity series, zero-offset synthetic seismogram, and the designed Ricker wavelet (35Hz dominant frequency, 100ms length) are newly generated from depth, P-wave, and S-wave velocity information. The synthetic CMP gather of the model is generated by applying the Zoeppritz equations with described rock parameters (Figure 3.40). Below are specific parameters for the synthetic CMP modeling of Dunkin and Levin's model:

- Target zone: 0 ~ 6100 (m)
- Geometric spreading, transmission losses, array effects and muting of post-critical events are not applied.
- Number of offset: 11
- Offset range: 0 ~ 3000 (m), Trace interval: 300 (m)
- Model blocking: travel-time (slowness) average
- Time window to model: 0 ~ 4000 (ms)
- Processing sample rate: 1 (ms)
- Output domain: time
- Output sample rate: 2 (ms)

Table 3.1. P-wave velocity profile for Dunkin and Levin's model (1973).

Depth profile (ft)	P-wave velocity (ft/sec)
0 ~ 600	7000
600 ~ 1600	7500
1600 ~ 3100	8000
3100 ~ 4000	9000
4000 ~ 4850	8500
4850 ~ 6350	10000
6350 ~ 7450	11000
7450 ~ 8500	10500
8500 ~ 9700	12000
9700 ~ 10250	11000
10250 ~ 11750	15000
11750 ~ 12650	18000
12650 ~ 14150	15000
14150 ~ 15850	17000
15850 ~ 17650	18000
17650 ~ 20000	20000

There are two reasons for setting the offset length as 3000 meter. Firstly, Dunkin and Levin (1973) set the largest source-receiver separation, offset, 9600 feet, which corresponds to 3000 meter approximately. The second reason is that beyond 3000 meter, severe post-critical events

occur both in relatively shallow depth and in almost whole depth of the model. Although the offset is set to be quite short in distance, 3000 meter, the post-critical events for first three reflections in shallow depth range could be observed in the synthetic CMP gather (Figure 3.40). The events are muted in Figure 3.41. After muting post-critical events on the CMP gather, NMO-correction is implemented with elaborate velocity analysis (Figure 3.42). A red-colored trace in Figure 3.42, the 11^{th} trace located at farthest offset (3000 meter) on the gather, is selected for applying the NMO-stretch correction to observe the result of applying the correction. The NMO-corrected trace is depicted in Figure 3.44. From the comparison between the traces before (Figure 3.43) and after (Figure 3.44) applying NMO-correction, the typical tendencies of NMO-stretch is more clearly observed; waveform distortions arise more severely in shallow time depths and the amount of the distortions decrease with increase in time depth. Figures 3.45 and 3.46 describe the procedures of NMO-stretch correction again. The trace applying sparse-deconvolution is shown in Figure 3.45 and final result of NMO-stretch correction is illustrated in Figure 3.46. Figure 3.47 provides a direct comparison of before (black-colored trace) and after (red-colored trace) applying NMO-stretch correction into the selected NMO-corrected trace. To look into the details of the results, a time section of the trace, 1400 ~ 1800 milliseconds, is magnified in Figure 3.48. Again, the waveform distortions are corrected with the correction.

3.4.2 Verification

For Dunkin and Levin's model, the time-frequency representations applying STFT, CWT, and CLSSA are computed in Figure 3.49 and 3.50 to verify validation the NMO-stretch correction. Specifically, 300 milliseconds are set as a time window to generate these time-frequency panels of STFT along with results applying CWT and CLSSA. It is three times the length of the designed Ricker wavelet, 100 milliseconds. Figure 3.49 shows the results of applying STFT into

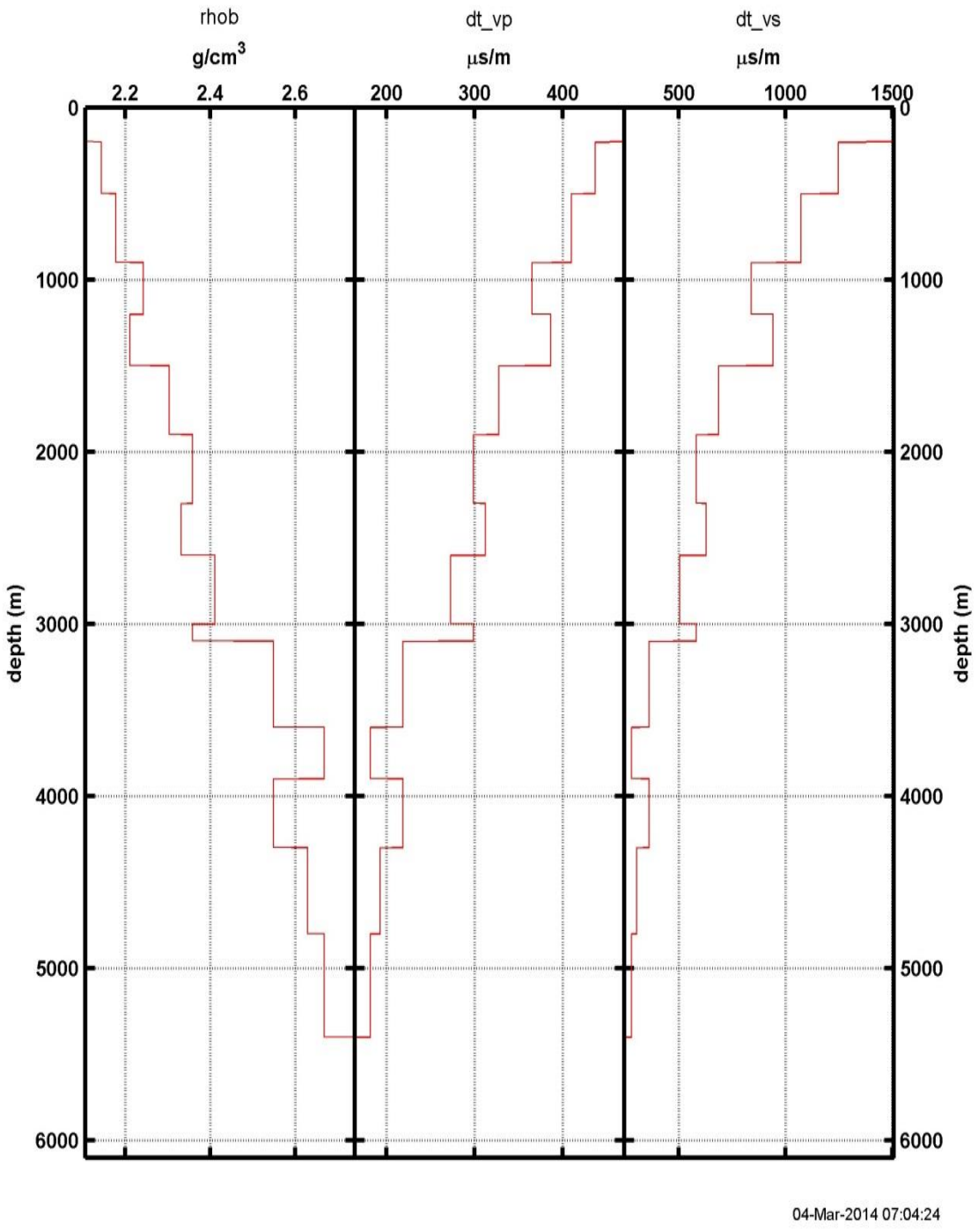

Fig. 3.38. Synthetic well-logs of density, P-wave, and S-wave slowness profiles for Dunkin and Levin's model.

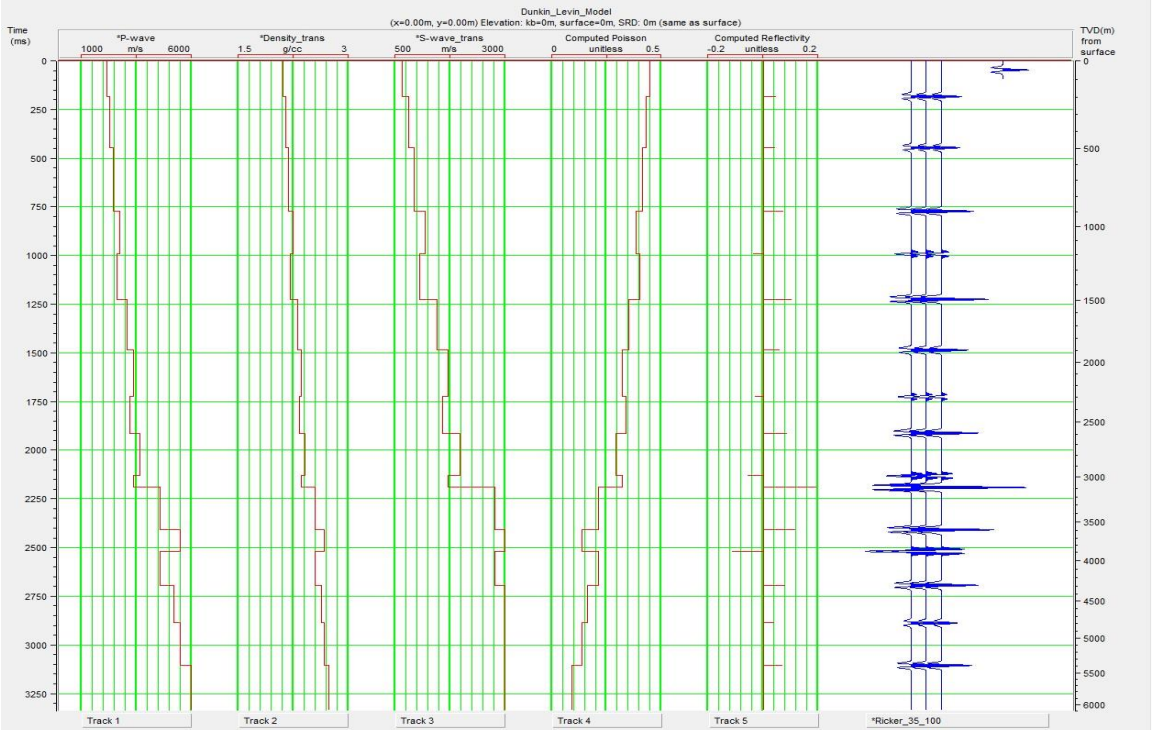

Fig. 3.39. Profiles of computed Poisson's ratio (track 4) and reflectivity series (track 5) of Dunkin and Levin's model including zero-offset synthetic seismogram with the generated 35Hz Ricker wavelet (blue colored one).

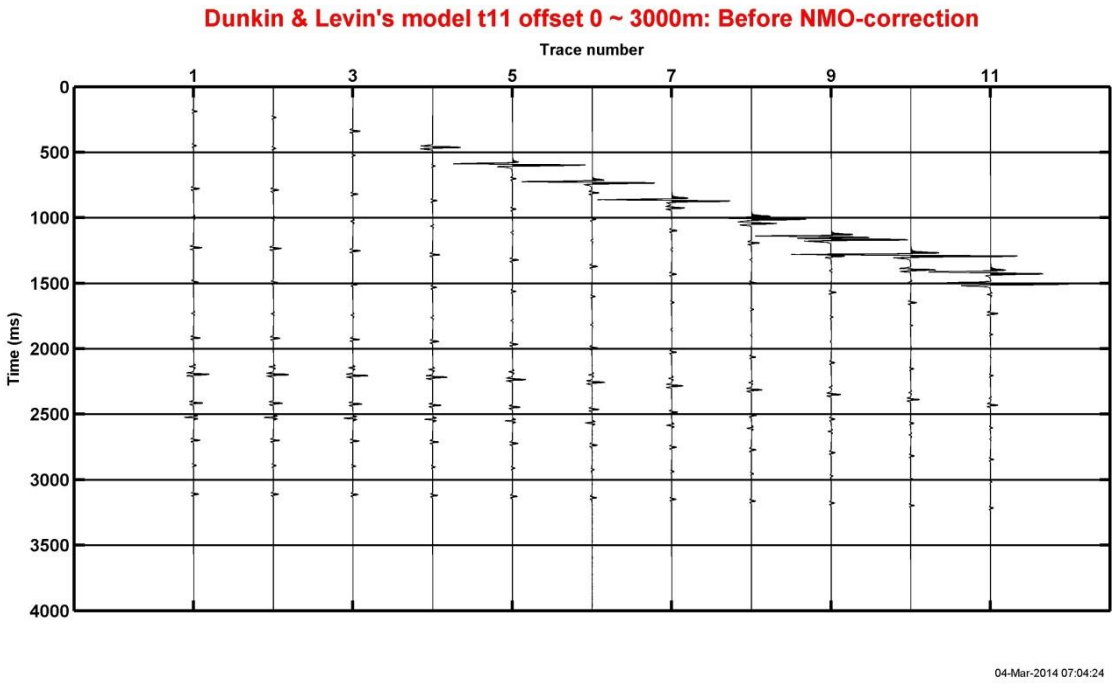

Fig. 3.40. Synthetic CMP gather of Dunkin and Levin's model (Before applying NMO-correction).

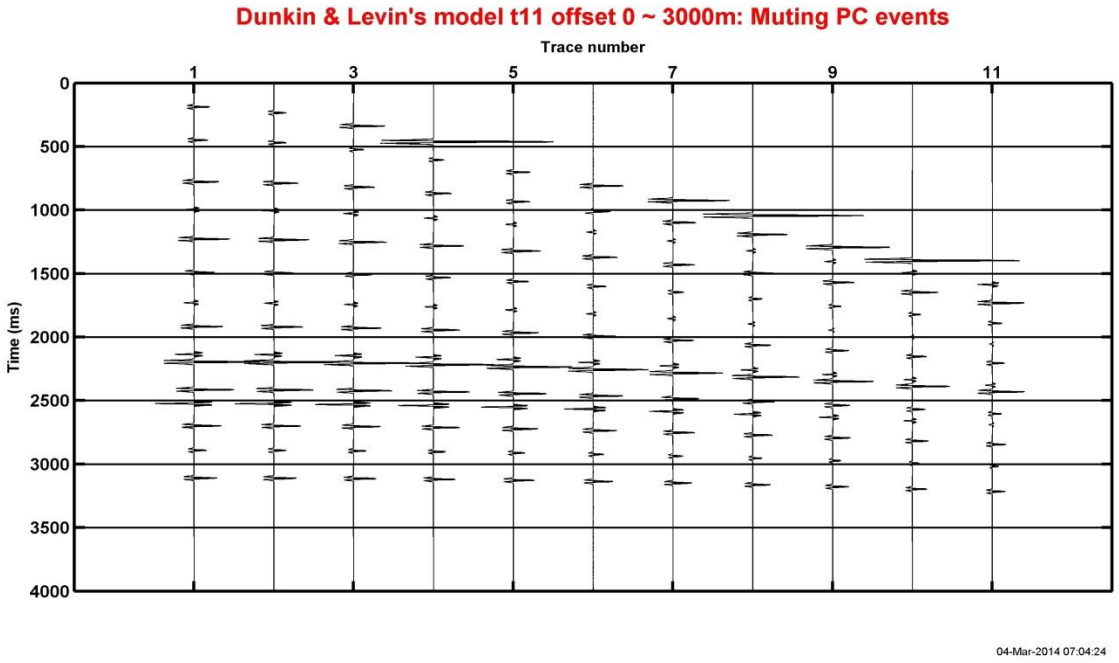

Fig. 3.41. Synthetic CMP gather of Dunkin and Levin's model (Before applying NMO-correction), post-critical events in Figure 3.40 are muted now.

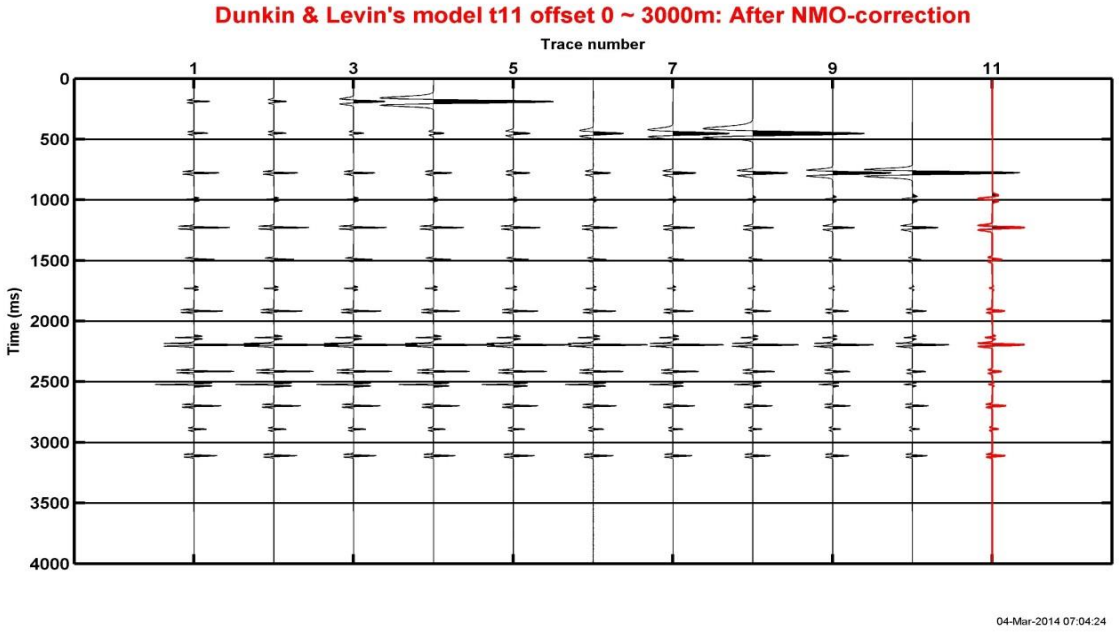

Fig. 3.42. Synthetic CMP gather of Dunkin and Levin's model (After applying NMO-correction). The red-colored trace, the 11th trace located at 3000 meter farthest offset, is selected for applying NMO-stretch correction.

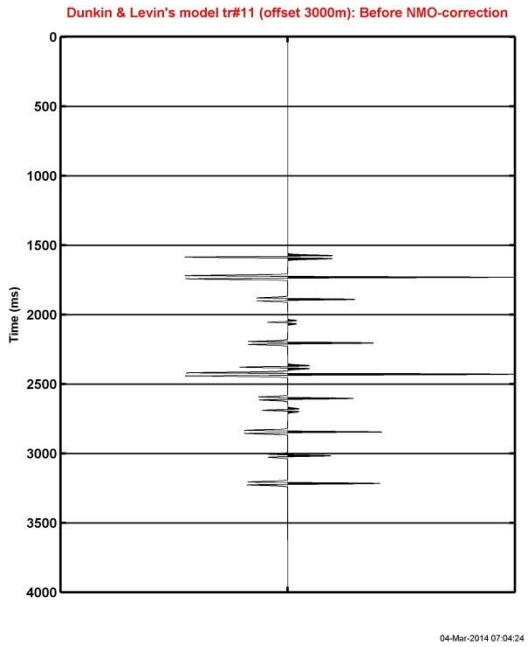

Fig. 3.43. The 11th trace, located at 3000 meter offset in Dunkin and Levin's model (Before NMO-correction).

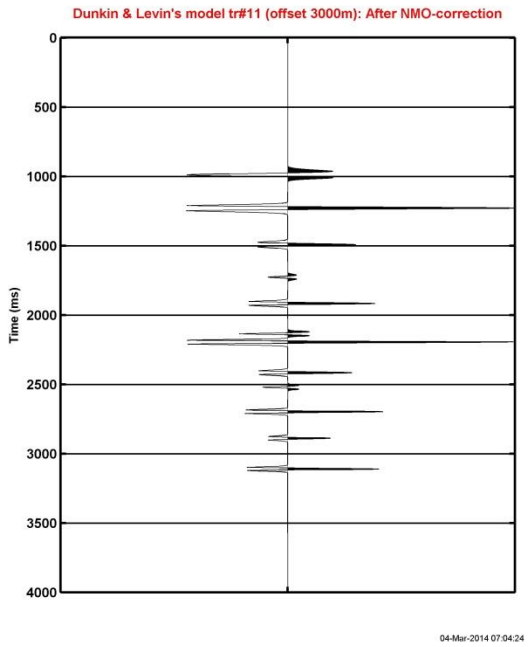

Fig. 3.44. The 11th trace, located at 3000 meter offset in Dunkin and Levin's model (After NMO-correction).

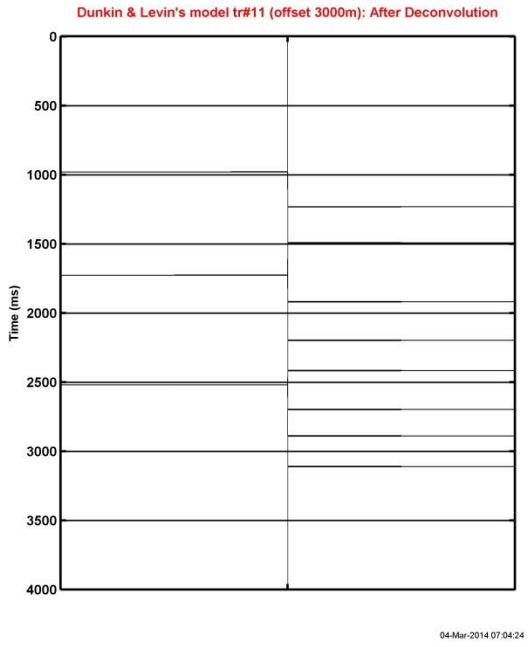

Fig. 3.45. The 11th trace, located at 3000 meter offset in Dunkin and Levin's model (After sparse-deconvolution).

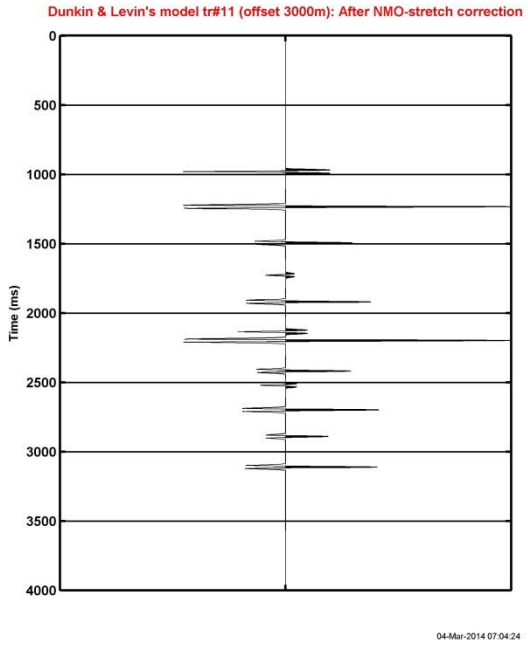

Fig. 3.46. The 11th trace, located at 3000 meter offset in Dunkin and Levin's model (After NMO-stretch correction).

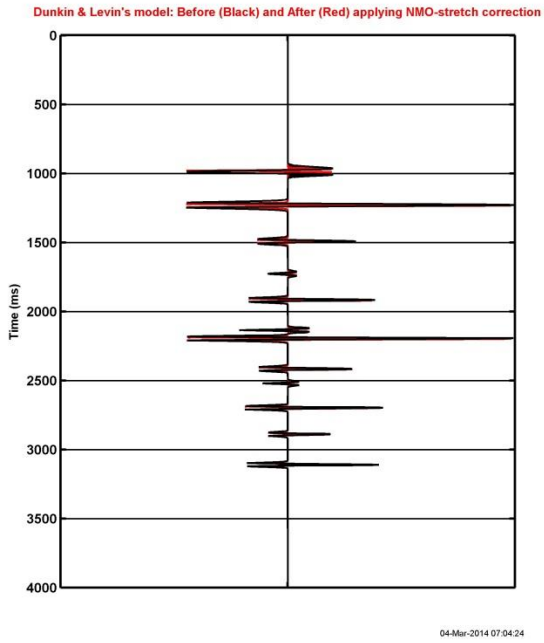

Fig. 3.47. The 11th trace, located at 3000 meter offset in Dunkin and Levin's model, before (black-colored trace) and after (red-colored trace) applying NMO-stretch correction.

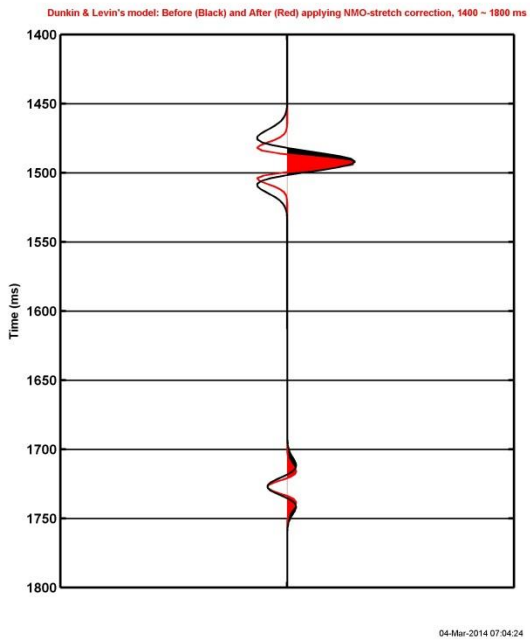

Fig. 3.48. The 11th trace, located at 3000 meter offset in Dunkin and Levin's model, before (black-colored trace) and after (red-colored trace) applying NMO-stretch correction, 1400 ~ 1800 milliseconds.

the selected traces, which are before (Figure 3.49 (a)) and after applying NMO-correction (Figure 3.49 (b)), and after applying NMO-stretch correction (Figure 3.49 (c)). In Figure 3.49 (b), we could observe the tendency of NMO-stretch more obviously compared to the results in the STFT for the first and second models. Along with decrease in time depth, the dominant frequencies move toward lower frequencies. That is, the waveform distortions arise more severely in shallow depths. After NMO-stretch correction, the observed distortions are corrected. Every dominant frequency of wavelets on the trace is located at 35Hz, the dominant frequency of convolved Ricker wavelet. CWT and CLSSA results also verify the effectiveness of the NMO-stretch correction with better time-frequency representation (Figure 3.50). To observe the effect in detail,

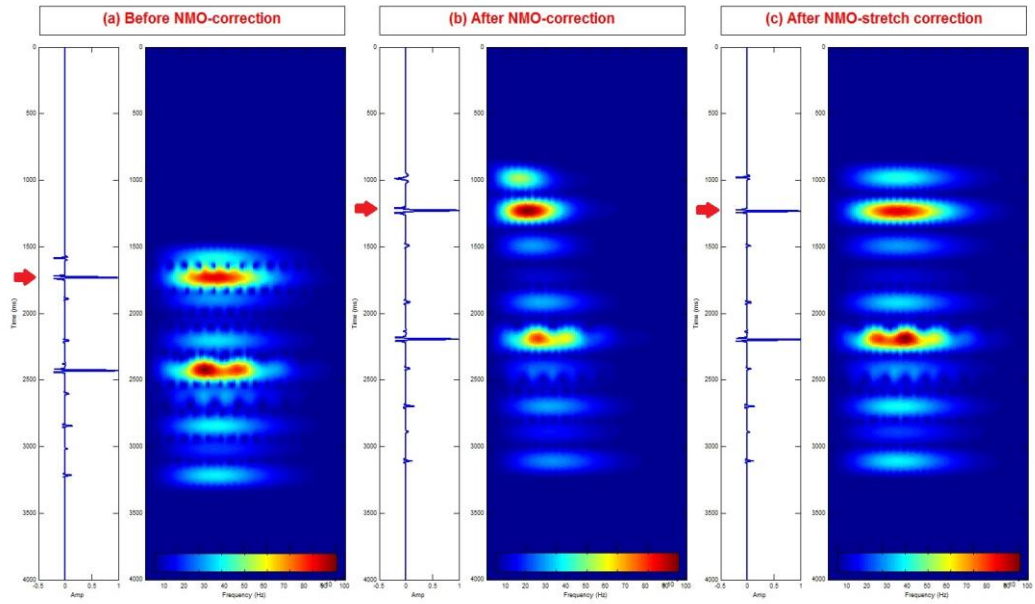

Fig. 3.49. The 11th trace of Dunkin and Levin's model and its time-frequency panels applying STFT. (a) Before NMO-correction, (b) After NMO-correction and (c) After NMO-stretch correction. Red arrows indicate targeted wavelets which are described in Figure 3.50.

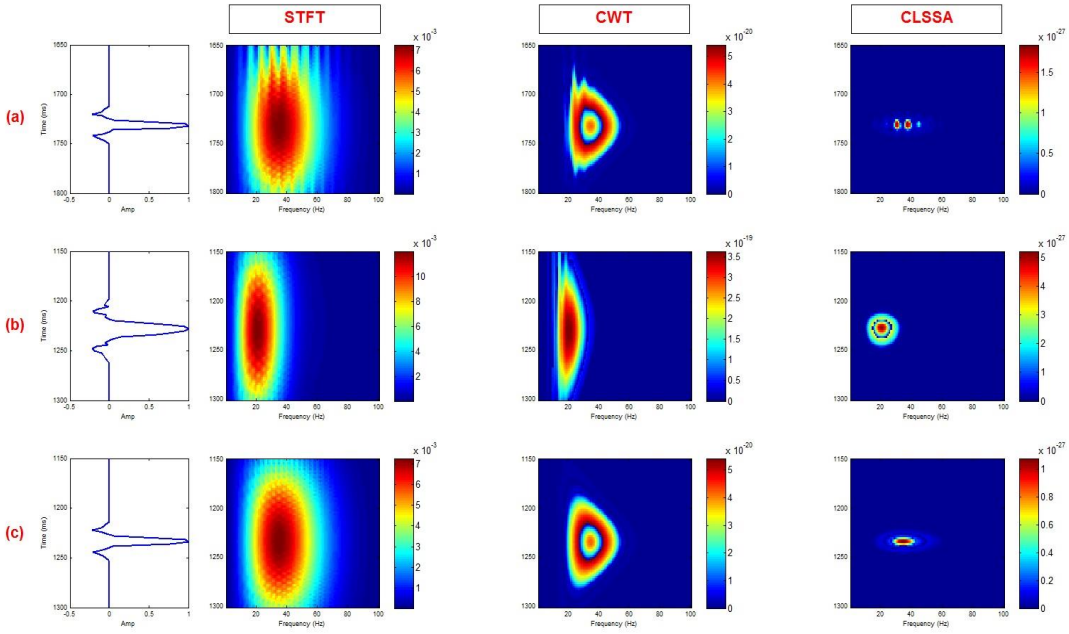

Fig. 3.50. Selected segments on the 11th trace of Dunkin and Levin's model and their time-frequency panels applying STFT (left), CWT (middle), and CLSSA (right). (a) Before NMO-correction, 1650 ~ 1800 milliseconds of the trace shown in Figure 3.49 (a), (b) After NMO-correction, 1150 ~ 1300 milliseconds of the trace shown in Figure 3.49 (b), (c) After NMO-stretch correction, 1150 ~ 1300 milliseconds of the trace shown in Figure 3.49 (c).

a time section, 1650 ~ 3200 milliseconds, is selected for the uncorrected trace (top, Figure 3.50 (a)), and a corresponding time section, 1150 ~ 1300 milliseconds, is chosen for the trace after NMO-correction (middle, Figure 3.50 (b)) and the trace after NMO-stretch correction (bottom, Figure 3.50 (c)). The specific time locations of selected time sections are depicted in red arrows in Figure 3.49. In all time-frequency representations, waveform changes before and after applying NMO-correction are observed and corrected. Again, the interferences detected in Figure 3.50 (a) occur due to adjacent events near selected wavelet.

3.5 Application NMO-stretch correction to real data

3.5.1 Data and wavelet description

With the aim of validating the effectiveness of NMO-stretch correction, the author applies this research to real well-log data from Hitts Lake Field, Smith County, onshore Texas. The location of the field is illustrated in Figure 3.51. In the tests on the synthetic models conducted above, the effectiveness of the NMO-stretch correction was clearly verified with ideal circumstances. However, the application of field data that includes noise will strengthen validation of the method to correct waveform changes in a more complicated situation. A well-log named 'Hitts Lake #124' was chosen from Hitts Lake Field data. Figure 3.52 illustrates p-wave slowness information of sonic log (left, Figure 3.52) and its time-depth curve for depth to time conversion (right, Figure 3.52). Considering only processed post-stack seismic data, which corresponds to the selected well-log, are available for this application, a new synthetic CMP gather has to be generated for further processing. For the generation of this gather, we have to solve the upscaling problem between measured log-data and corresponding seismogram. A profile of four milliseconds

averaged slowness is newly computed from the sonic log data by using four milliseconds sliding averaging and the time-depth curve. The profiles of slowness before (red) and after (blue) applying 4 milliseconds averaging are compared in Figure 3.53. The reason why 4 milliseconds is set for averaging is that processing sample rate of corresponding post-stack seismic data is 4 milliseconds. Even though applying a Backus average is the most accurate way to solve upscaling problem compared to using arithmetic or RMS average (Mukerji et al, 1995), Backus averaging needs additional density information to apply, thus simple arithmetic averaging is used to generate the averaged slowness. Additionally, a new Ricker wavelet and well-log set including profiles of density and slowness of S-wave are generated for preparation of CMP gather generation. In order to generate a density profile and profile of S-wave slowness from P-wave velocity information, Gardner's empirical relation (Gardner et al., 1974) and Greenberg-Castagna's V_P-V_S relations (Greenberg and Castagna, 1992) are applied again (Figure 3.54). In addition, to show the effectiveness of NMO-stretch correction, the wavelet has a 50Hz dominant frequency (Figure 3.55). It also has a 100 milliseconds wavelet length, 2 milliseconds sampling rate, and linear phase with zero phase rotation. Figure 3.56 illustrates the corresponding profiles of computed Poisson's ratio of the data (track 4), reflectivity series (track 5), and zero-offset synthetic seismogram with the designed Ricker wavelet (rightmost track). By implementing the Zoeppritz equation with the parameters above, the uncorrected synthetic CMP gather is generated (Figure 3.57). Below are the designed parameters for the synthetic CMP modeling:

- Target zone: 1638 ~ 2259 (m)
- Geometric spreading, transmission losses, array effects and muting of post-critical events are not applied.
- Number of offset: 11

- Offset range: 0 ~ 3000 (m), Trace interval: 300 (m)
- Model blocking: travel-time (slowness) average
- Time window to model: 0 ~ 1500 (ms)
- Processing sample rate: 1 (ms)
- Output domain: time
- Output sample rate: 2 (ms)

For better presentation, 750 ~ 1400 milliseconds is selected and magnified in Figure 3.58. Red-colored boundaries are targeted to test the effectiveness of the NMO-stretch correction for this CMP gather, since the author applies the NMO-stretch correction as a target-oriented method only to the events of interest. The correction is conducted in following subchapter 3.5.2.

3.5.2 Application

Figure 3.59 shows the generated CMP gather from the log data and red-colored events of interest after NMO-correction. Despite the fact that the waveforms on the targeted boundaries are distorted after NMO-correction, it is difficult to distinguish the waveform changes and their tendencies with naked eyes. However, after applying NMO-stretch correction, we could observe the differences between waveforms on targeted boundaries before (black) and after applying NMO-stretch correction (red) in Figure 3.60. Notice that the red-colored boundaries in Figure 3.60 represent not only targeted but also NMO-stretch corrected boundaries now. The targeted events in 825 ~ 865 milliseconds are magnified in Figure 3.61. The stretched wavelets (black) in far offset ranges are observed and corrected into narrower wavelets after the target oriented

NMO-stretch correction (red). The validation of the method for correcting NMO-stretch is extended to an application of real data.

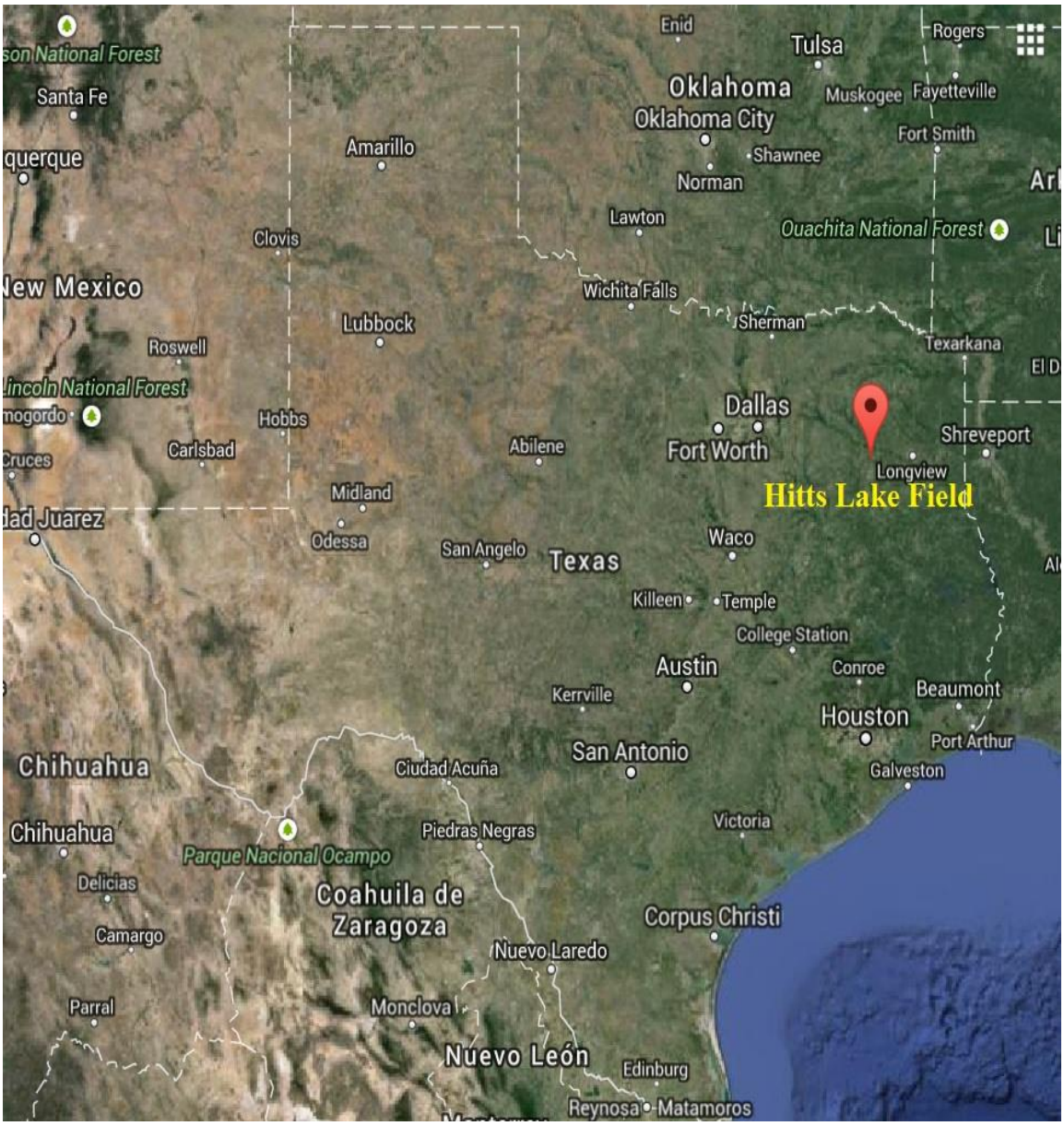

Fig. 3.51. Location of Hitts Lake Field, located North of Tyler in Smith County (red mark), onshore Texas (Figure courtesy: Google maps available at https://www.google.com/maps/)

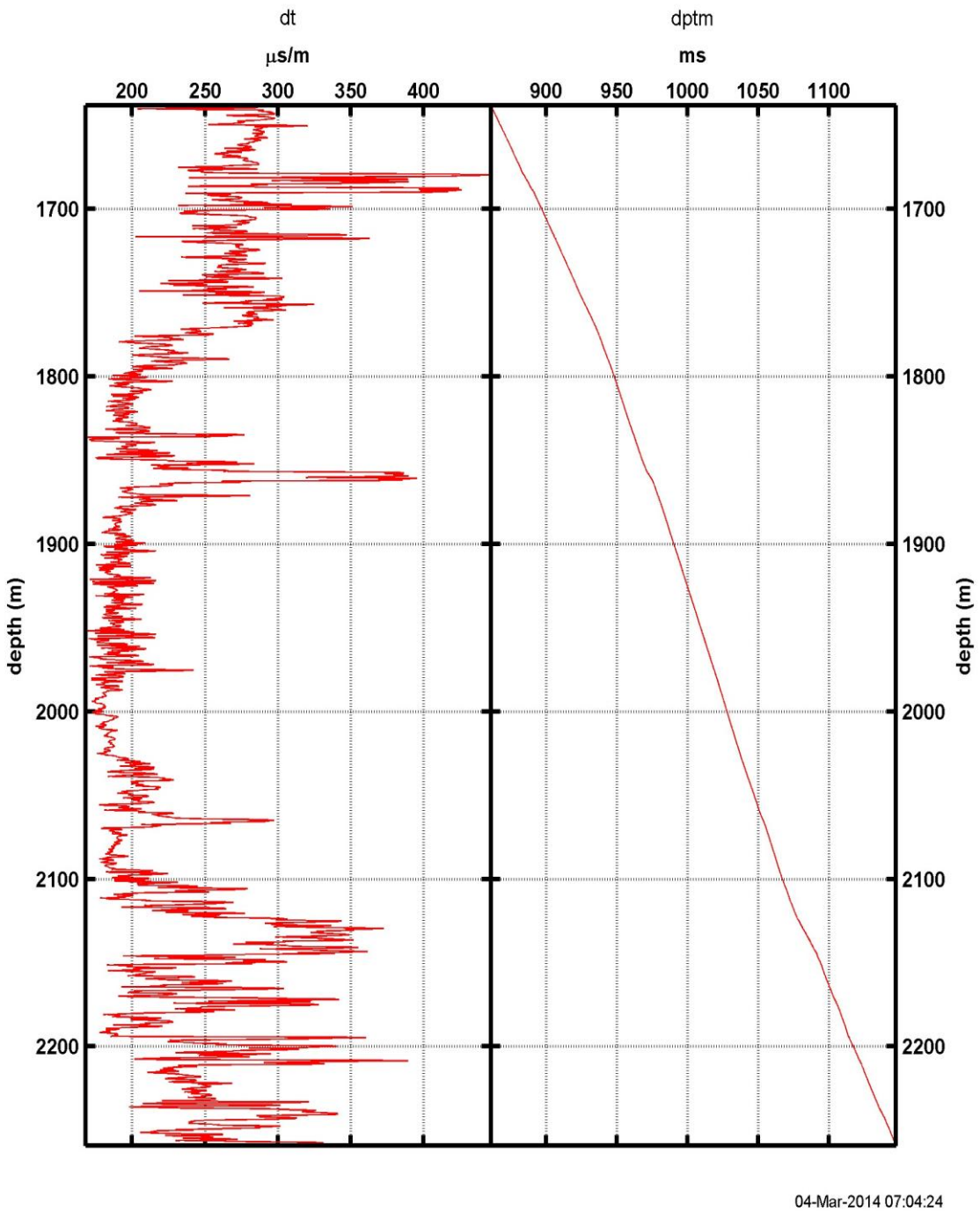

Fig 3.52. 'Hitts Lake #124', P-wave slowness profile (µs/m) (left) and its time-depth curve (right)

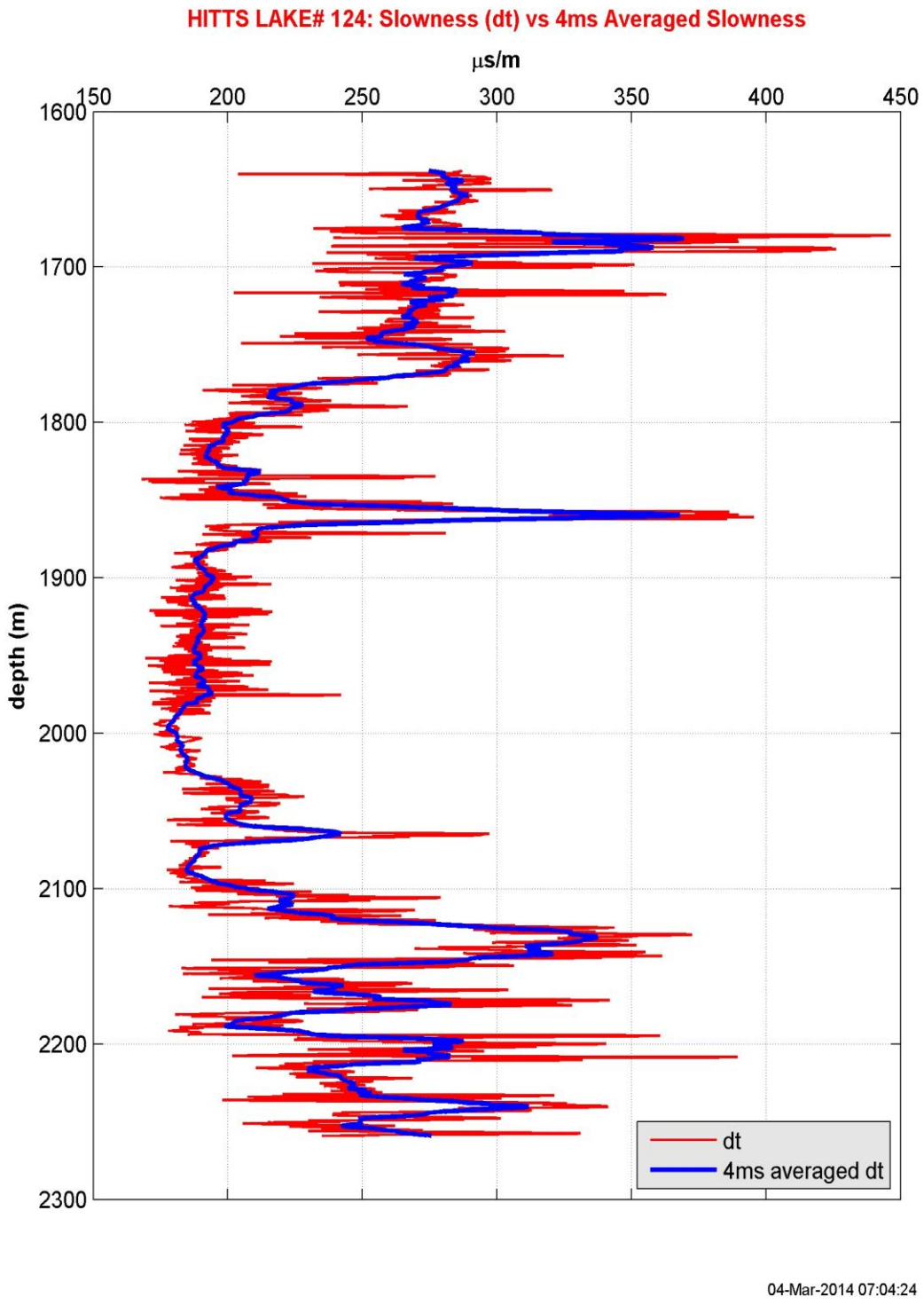

Fig 3.53. 'Hitts Lake #124', P-wave slowness profile (μs/m) (red) and 4 milliseconds averaged slowness (blue).

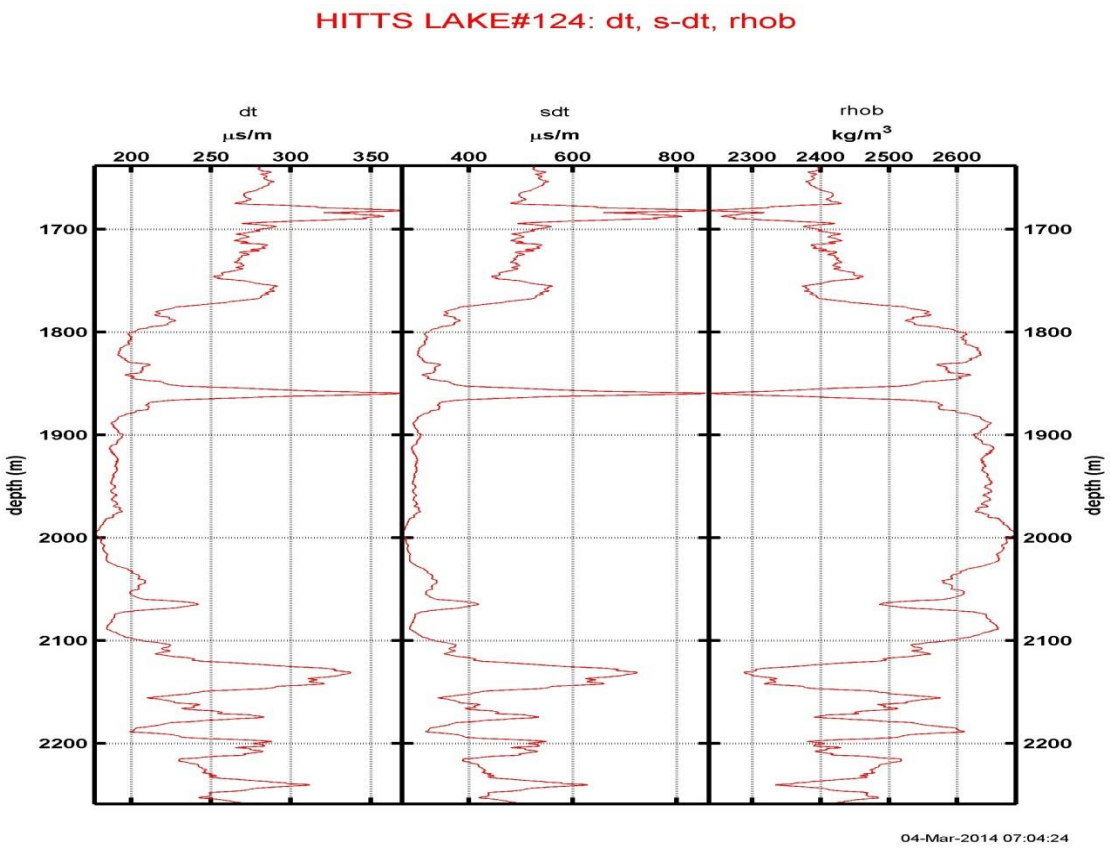

Fig. 3.54. Profiles of 4 milliseconds averaged P-wave slowness (left), newly computed S-wave slowness (middle) and density (right).

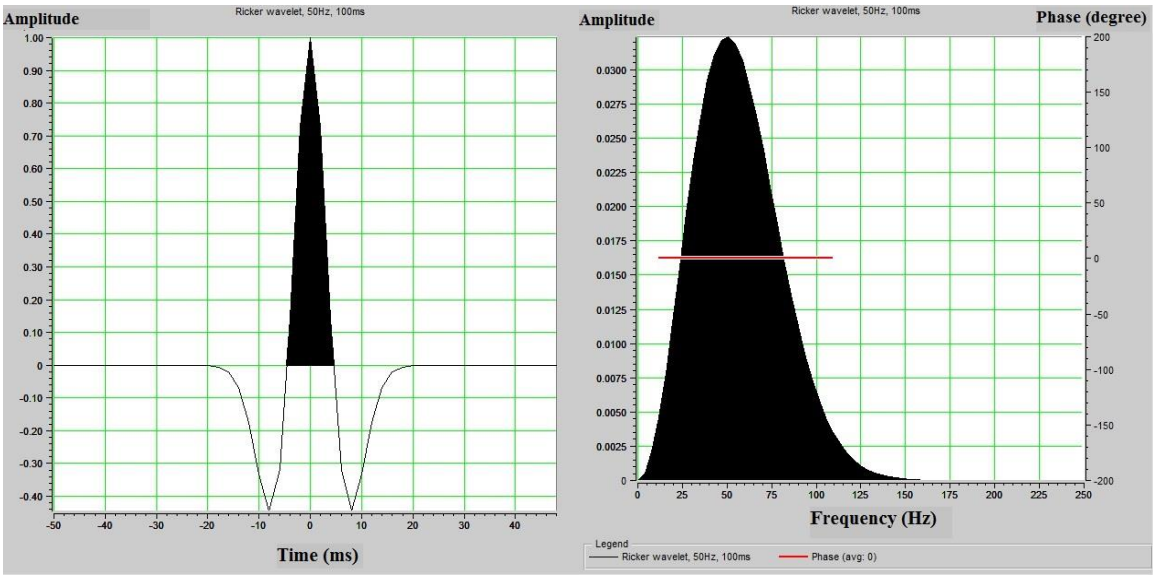

Fig. 3.55. A designed Ricker wavelet (left) and its amplitude spectrum in frequency domain (right), 50Hz dominant frequency, zero phase, and 2ms sampled.

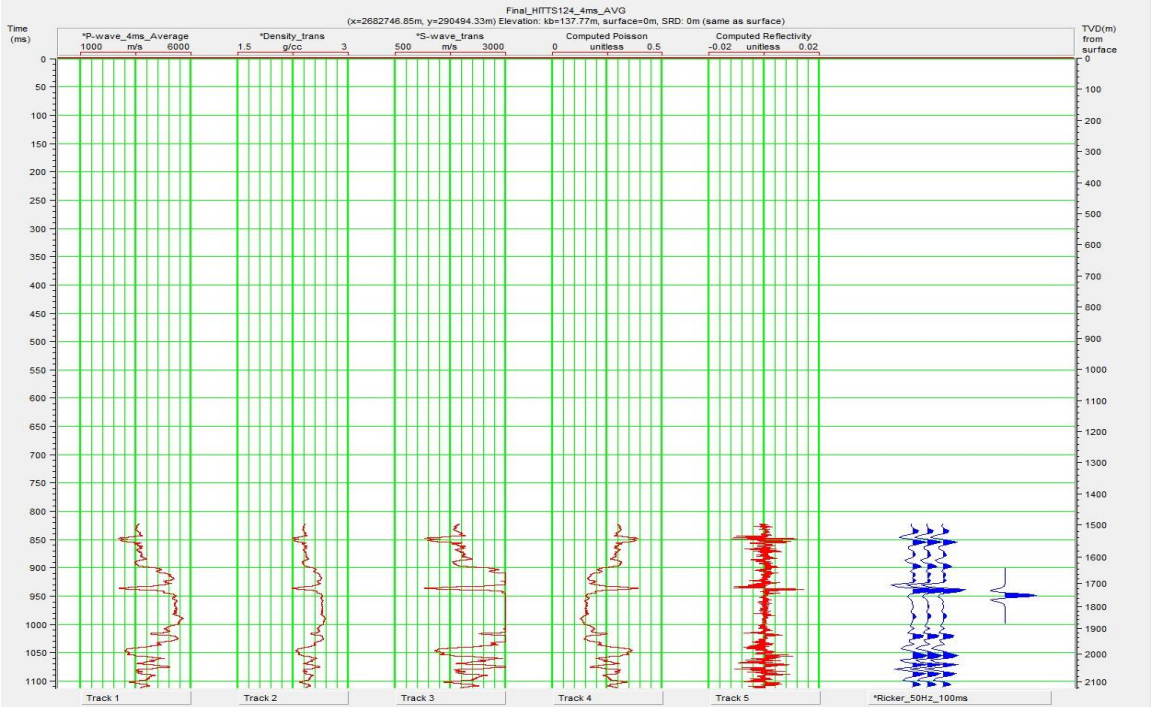

Fig. 3.56. Profiles of computed Poisson's ratio (track 4) and reflectivity series (track 5), which correspond to averaged Hitts Lake #124, including zero-offset synthetic seismogram with the generated 50Hz Ricker wavelet (blue colored one).

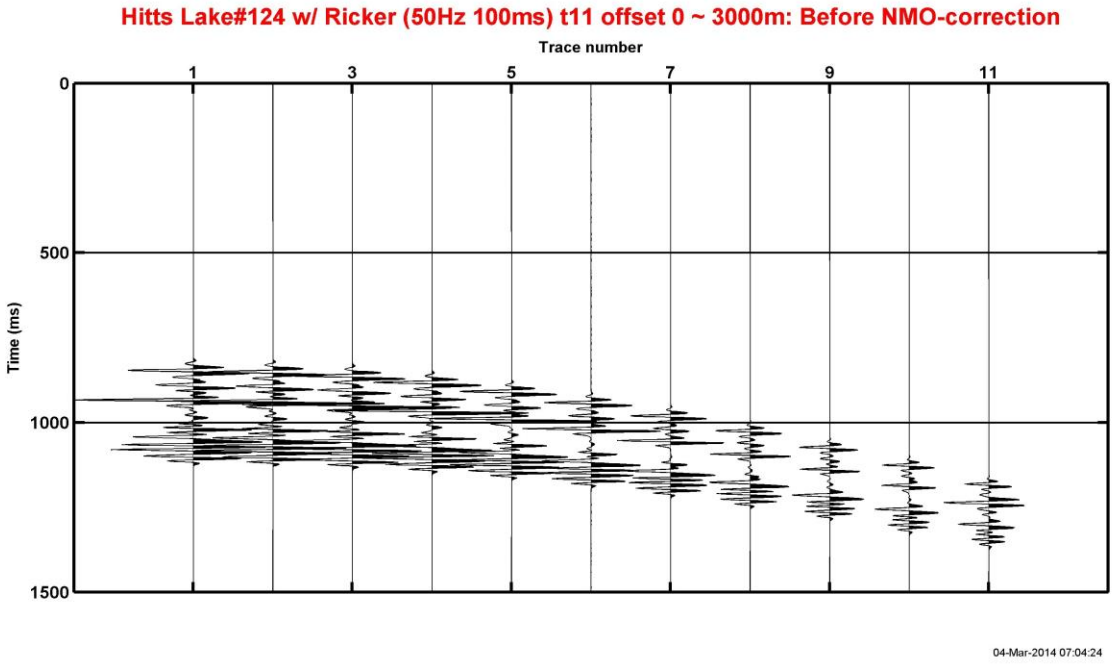

Fig. 3.57. Synthetic CMP gather generated from 'Hitts Lake #124' (Before applying NMO-correction).

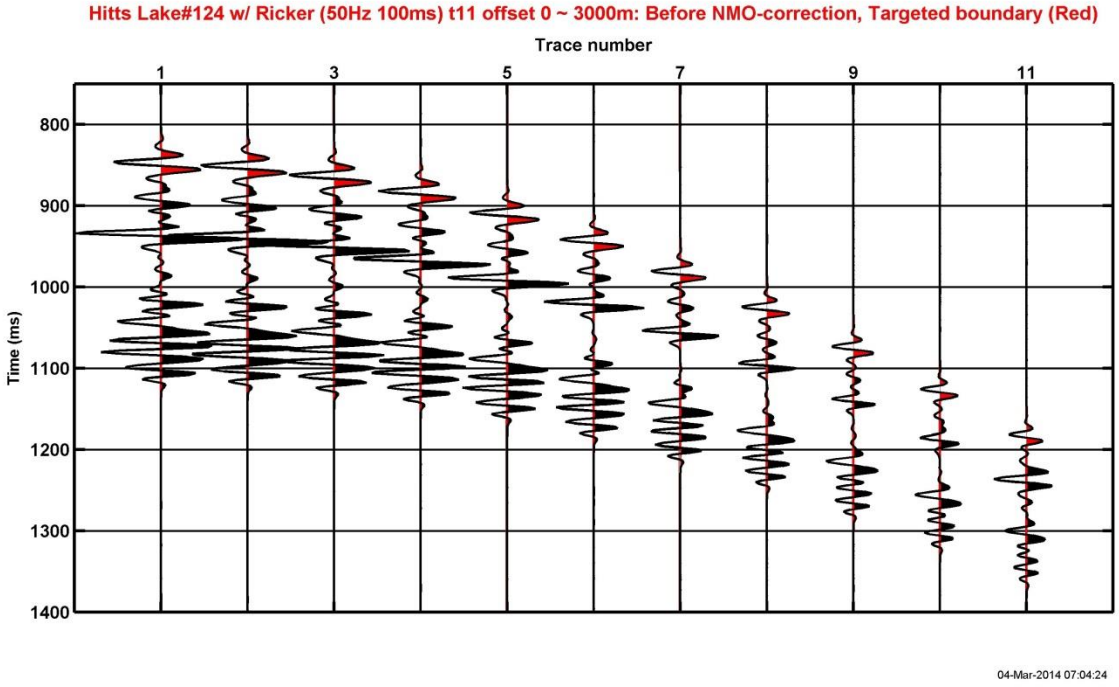

Fig. 3.58. Synthetic CMP gather in Figure 3.57, 750 ~ 1400 milliseconds is selected and magnified. Red-colored boundaries represent targeted events of interest.

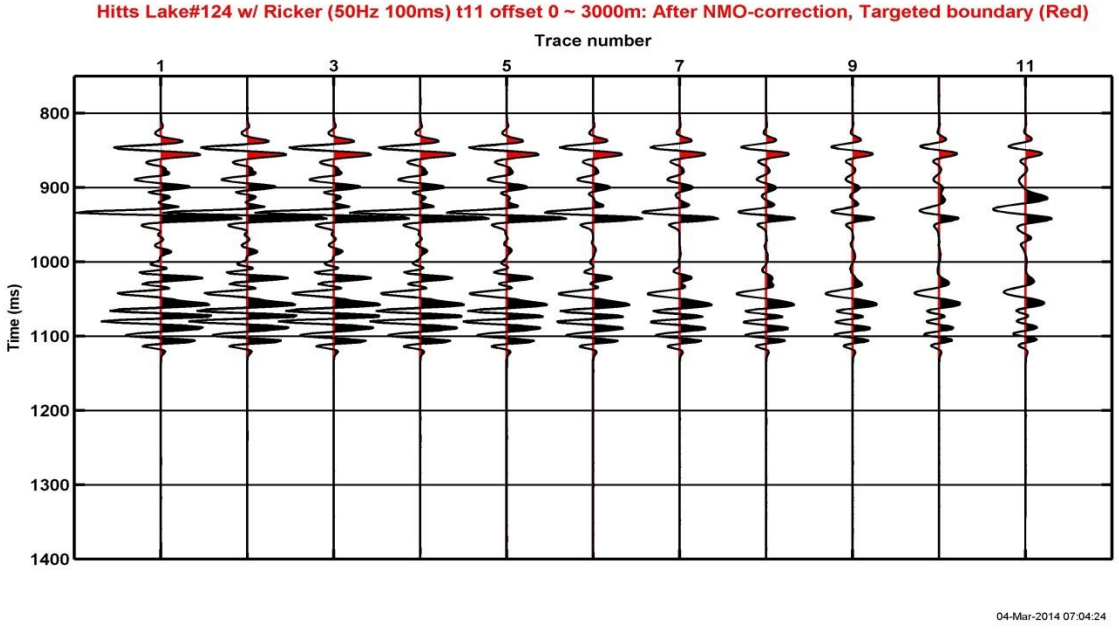

Fig. 3.59. Synthetic CMP gather generated from 'Hitts Lake #124' (After applying NMO-correction). Red-colored boundaries represent targeted events of interest.

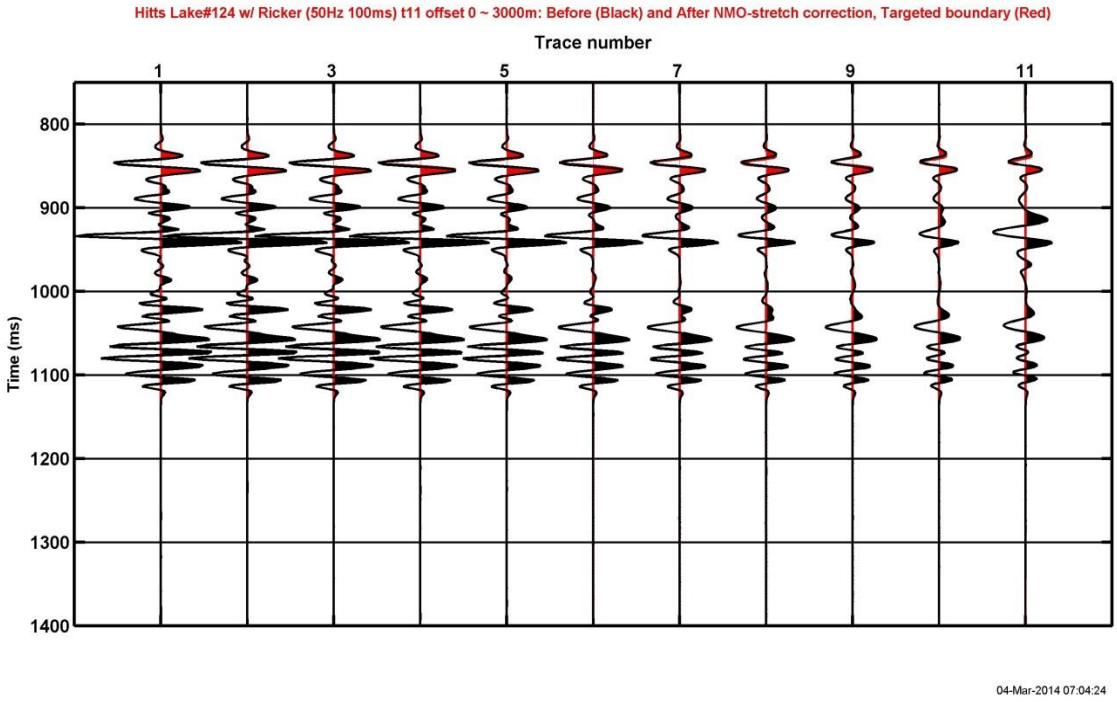

Fig. 3.60. Synthetic CMP gather generated from 'Hitts Lake #124' (After applying NMO-stretch correction). Red-colored boundaries represent targeted events of interest.

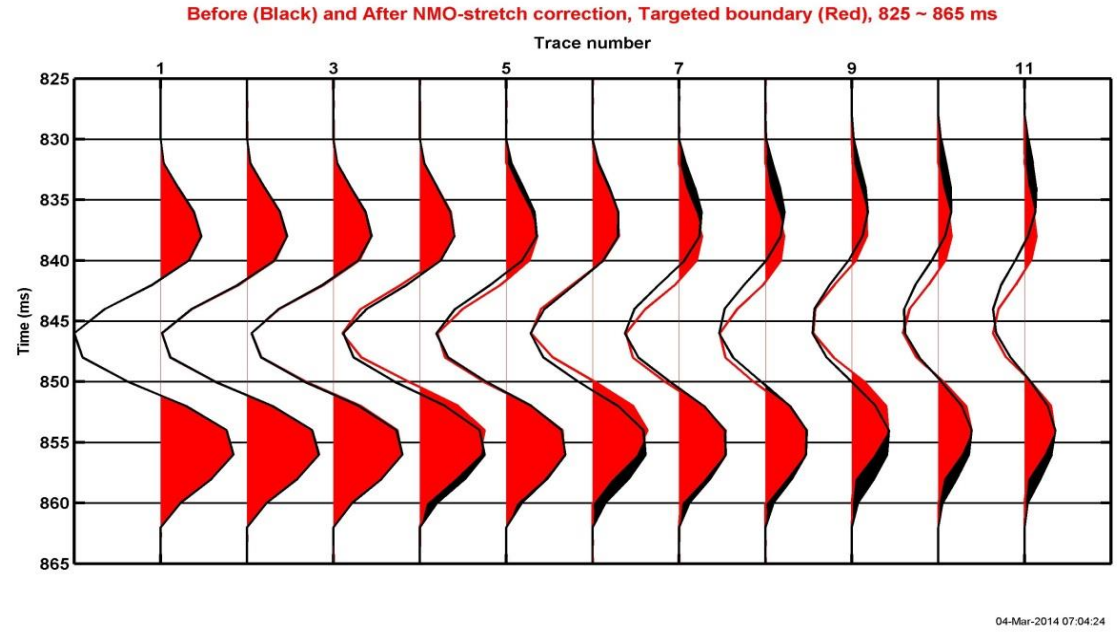

Fig. 3.61. Synthetic CMP gather in Figure 3.60, 825 ~ 865 milliseconds is selected and magnified. Black-colored wavelets correspond to events of interest before NMO-stretch correction and Red-colored wavelets represent the NMO-stretch corrected results.

3.6 Conclusion of correction

To correct the investigated waveform changes in the 1st and 2nd models, Casotoro et al.'s wavelet deconvolution method (2001) was applied. In addition, Dunkin and Levin's model (1973) was reproduced and an application to real-data was conducted to confirm the effectiveness of the NMO-stretch correction for a better understanding of more realistic situation. The typical tendency of NMO-stretch was observed. After applying the NMO-stretch correction, the investigated and newly observed waveform distortions were successfully corrected. STFT, CWT, and CLSSA time-frequency representations helped to verify the validation of correction. Among these spectral decomposition methods, CLSSA showed the best resolution.

CHAPTER IV

CONCLUSION

To quantitatively determine waveform changes arising from NMO-stretch, investigations of the synthetic models were conducted. The general tendency of NMO-stretch with increased offset is progressive reductions of bandwidth and shifts toward lower frequencies. By computing Dunkin and Levin's Stretch-ratio for the models, the tendencies were successfully illustrated again and degrees of waveform distortions were quantitatively determined. In the investigation of the 2nd model set, we could test the possibility of the Dunkin and Levin's Stretch-ratio as a new seismic attribute for reservoir characterization. Since the degrees of NMO-stretch for gas-saturated and brine-saturated cases, which correspond to AVO Classes 3, 2, and 1, were noticeably separated with the investigated values of Stretch-ratio in far offset ranges, it indicates that gas and wet situations concerning typical AVO Classes could be differentiated by proper investigation of NMO-stretch at far offsets in pre-stack seismic data. For correction of investigated waveform changes in the models, the Casotoro et al.'s wavelet deconvolution method (2001) was applied. The proposed method was also applied to Dunkin and Levin's model (1973) and targeted reflections in Hitts Lake Field data, in order to confirm the effectiveness of NMO-stretch correction. After applying NMO-stretch correction, the investigated and newly observed waveform distortions arising from NMO-stretch were successfully corrected. The results of applying STFT, CWT, and CLSSA were also presented. The time-frequency representations help to verify the validation of correction. The achieved objectives of this thesis are as the following:

1. Quantitative investigation of waveform changes arising from NMO-stretch in proposed models with the Stretch-ratio (Dunkin and Levin, 1973),

2. Testing of the Stretch-ratio as a new seismic attribute for reservoir characterization,

3. Applying the wavelet deconvolution method (Casotoro et al., 2001) into the proposed model including correction of investigated waveform changes,

4. Validation of the NMO-stretch correction with state-of-the-art time-frequency analyses,

5. Application of the correction: with the synthetic seismogram based on real data, Hitts Lake Field, onshore Texas.

Although the objectives of this thesis were achieved successfully with Dunkin and Levin's stretch ratio and Castoro's wavelet deconvolution-based NMO-stretch correction, the proposed NMO-stretch correction was tested and the effectiveness of the correction was verified under the condition that tuning effects are excluded. Tuning effects could be described as constructive or destructive interference of adjacent reflection events. The effect arises from two or more reflectors spaced closer than a quarter of the dominant wavelet length (Widess, 1973). A newly devised CMP gather corresponding gas-saturated AVO Classes describes the tuning effect in Figure 3.62. This gather is revised from the gather described in Figure 2.29. Each bed thickness is now changed from 250 meters to 50 meters for generating tuning effects. A red-colored trace located at 6300 meter offset is targeted to show the details. The trace is illustrated in Figure 3.63. Top and bottom reflections of each gas-saturated bed of AVO Class 3 (Figure 3.64), Class 2 (Figure 3.65), and Class 1 (Figure 3.66) on the trace are selected and magnified. Especially for the reflections of Class 2 and 1, destructive and constructive interferences due to tuning effects

are observed. Since these tuned events cause severe difficulty in investigating and extracting the original wavelets on the target trace before applying NMO-correction because of existence of interferences, when tuned events arise, direct application of the proposed NMO-stretch correction was not feasible. Future works should therefore include investigation of and correction for waveform changes arising not only from NMO-stretch, but also from tuning effects. Interpolations of Dunkin and Levin's stretch ratios for tuned reflections, which could be achieved by investigation of the stretch ratio, and directly shifting the distorted frequency amplitudes to the right frequency location by applying investigated and interpolated stretch ratios would be effective for correction of tuned events. Attenuation, the reduction in amplitude or energy caused by transmitting media (Sheriff, 2002), should be handled in future works for elaborate investigation and correction. Moreover, if pre-stack seismic data are available for future research, it would definitely show the effectiveness of the proposed method in more realistic and specific situation.

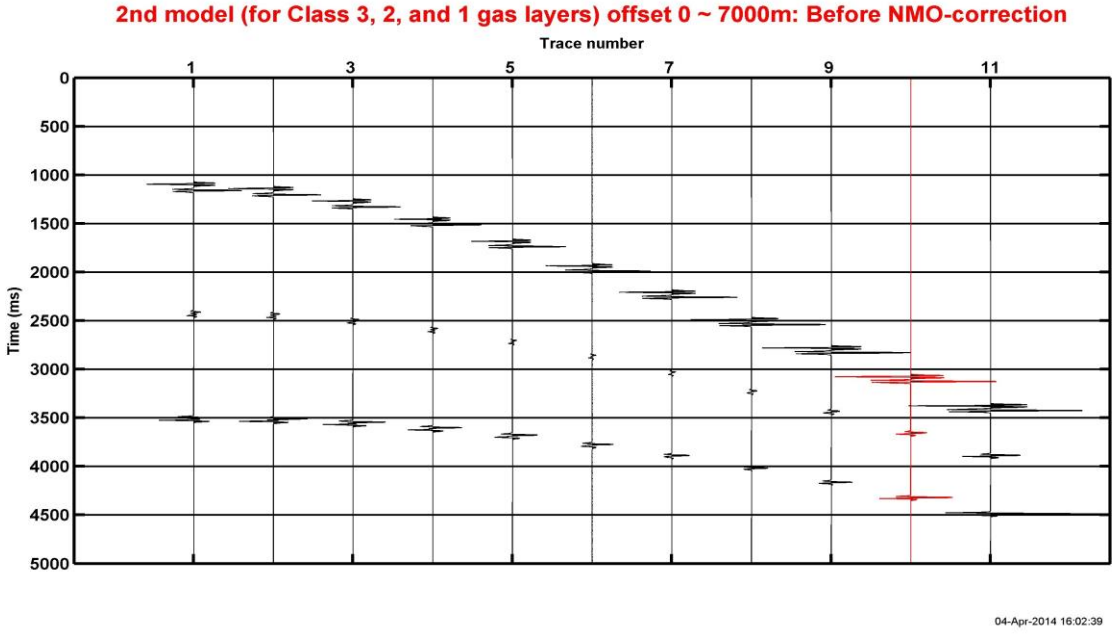

Fig. 3.62. Synthetic CMP gather of gas-saturated model to investigate tuning effects (Before NMO-correction). The 10th trace (red-colored trace), located at 6300 meter offset on the gather, is selected for the investigation.

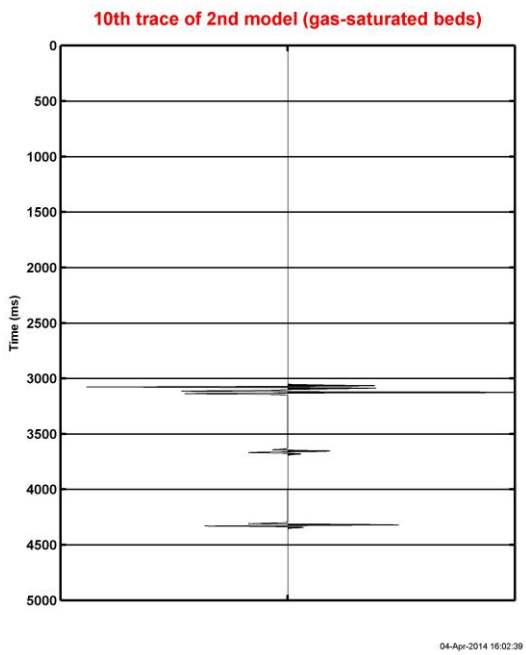

Fig. 3.63. The 10th trace, located at 6300 meter offset on the gas-saturated model in Figure 3.62 (Before NMO-correction).

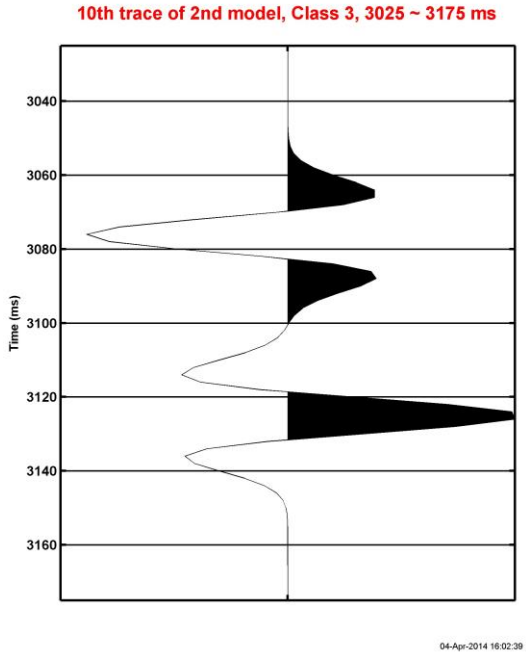

Fig. 3.64. The 10th trace in Figure 3.62, 3025 ~ 3175 milliseconds, top and bottom reflections of the gas-saturated bed for AVO Class 3.

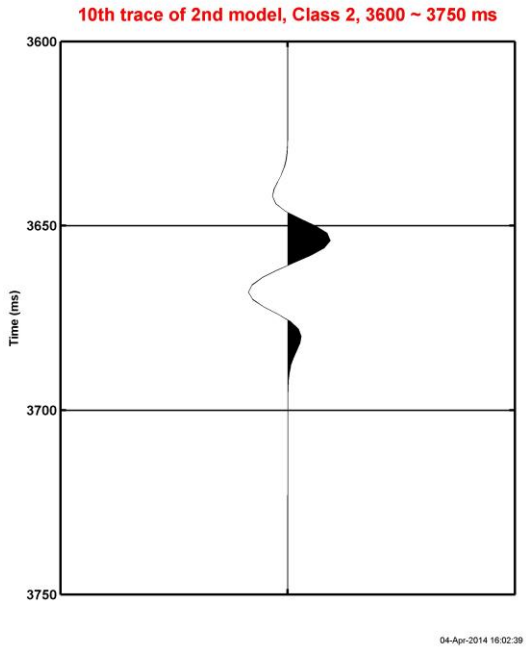

Fig. 3.65. The 10th trace in Figure 3.62, 3600 ~ 3750 milliseconds, top and bottom reflections of the gas-saturated bed for AVO Class 2.

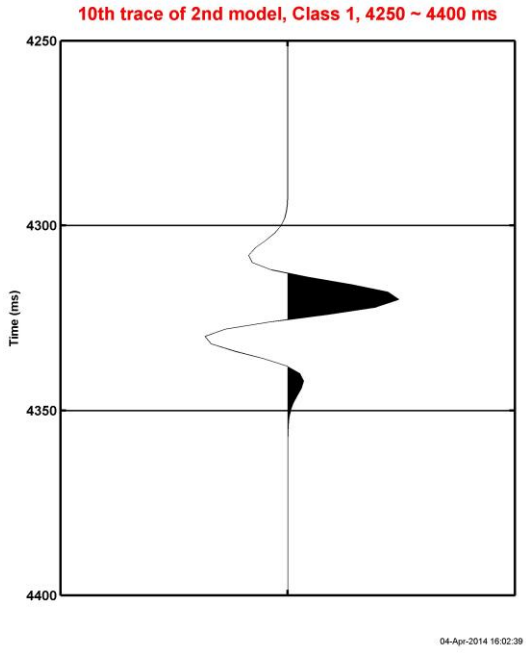

Fig. 3.66. The10th trace in Figure 3.62, 4250 ~ 4400 milliseconds, top and bottom reflections of the gas-saturated bed for AVO Class 1.

APPENDIX A

THE ZOEPPRITZ EQUATION

The Zoeppritz equations are a set of equations that describe the partitioning of seismic wave energy at an interface, typically a boundary between two different layers of rock. Zoeppritz (1919) solved the amplitudes of reflected and transmitted waves using the conservation of stress and displacement across the layer boundary, which provides the equations with respect to incident angle, densities, and elastic moduli. It can be expressed as following matrix:

$$\begin{bmatrix} R_P(\theta_1) \\ R_S(\theta_1) \\ T_P(\theta_1) \\ T_s(\theta_1) \end{bmatrix} = \begin{bmatrix} -\sin\theta_1 & -\cos\emptyset_1 & \sin\theta_2 & \cos\emptyset_2 \\ \cos\theta_1 & -\sin\emptyset_1 & \cos\theta_2 & -\sin\emptyset_2 \\ \sin 2\theta_1 & \frac{V_{P1}}{V_{S1}}\cos 2\emptyset_1 & \frac{\rho_2 {V_{S2}}^2 V_{P1}}{\rho_1 {V_{S1}}^2 V_{P2}}\cos 2\emptyset_1 & \frac{\rho_2 V_{S2} V_{P1}}{\rho_1 {V_{S1}}^2}\cos 2\emptyset_2 \\ -\cos 2\emptyset_1 & \frac{V_{S1}}{V_{P1}}\sin 2\emptyset_1 & \frac{\rho_2 V_{P2}}{\rho_1 V_{P1}}\cos 2\emptyset_2 & -\frac{\rho_2 V_{S2}}{\rho_1 V_{P1}}\sin 2\emptyset_2 \end{bmatrix}^{-1} \begin{bmatrix} \sin\theta_1 \\ \cos\theta_1 \\ \sin 2\theta_1 \\ \cos 2\emptyset_1 \end{bmatrix}$$

where, R_P, R_S, T_P, and T_s are the reflected P, reflected S, transmitted P, and Transmitted S-wave amplitude coefficients. Furthermore, when θ_1 represents the incident angle of P-wave, θ_2, $\emptyset_1$, $\emptyset_2$ correspond to the angle of transmitted P-wave and the angle of reflected and transmitted S-wave. These parameters are illustrated in Figure A.1. Inverting the matrix form provides the exact amplitudes as a function of angles described above. Figure A.1 describes the mode conversion for a P-wave incident on a planar boundary.

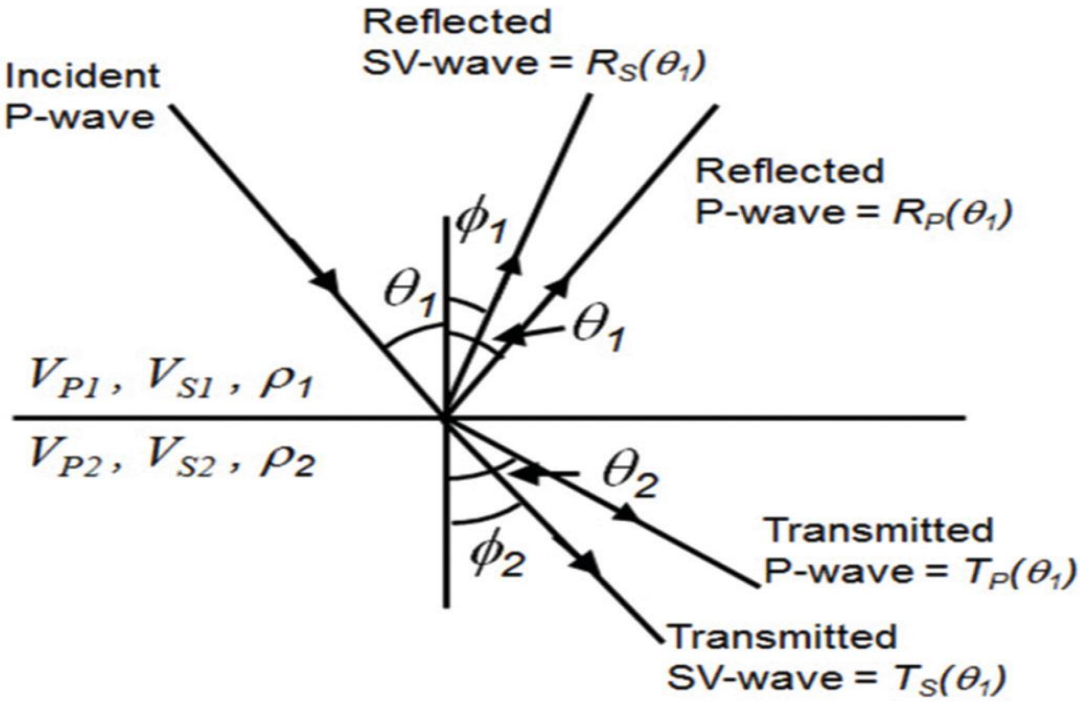

Fig. A.1. Mode conversion of an incident P-wave on the boundary between two elastic layers. (Figure courtesy: Dan Hampson et al, Hampson-Russell, A CGG Company, Calgary, Alberta, Canada available at http://csegrecorder.com/articles/view/joint-simultaneous-inversion-of-pp-and-ps-angle-gathers)

APPENDIX B

DUNKIN AND LEVIN'S STRETCH RATIO

Dunkin and Levin (1973) derived the stretch ratio to describe NMO-stretching of non-intersecting signals quantitatively. Let t_X and t_0 be the measured time in seismic data at an arbitrary source-receiver offset x, and the time at zero offset. In addition if we define Δt_X and Δt_0 as the corresponding reflection coefficient spacing at the offset x and zero offset, the link between Δt_X and Δt_0, the Dunkin and Levin's stretch ratio, A, can be given by following equation:

$$\Delta t_0 = \frac{\partial t_X}{\partial t_0} \Delta t_X = \mathrm{A} \Delta t_X,$$

where the NMO equation describes the relation between t_A and t_0 as following equation:

$$t_X{}^2 = t_0^2 + \frac{x^2}{V_{NMO}^2}$$

With the NMO equation and its expansion of Taylor series, Dunkin and Levin derived the stretch ratio A as a function of t_0, t_X, offset x and NMO velocity, V_{NMO}. It is given by following equation:

$$A = \frac{\partial t_X}{\partial t_0} = \frac{t_X}{t_0}\left(1 - \frac{x^2}{V_{NMO}^3 t_0} \cdot \frac{\partial V_{NMO}}{\partial t_0}\right)^{-1}$$

REFERENCES

Aki, K., and Richards, P. G., 1980, Quantitative Seismology – Theory and Methods: W. H. Freeman and Co., San Francisco, vol. 1.

Alam, A., and Taylor, J. D., 2006, Dip, azimuth and fault from continuous phase spectrum: SEG Technical Program Expanded Abstracts, **2006**, 998-1002.

Arnold, O., and Castagna, J. P., 2013, Layer thickness estimation from the frequency spectrum of seismic reflection data: SEG Technical Program Expanded Abstracts, **2013**, 1451-1455.

Backus, G. E., 1962, Long-wave elastic anisotropy produced by horizontal layering: Journal of Geophysical Research, **67**, no. 11, 4427-4440.

Batzle, M., and Wang, Z., 1992, Seismic properties of fluids: Geophysics, **57**, no. 11, 1396-1408

Bortfeld, R., 1961, Approximation to the reflection and transmission coefficients of plane longitudinal and transverse waves: Geophysical Prospecting, **9**, no. 4, 485-502.

Bracewell, R., 1986, The Fourier Transform and its Applications: McGraw-Hill Publishing Company.

Castoro, A., White, R., and Thomas, R., 2001, Thin-bed AVO: Compensating for the effects of NMO on reflectivity sequences: Geophysics, **66**, no. 6, 1714-1720.

Cohen, L., 1994, Time-Frequency Analysis: Prentice Hall.

Dunkin, J. W., and Levin, F. K., 1973, Effect of normal moveout on a seismic pulse: Geophysics, **38**, no. 4, 635-642.

Gardner, G. H. F., Gardner, L. W., and Gregory, A. R., 1974, Formation velocity and density – The diagnostic basics for stratigraphic traps: Geophysics, **39**, no. 6, 770-780.

Greenberg, M. L., and Castagna, J. P., 1992, Shear-wave velocity estimation in porous rocks: Theoretical formulation, preliminary verification and applications: Geophysical Prospecting, **40**, no. 2, 195-210.

Hilterman F. J., 2001, Seismic Amplitude Interpretation: Society of Exploration Geophysicists, 3-12, 13.

Kennett, B. L. N., 1979, Theoretical reflection seismograms for an elastic medium: Geophysical Prospecting, **27**, no. 2, 301-321.

Kennett, B. L. N., 1980, Seismic waves in a stratified half space: Geophysical Journal of the Royal Astronomical Society, **61,** no. 1, 1-10.

Matos, M. C., and Marfurt, K. J., 2008, Brazilian deep water carbonate reservoir study using the wavelet transform teager-kaiser energy: SEG Technical Program Expanded Abstracts, **2008**,

1516-1520.

Mukerji, T., Mavko, G., Mujica, D., and Lucet, N., 1995, Scale-dependent seismic velocity in heterogeneous media: Geophysics, **60**, no. 4, 1222-1233.

Partyka, G., Gridley, J., and Lopez, J., 1999, Interpretational applications of spectral decomposition in reservoir characterization: The Leading Edge, **18**, no. 3, 353-360.

Puryear, C., Castagna, J. P., Portniaguine, O., and Cobos, C., 2012, Costrained least-squares spectral analysis: application to seismic data: SEG Technical Program Expanded Abstracts, **2012**, 1-5.

Richards, P. G., and Frasier, C. W., 1976, Scattering of elastic waves from depth-dependent inhomogeneities: Geophysics, **41**, no. 3, 441-458.

Sacchi, M. D., 1997, Reweighting strategies in seismic deconvolution: Geophysical Journal International, **129**, 651-656.

Rutherford, S. R., and Williams, R. H., 1989, Amplitude-versus-offset in gas sands: Geophysics, **54**, no. 6, 680-688.

Sheriff, R. E., 2002, Encyclopedic Dictionary of Applied Geophysic, **4th edition**: Society of Exploration Geophysicists, 23.

Sheriff, R. E., and Geldart, L. P., 1995, Exploration Seismology, **2nd edition**: Cambridge University Press, 86.

Simmons, J. L., Jr. and Backus, M. M., 1994, AVO modeling and the locally converted shear wave: Geophysics, **59**, no. 8, 1237-1248.

Widess, M. B., 1973, How thin is a thin bed? : Geophysics, **38**, no. 6, 1176-1180.

Yilmaz, O., 2001, Seismic Data Analysis, **2nd edition**: Society of Exploration Geophysicists, vol. 1, 274-288.

Zhou, H., 2014, Practical Seismic Data Analysis: Cambridge University Press, 37-44.

Zoeppritz, K., 1919, On the reflection and propagation of seismic waves: Gottinger Nachrichten, **I**, 66-84.